

Enclosures

1. **Zhang J.**, Yue Q., Mazur M., Opanasenko M., Shamzhy M., Čejka J. Selective Recovery and Recycling of Germanium for the Design of Sustainable Zeolite Catalysts. *ACS Sustainable Chemistry & Engineering*, 2020, 8, 8235-8246.
2. **Zhang J.**, Veselý O., Tošner Z., Mazur M., Opanasenko M., Čejka J., Shamzhy M. Towards Controlling Disassembly Step within the ADOR Process for the Synthesis of Zeolites. *Chemistry of Materials*, 2021, 33, 1228-1237.
3. Podolean I., **Zhang J.**, Shamzhy M., Pârvulescu V. I., Čejka J. Solvent-Free Ketalization of Polyols over Germanosilicate Zeolites: The Role of the Nature and Strength of Acid Sites. *Catalysis Science & Technology*, 2020, 10, 8254-8264.
4. Shamzhy M., Přeč J., **Zhang J.**, Ruaux V., El-Siblani H., Mintova S. Quantification of Lewis Acid Sites in 3D and 2D TS-1 Zeolites: FTIR Spectroscopic Study. *Catalysis Today*, 2020, 345, 80-87.

Declaration of Authorship

I declare that I have presented this dissertation independently and I have properly cited all literatures. This work has not been submitted to obtain any other academic degree.

The dissertation was completed based on the following publications

1. **Zhang J.**, Yue Q., Mazur M., Opanasenko M., Shamzhy M., Čejka J. Selective Recovery and Recycling of Germanium for the Design of Sustainable Zeolite Catalysts. *ACS Sustainable Chemistry & Engineering*, 2020, 8, 8235-8246.
2. **Zhang J.**, Veselý O., Tošner Z., Mazur M., Opanasenko M., Čejka J., Shamzhy M. Towards Controlling Disassembly Step within the ADOR Process for the Synthesis of Zeolites. *Chemistry of Materials*, 2021, 33, 1228-1237.
3. Podolean I., **Zhang J.**, Shamzhy M., Pârvulescu V. I., Čejka J. Solvent-Free Ketalization of Polyols over Germanosilicate Zeolites: The Role of the Nature and Strength of Acid Sites. *Catalysis Science & Technology*, 2020, 10, 8254-8264.
4. Shamzhy M., Přeč J., **Zhang J.**, Ruaux V., El-Siblani H., Mintova S. Quantification of Lewis Acid Sites in 3D and 2D TS-1 Zeolites: FTIR Spectroscopic Study. *Catalysis Today*, 2020, 345, 80-87.

My contributions to these publications were as follows:

In the 1st paper, I optimized the synthesis conditions for Lewis acid zeolite catalysts. I performed XRD, UV-vis, ICP-OES, FTIR characterizations, and catalytic reaction testing (Bayer-Villiger oxidation, epoxidation). I participated in data analysis and manuscript writing. My overall contribution is 80%.

In the 2nd paper, I synthesized UTL zeolite and performed the kinetic study of UTL hydrolysis in Al-containing MeOH/H₂O medium. I performed XRD, ICP-OES, FTIR, and solid-state NMR characterizations. I participated in data analysis and manuscript writing. My overall contribution is 70%.

In the 3rd paper, I synthesized IWW and UTL zeolite catalysts and performed characterization of their structural and acidic characteristics using XRD, ICP-OES, FTIR spectroscopys. My overall contribution is 50%.

In the 4th paper, I participated in the development of FTIR spectroscopic method for the quantification of Lewis acidity of titanosilicate zeolite. My overall contribution is 30%.

Signature: Jin Zhang

Date: 31.05.2021

Supervisor:



Selective Recovery and Recycling of Germanium for the Design of Sustainable Zeolite Catalysts

Jin Zhang, Qiudi Yue, Michal Mazur, Maksym Opanasenko, Mariya V. Shamzhy,* and Jiří Čejka

Cite This: *ACS Sustainable Chem. Eng.* 2020, 8, 8235–8246

Read Online

ACCESS |



Metrics & More



Article Recommendations



Supporting Information

ABSTRACT: Germanosilicate zeolites with extra-large-/multidimensional pore systems have a high potential for catalytic applications. However, their insufficient hydrothermal stability, high cost, and lack of strong acid sites limit their use. This work presents a synthetic approach involving post-synthesis degermanation/germanium recycling and remetallation steps for the cost-efficient preparation of Brønsted and Lewis acid zeolite catalysts. Optimization of degermanation conditions (i.e., pH and duration of the leaching treatment) allowed to recover up to 78–94% germanium from ITH, IWW, and UTL zeolites. Further metalation of hydrolyzed IWW zeolites resulted in a set of Al-, Ti-, and Sn-substituted catalysts showing enhanced activity in model acid-catalyzed reactions, such as 1-hexanol tetrahydropyranlation, 1-octene epoxidation, and Baeyer–Villiger oxidation of cyclohexanone. Noticeably, the phase selectivity of zeolite formation upon germanium recycling strongly depended on the method for parent zeolite separation from the leaching solution. In contrast to microfiltration, which produces a versatile source of germanium for the preparation of various zeolites, filtration leads to the formation of germanosilicates with the topology of the parent zeolite regardless of recycling conditions. Such a “memory effect” was rationalized based on the characterization of the germanium source and crystallization products using a combination of techniques (e.g., X-ray diffraction, Fourier transform infrared spectroscopy, scanning electron microscopy, and transmission electron microscopy).

KEYWORDS: Ge recycling, germanosilicate zeolites, sustainable catalysis



INTRODUCTION

In the last 2 decades, germanosilicate zeolites have been the focus of considerable research, not only fundamental but also applied. Most extra-large-pore zeolites are highly interesting for the oil industry, and specialty chemicals have been prepared as germanosilicates.^{1–4} Moreover, germanosilicate zeolites characterized by the unidirectional location of Ge-enriched D4R units were discovered as precursors for novel isorecticular zeolites⁵ via the assembly–disassembly–organization–reassembly (ADOR) synthesis protocol.^{6,7} ADOR applied to only one starting material, UTL, has led so far to six new zeolites: IPC-2 (OKO), IPC-4 (PCR),⁸ IPC-6 (*PCS), IPC-7,⁷ IPC-9, and IPC-10.⁹ Importantly, the ADOR approach has recently been expanded to other germanosilicates,^{10–14} enriching the family of ADORable zeolites with new members. Yet, despite their high potential for catalytic applications, the high cost of Ge limits the practical use of both germanosilicate and ADORable zeolites. Nevertheless, recent studies have shown that the low hydrolytic stability of Si–O–Ge and Ge–O–Ge bonds can be used to incorporate different tri- and tetravalent elements into the frameworks of germanosilicate zeolites to tailor their catalytic properties.¹⁵ In particular, the post-synthesis stabilization by isomorphous substitution of Ge with Al,^{16–19} Ga,²⁰ Ti,²¹ and Zr²² has been reported as an efficient approach for the preparation of hydrolytically stable catalysts and only broadens the use of new germanosilicate

zeolites in catalysis without reducing production costs because Ge is substituted without any recycling treatment.¹⁵

Thus, a sequential two-step post-synthesis modification, intending to overcome the aforementioned limitations, is proposed here for germanosilicate zeolites (Scheme 1). The method includes the following steps: (1) Ge leaching and recycling and (2) heteroelement incorporation, generating catalytically active sites in degermanated zeolites.

Efficient recycling of Ge recovered from the IWW zeolite in the synthesis of different germanosilicates was confirmed by X-ray diffraction (XRD), N₂ adsorption/desorption, chemical analysis, and scanning electron microscopy (SEM). In turn, the enhanced catalytic activity of Al-, Ti-, and Sn-substituted IWW zeolites produced via a degermanation–remetallation approach was verified in model reactions of 1-hexanol tetrahydropyranlation (THP), epoxidation of 1-octene, and Baeyer–Villiger oxidation (BVO) of cyclohexanone.

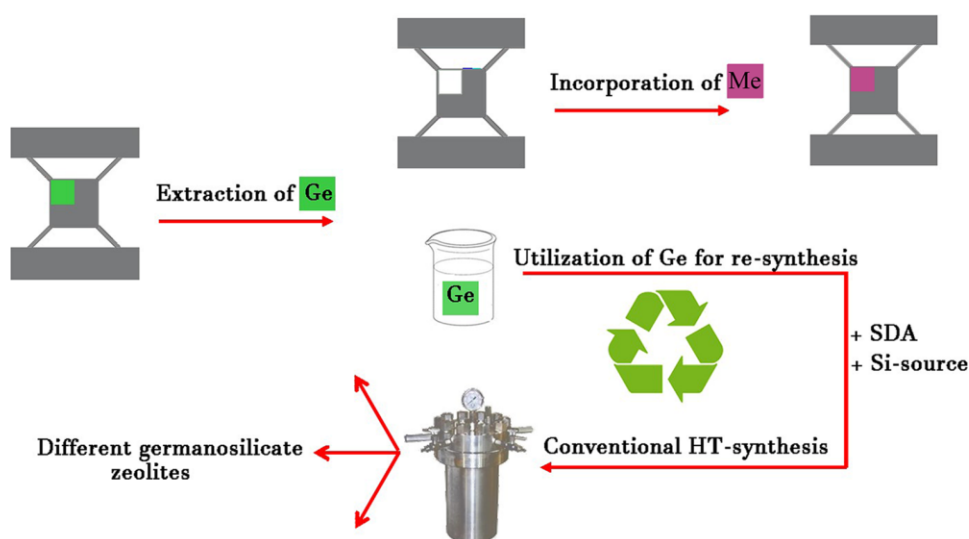
Received: February 19, 2020

Revised: April 21, 2020

Published: May 8, 2020



Scheme 1. Two-Step Post-Synthesis Approach for the Cost-Efficient Production of Catalytically Active Materials Based on Germanosilicate Zeolites



METHODS

Zeolite Synthesis. Structure-Directing Agents. Hexamethonium (HM) dihydroxide, 1,5-bis(methylpyrrolidinium) pentane dihydroxide (MPP(OH)₂, SDA_{IWW}), and (6R,10S)-6,10-dimethyl-5-azoniaspiro decane hydroxide (SDA_{UTL}) were prepared according to refs 23,24,25. The structures of structure-directing agents (SDAs) were verified by ¹H NMR using dimethyl-sulfoxide-*d*₆ as a solvent.

Hydrothermal Synthesis. ITH zeolites with small and large crystals were prepared using *N,N,N',N'*-tetramethyl-1,6-hexanediamine (TMHDA, SDA_{ITH}) or HM dihydroxide as SDAs according to refs 26 and 27, respectively. The composition of the reaction mixture for ITH zeolites with small crystals was 0.90 SiO₂:0.09 GeO₂:0.25 HM:5 H₂O. The resulting gel was charged into a 25 mL Teflon-lined autoclave heated at 175 °C for 14 days under agitation (60 rpm).

To synthesize ITH zeolites with larger crystals, a gel composition of 0.67 SiO₂:0.33 GeO₂:7 TMHDA:1.4 HF:44 H₂O was used. Then, the reaction mixture was heated at 175 °C for 3 days under static conditions.²⁶

Germanosilicate and Al- and Sn-substituted IWW zeolites were synthesized using MPP dihydroxide as the SDA according to Corma et al.^{28,29} The gel with a composition of 0.66 SiO₂:0.33 GeO₂:*x* AlO_{1.5}:(*y* SnO₂):0.25 MPP(OH)₂:*z* H₂O (*x* = 0, *y* = 0, *z* = 15 for the germanosilicate zeolite; *x* = 0.02, *y* = 0, *z* = 15 for the Al-substituted zeolite; *x* = 0, *y* = 0.01, *z* = 3.5 for the Sn-substituted zeolite) was transferred into a Teflon-lined autoclave and heated at 175 °C for 7 (IWW-5 zeolite), 14 (Al-IWW_{hydro} zeolites), or 23 (Sn-IWW_{hydro}) days under static conditions, respectively. Aluminum nitrate nonahydrate (98%, Aldrich) and tin(IV) chloride pentahydrate (98%, Aldrich) were used as the Al and Sn sources, respectively.

The UTL zeolite was synthesized according to ref 30. A gel with a composition of 0.67 SiO₂:0.33 GeO₂:0.25DMAD:30 H₂O was heated at 175 °C for 7 days under agitation (60 rpm).

The solid products were recovered by filtration, washed with deionized water, and dried overnight at 70 °C. Then, the zeolites were calcined in the air flow according to refs.^{17,26,28}

All germanosilicate zeolites under investigation were designated as ITH-*n*, IWW-*n*, and UTL-*n*, in which *n* represents the Si/Ge ratio in the zeolites. Directly synthesized Al-, Sn-containing IWW zeolites were designated as Me-IWW_{hydro}.

Ge Leaching (Hydrolysis of Zeolites). Calcined germanosilicate zeolites (0.1 g) were hydrolyzed in 5 mL of hydrochloric or nitric acid. Various concentrations of acids were used (0, 0.1, 1, and 4 M) at *T* = 25 or 80 °C. The duration of the treatment was fixed at 1 or 16 h. The degermanated samples were filtrated using a Fisher Scientific

qualitative filter paper (grade 601) or an MF-Millipore Membrane Filter (0.025 μm pore size), washed sequentially with 5 mL of the corresponding acid solution and with 10 mL of deionized water, and dried at room temperature. The hydrolyzed zeolites were further characterized and used for post-synthesis incorporation of Al, Ti, and Sn, while the leaching solution (5 mL solution from initial treatment + 5 mL solution from the first washing) was analyzed by inductively coupled plasma–optical emission spectroscopy (ICP–OES) to determine the degree of leached Ge. The hydrolyzed zeolites were named “zeolite-*x*-H₂O-*T*°C-*rh*/*n*” or “zeolite-*x*-*y*M HCl (HNO₃)-*T*°C-*rh*”, in which *x* corresponds to the Si/Ge ratio in the initial zeolite, *y*—to the concentration of the respective acid, *T*—to the temperature of the treatment, and *τ*—to the duration of the treatment and *n* represents the multiplicity of the treatment, respectively.

Ge Recovery/Recycling. The initial germanosilicate zeolite IWW-5 (10 g) was treated three times with 1000 mL of water. The leaching solution was obtained after the recovery of the degermanated zeolite by filtration. Further evaporation of the excess of water at *T* = 65 °C, *p* = 30 atm for 2 h resulted in a solid product, showing the XRD pattern characteristic of GeO₂.

GeO₂ recovered either after filtration (GeO₂^{filt}) or microfiltration (GeO₂^{microfilt}) was further used as the Ge source for the synthesis of IWW_{recycle}, ITH_{recycle}, and UTL_{recycle} zeolites according to the protocols described *vide supra*. The samples synthesized using recovered GeO₂ were designated as zeolite_{recycle}-GeO₂-SDA_n, in which the “zeolite” corresponds to the topology of the formed zeolite according to XRD, *x*—to the procedure of GeO₂ recovery, that is, filtration or microfiltration, and *n*—to the type of used SDA and synthesis conditions, that is, *n* = IWW, UTL, and ITH were assigned to the synthesis conditions typical for the preparation of IWW, UTL, and ITH zeolites, respectively.

Post-Synthesis Preparation of Metal-Substituted IWW Zeolites. Aluminum nitrate nonahydrate (98%, Aldrich), titanium chloride(IV) (1 M solution in toluene, Acros Organics), and tin chloride(IV) (1 M solution in heptane, Aldrich) were used as the Al, Ti, and Sn sources, respectively.

To prepare an Al-substituted zeolite, IWW-5-H₂O-25°C-16h/3 was treated with a 1 M aqueous solution of Al(NO₃)₃ (pH = 2) with a solid/liquid ratio of 10 g/L at 95 °C for 96 h. Solid samples recovered by centrifugation were washed five times with deionized water (solid/liquid ratio 10 g/L) to remove the unreacted metal precursor, followed by calcination at 450 °C for 4 h with a temperature ramp of 1 °C·min⁻¹. The sample was designated as IWW/Al_{post}.

To prepare Ti- and Sn-substituted zeolites, IWW-5-H₂O-25°C-16h/3 was treated with a 0.05–0.45 M solution of TiCl₄ in toluene or SnCl₄ in heptane (solid/liquid ratio 20 g/L) at 95 °C for 96 h in the atmosphere of N₂. Before the treatment, the samples were activated at 450 °C for 1 h at a rate of 10 °C min⁻¹ and cooled in a desiccator to room temperature. Solid samples recovered by centrifugation were washed five times with the solvent (toluene or heptane) and five times with methanol to remove the unreacted metal, followed by calcination at 450 °C for 3 h with a temperature ramp of 1 °C min⁻¹. The samples were designated as IWW/Ti_{post}/xM and IWW/Sn_{post}/xM, wherein *x* refers to the molarity of TiCl₄ or SnCl₄ solution used in the metalation step.

Characterization. Sample phase purity was examined by powder XRD using a Bruker AXS D8 Advance diffractometer with a Vantec-1 detector in the Bragg–Brentano geometry using Cu K α radiation (1.54056 Å). Samples were ground gently and packed into the holder carefully before the measurement.

The average crystallite size of recovered GeO₂ was estimated using the Scherrer equation³¹

$$D = \frac{k\lambda}{\beta_{hkl} \cos \theta_{hkl}} \quad (1)$$

where *k* is the shape factor (0.94 for spherical nanoparticles); λ is the X-ray wavelength; β_{hkl} is the full width at half-maximum of the diffraction peak in radian; and θ_{hkl} is the Bragg angle.

Transmission electron microscopy (TEM) imaging was performed using JEOL NeoARM 200F operated at 200 kV. The alignment was performed using the standard gold nanoparticle film method.

The morphology of the zeolite crystals was studied by SEM (TESCAN Vega microscope).

Si, Ge, Al, Ti, and Sn contents were determined by elemental analysis using ICP–OES (Thermo Scientific iCAP 7000), digesting 50 mg of the zeolite in a mixture of HF, HNO₃, and HCl. The samples were placed in the microwave in a closed vessel at *T* = 140 °C for 35 min. A saturated solution of H₃BO₃ was then added for the complexation of the excess of HF. After digestion, solutions under analysis were collected in 250 mL flasks, and the volume was measured with ultrapure water.

N₂ adsorption/desorption isotherms were collected at –196 °C using a 3Flex (Micromeritics) static volumetric apparatus. Before the sorption measurements, all samples were degassed with a turbo molecular pump at *p* < 10⁻² Pa and *T* = 300 °C for 8 h. The surface areas were evaluated by the standard Brunauer–Emmett–Teller (BET) method using adsorption data in the *p/p*⁰ range of 0.05–0.20, while the *t*-plot method was employed to obtain the micropore volumes.³²

The concentration of Lewis (cL) and Brønsted (cB) acid sites was determined after pyridine (Py) adsorption, followed by Fourier transform infrared spectroscopy (Py-FTIR) on a Nicolet iS50 spectrometer with a transmission MCT/B detector similar to refs^{33–35} (experimental details are given in the Supporting Information, S8).

Diffuse reflectance ultraviolet–visible (UV–vis) spectra were collected on a Cary 300 UV–vis spectrophotometer using BaSO₄ as a reference. The spectra were collected in the wavelength range of 200–500 nm and converted into absorption spectra using the Kubelka–Munk function.

Testing the Catalytic Activity. The catalytic performances of Al-, Ti-, and Sn-substituted IWW zeolites were studied in the reaction of 1-hexanol THP, 1-octene epoxidation, and BVO of cyclohexanone, respectively (experimental details are given in the Supporting Information, S10). All catalytic tests were performed on a multi-experiment workstation StarFish (Radleys Discovery Technologies) under atmospheric pressure. Before the catalytic testing, the catalyst was activated at 450 °C for 2 h at a rate of 10 °C min⁻¹. Samples of the reaction mixture were periodically collected and analyzed by gas chromatography (Agilent 7890B). The reaction products were identified using a Thermo Scientific ISQ LT—TRACE 1310 GC/MS.

The activities of the catalysts were compared based on turnover frequency (TOF) numbers,³⁶ determined from the initial segment of conversion versus time plot (*t* = 10 min) as

$$\text{TOF} = \text{moles}_{(\text{reactant converted})} / \text{moles}_{(\text{active sites})}^{-1} \text{ hour}^{-1} \quad (2)$$

RESULTS AND DISCUSSION

Synthesis of Germanosilicate Zeolites. Three germanosilicate zeolites differing in channel sizes were chosen for the study of Ge leaching: medium-pore ITH with a 9 × 10 × 10 ring channel system, large-pore IWW with a multidimensional 8 × 10 × 12 ring pore system, and extra-large pore UTL with 12 × 14 ring pores. The chemical composition of the zeolites prepared from different reaction mixtures ranged from Si/Ge = 3.8–6.7 for UTL through⁶ Si/Ge = 2.3–13.3 for ITH¹⁰ to Si/Ge = 2.9–7.2 for IWW.¹⁷ To assess the effect of zeolite topology on Ge leaching, UTL-3, ITH-3, and IWW-5 zeolites with similar Si/Ge ratios (Table 1) were prepared in this work.

Table 1. Chemical Compositions and Crystal Sizes of Parent Germanosilicates

Sample	chemical composition, mol %			crystal size, μm
	Si	Ge	Si/Ge	
ITH-10	90.9	9.1	10.0	2 × 0.5 × 0.5
ITH-3	75.6	24.4	3.1	40 × 10 × 5
IWW-5	84.1	15.9	5.3	0.5 × 5 × 5/0.5 × 0.5 × 0.5
UTL-3	76.2	23.8	3.2	50 × 30 × <0.5

Simultaneously, ITH-3 and ITH-10 zeolites with crystals of different sizes were synthesized via TMHDA- and HM-assisted crystallization.^{26,27} The XRD patterns of all as-synthesized samples (Figure S1) match those reported earlier,^{3,28,37,38} thus showing their phase purity. SEM images indicated that both ITH-3 and ITH-10 zeolites were formed by elongated crystals of 40 × 10 × 5 and 2 × 0.5 × 0.5 μm (Figure 1a,b), respectively. The IWW-5 sample shows the agglomeration of 0.5 × 5 × 5 μm sized and a number of smaller 0.5 × 0.5 × 0.5 μm sized rectangular crystals (Figure 1c), while the UTL-3 zeolite formed quite uniform thin rectangular 50 × 30 × <0.5 μm sized crystals (Figure 1d).

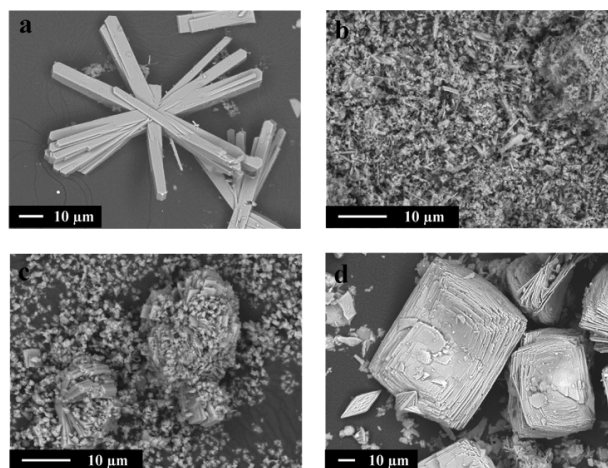


Figure 1. SEM images of germanosilicate zeolites: (a) ITH-3, (b) ITH-10, (c) IWW-5, and (d) UTL-3.

While ITH-3 showed a type-I isotherm characteristic of microporous materials, all ITH-10, IWW-5, and UTL-3 exhibited micro-mesoporosity, as demonstrated by their combined type-I and type-IV isotherms with H3-/H4-type hysteresis loops (Figure S2).³² In the case of UTL-3 and especially ITH-10 with smaller crystals, the desorption branch of the H4-type hysteresis loop shows a step-down at $p/p^0 \approx 0.4$, which is associated with the cavitation effect during adsorbate evaporation from larger mesopores (i.e., interparticle voids which are filled at $p/p^0 > 0.95$) limited by smaller mesopores (≤ 5 nm). A lack of such step in the isotherm of IWW-5 evidences that there is no cavitation phenomenon in the interparticle mesopores. The micropore volumes decreased in the following order: UTL ($0.19 \text{ cm}^3 \cdot \text{g}^{-1}$) > IWW ($0.17 \text{ cm}^3 \cdot \text{g}^{-1}$) > ITH ($0.12\text{--}0.13 \text{ cm}^3 \cdot \text{g}^{-1}$).

Ge Leaching (Hydrolysis of Zeolites). To assess the effect of treatment conditions on the degree of Ge leaching, nature (HCl or HNO_3), and concentration (0.1, 1, or 4 M) of the acid, temperature (25 or 80 °C) and duration (1 or 16 h) of the treatment were systematically varied. The fraction of Ge recovered after the treatment of ITH-3 with 0.1 M HCl at 25 °C for 16 h was higher than that obtained after treatment with HNO_3 under the same conditions (i.e., 45 vs 40%, Figure 2).

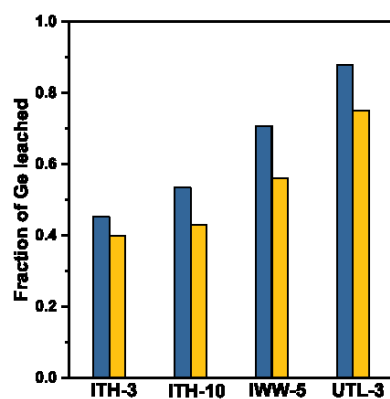


Figure 2. Fraction of Ge leached from the initial zeolites after treatment with 0.1 M HCl (blue) vs HNO_3 (yellow) for 16 h at 25 °C.

ITH-10 (53 vs 43%), IWW-5 (71 vs 56%), and UTL-3 (88 vs 75%) showed similar results, which may reflect differences in the complexation ability of Cl^- and NO_3^- toward Ge.³⁹

Temperature had no significant effect on the efficiency of degermanation (Figure 3a) as the fraction of Ge leached was nearly the same for all samples treated at 25 or 80 °C (difference did not exceed 2%). Prolonging the treatment allowed to extract a higher amount of Ge (25 vs 45%) from medium-pore ITH-3 with large crystals, without affecting the degree of leaching of ITH-10 with smaller crystals, large-pore IWW, and extra-large pore UTL zeolites (Figure 3a). This indicates diffusion control during the hydrolysis of germanosilicate zeolites with small-size pores and large-size crystals. Noticeably, the degree of leached Ge increases with the decrease in HCl concentration from 4 to 0.1 M (Figure 3b, Table S1). At the first sight, this apparently anomalous result can be accounted for the condensation reaction between germanol groups of the leached $\text{Ge}(\text{OH})_x\text{O}_{(2-0.5x)}$ species and framework silanol defects (i.e., reincorporation of Ge into the zeolite framework) accelerating with increasing $[\text{H}^+]$. However, further decreasing the HCl concentration (e.g., the treatment of zeolites in water) did not enhance the efficiency of Ge leaching (Figure 4a), which may originate from slowing

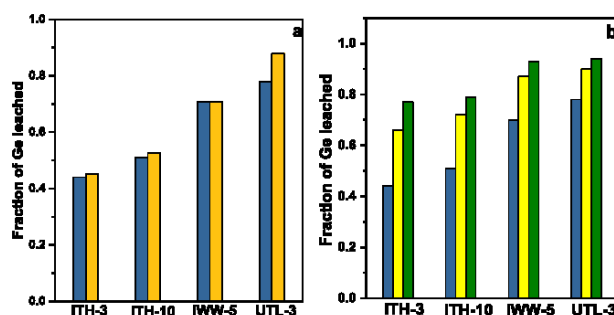


Figure 4. Fraction of Ge leached from the initial zeolites after (a) treatment with H_2O (blue) vs 0.1 M HCl (yellow) or (b) repetitive treatment with H_2O : 1 time (blue), 2 times (yellow), and 3 times (green) at 25 °C for 16 h.

the cleavage of $\text{Ge-O}(\text{Si})$ bonds with a drop in $[\text{H}^+]$. In total, the Ge leaching degree is, likely, determined by the relative rates of these two H^+ -catalyzed processes, while optimum pH for Ge extraction is 2.

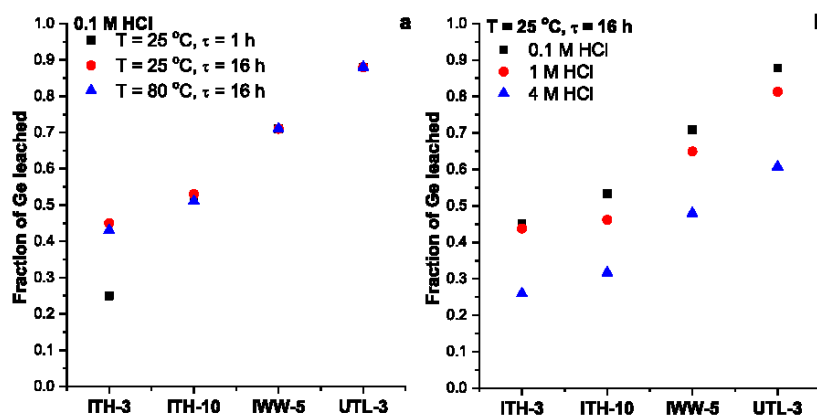
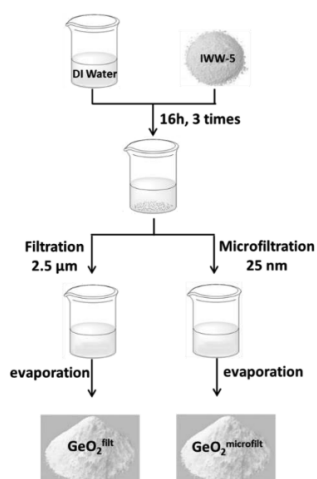


Figure 3. Fraction of Ge leached from the initial zeolites after treatment with (a) 0.1 M HCl under different conditions or (b) HCl of variable concentrations at 25 °C for 16 h.

Importantly, repetitive treatment in water allowed to increase the amount of recovered Ge substantially (Figure 4b). Finally, up to 78–94% of Ge were recovered from germanosilicate zeolites after triple treatment with water depending on the type and textural properties of the initial zeolite.

Ge Reuse. Leaching solution separation from the degermanated zeolite via filtration or microfiltration followed by water evaporation was used to collect $\text{GeO}_2^{\text{filt}}$ and $\text{GeO}_2^{\text{microfilt}}$ samples, respectively (Scheme 2).

Scheme 2. Recovery of GeO_2 via IWW Zeolite Hydrolysis



The XRD patterns of both $\text{GeO}_2^{\text{filt}}$ and $\text{GeO}_2^{\text{microfilt}}$ (the samples recovered from the IWW-5 zeolite are shown as representative) feature solely diffraction lines characteristic of germanium(IV) oxide (Figure 5a). Simultaneously, the FTIR spectra of $\text{GeO}_2^{\text{filt}}$ and $\text{GeO}_2^{\text{microfilt}}$ display the bands (~ 1100 – 1000 cm^{-1}) corresponding to Si–O vibrations (Figure 5b). The obtained results reveal the presence of SiO_2 -containing entities in both $\text{GeO}_2^{\text{filt}}$ and $\text{GeO}_2^{\text{microfilt}}$ samples, although chemical analysis showed that the fraction of SiO_2 does not exceed 3 wt %. The average crystallite sizes of GeO_2 estimated based on the broadening (011) peak using the Scherrer equation were 77 nm (for commercial GeO_2 and $\text{GeO}_2^{\text{filt}}$) and 35 nm (for $\text{GeO}_2^{\text{microfilt}}$). Consistently, high-resolution TEM (HRTEM) provided another evidence on higher dispersion of

$\text{GeO}_2^{\text{microfilt}}$ particles in comparison to that of $\text{GeO}_2^{\text{filt}}$ (Figure S3). Residual zeolite species clearly visible in the HRTEM image of the $\text{GeO}_2^{\text{filt}}$ sample evidently facilitated the aggregation of germanium oxide(IV) particles formed upon water evaporation.

To exemplify the reuse of leached GeO_2 as the Ge source for the synthesis of zeolites, the GeO_2 extracted from the IWW-5 sample was repeatedly used for crystallization under conditions (i.e., particular SDA, gel composition, crystallization time, and temperature) typical for the formation of IWW, ITH, and UTL phases. Noticeably, the use of $\text{GeO}_2^{\text{filt}}$ resulted in the crystallization of pure IWW zeolites independently of the synthesis conditions (Figure 6a).

$\text{IWW}_{\text{recycle}}-\text{GeO}_2^{\text{filt}}-\text{SDA}_{\text{UTL}}$ and $\text{IWW}_{\text{recycle}}-\text{GeO}_2^{\text{filt}}-\text{SDA}_{\text{ITH}}$ samples were depleted in the amount of incorporated Ge ($\text{Si}/\text{Ge} = 20$ – 21) and showed low textural characteristics ($V_{\text{micro}} = 0.07$ – $0.09 \text{ cm}^3/\text{g}$, Table 2) and nonuniform crystals typical for the IWW zeolite (Figure 7). In turn, using $\text{GeO}_2^{\text{microfilt}}$ to prepare the parent IWW zeolite enabled the formation of big and uniform crystals of $\text{IWW}_{\text{recycle}}-\text{GeO}_2^{\text{microfilt}}-\text{SDA}_{\text{IWW}}$ with a chemical composition ($\text{Si}/\text{Ge} = 4$ – 5) and a micropore volume ($V_{\text{micro}} = 0.17$ – $0.18 \text{ cm}^3/\text{g}$, Table 2) similar to those of the parent IWW-5. In contrast to IWW-5 possessing smaller crystals (Table 2), the adsorption isotherm of $\text{IWW}_{\text{recycle}}-\text{GeO}_2^{\text{microfilt}}-\text{SDA}_{\text{IWW}}$ shows no sign of filling interparticle pores at $0.5 < p/p^0$ (Figure 6b).

In contrast to $\text{GeO}_2^{\text{filt}}$, which promoted the selective crystallization of the IWW phase, the use of $\text{GeO}_2^{\text{microfilt}}$ resulted in the formation of $\text{IWW}_{\text{recycle}}$, $\text{UTL}_{\text{recycle}}$, and $\text{ITH}_{\text{recycle}}$ depending on the synthetic conditions (Table 2). $\text{Zeolite}_{\text{recycle}}-\text{GeO}_2^{\text{microfilt}}-\text{SDA}-n$ showed XRD patterns (Figure 8a), N_2 adsorption/desorption isotherms (Figure 8b), and crystal morphology (Figure 9) similar to those characteristic of IWW-5 ($n = \text{IWW}$), UTL-3 ($n = \text{UTL}$), and ITH-3 ($n = \text{ITH}$) germanosilicates synthesized under similar conditions, albeit using commercial GeO_2 as a source of Ge. The crystal sizes of recycled zeolites were smaller than those of original samples (Table 2). Thus, different N_2 uptakes at $p/p^0 > 0.95$ characteristic of filling intercrystalline voids were observed in the isotherms of original and recycled materials (Figures S2 and 8b). Noticeably, in contrast to the IWW-5 sample (Figure S2), a step-down at $p/p^0 \approx 0.4$ is clearly seen in the desorption branch of $\text{IWW}_{\text{recycle}}-\text{GeO}_2^{\text{microfilt}}-\text{SDA}_{\text{IWW}}$ (Figure 8b), evidencing a cavitation effect in the interparticle mesopores of $\text{IWW}_{\text{recycle}}$.

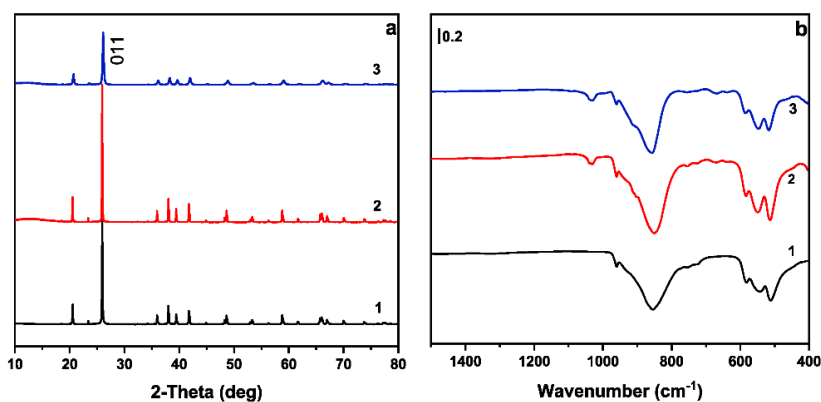


Figure 5. (a) XRD patterns and (b) FTIR spectra of commercial GeO_2 (1), $\text{GeO}_2^{\text{filt}}$ (2), and $\text{GeO}_2^{\text{microfilt}}$ (3).

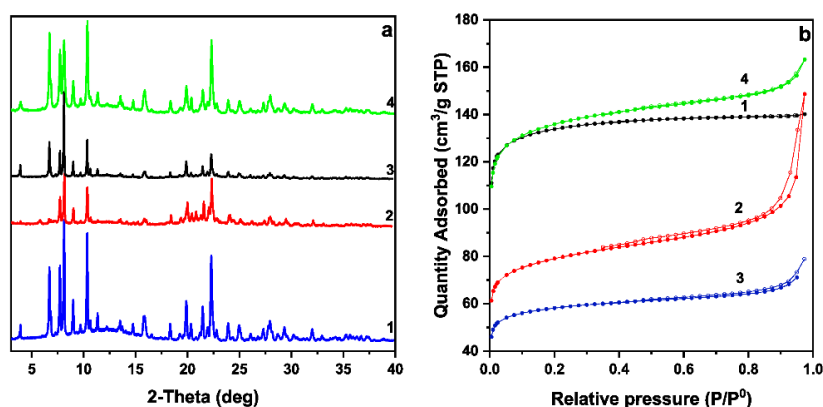


Figure 6. (a) XRD patterns and (b) N_2 adsorption (filled symbols) and desorption (empty symbols) isotherms of $IWW_{\text{recycle}}-GeO_2^{\text{fllt}}-SDA_{IWW}$ (1), $IWW_{\text{recycle}}-GeO_2^{\text{fllt}}-SDA_{UTL}$ (2), $IWW_{\text{recycle}}-GeO_2^{\text{fllt}}-SDA_{ITH}$ (3), and $IWW-5$ (4).

Table 2. Textural Properties and Chemical Compositions of Parent $IWW-5$ and Zeolite $_{\text{recycle}}-GeO_2-SDA_n$ Zeolites

sample	phase composition	textural properties			Si/Ge
		V_{micro} cm^3/g	S_{BET} m^2/g	crystal size, μm	
$IWW-5$	IWW	0.17	474	$0.5 \times 5 \times 5/0.5 \times 0.5 \times 0.5$	5.3
zeolite $_{\text{recycle}}-GeO_2^{\text{fllt}}-SDA_{IWW}$		0.18	454	$10 \times 3 \times 1.5$	4.2
zeolite $_{\text{recycle}}-GeO_2^{\text{fllt}}-SDA_{UTL}$		0.09	276	n.d.	21.7
zeolite $_{\text{recycle}}-GeO_2^{\text{fllt}}-SDA_{ITH}$		0.07	203	n.d.	20.6
zeolite $_{\text{recycle}}-GeO_2^{\text{microfllt}}-SDA_{IWW}$		0.17	451	$<0.5 \times <0.5 \times <0.5$	4.7
$UTL-3$	UTL	0.19	450	$50 \times 30 \times <0.5$	3.2
zeolite $_{\text{recycle}}-GeO_2^{\text{microfllt}}-SDA_{UTL}$		0.18	427	$40 \times 30 \times <0.5$	4.1
$ITH-3$	ITH	0.12	271	$40 \times 10 \times 5$	3.1
zeolite $_{\text{recycle}}-GeO_2^{\text{microfllt}}-SDA_{ITH}$		0.13	319	$40 \times 6 \times 5$	3.5

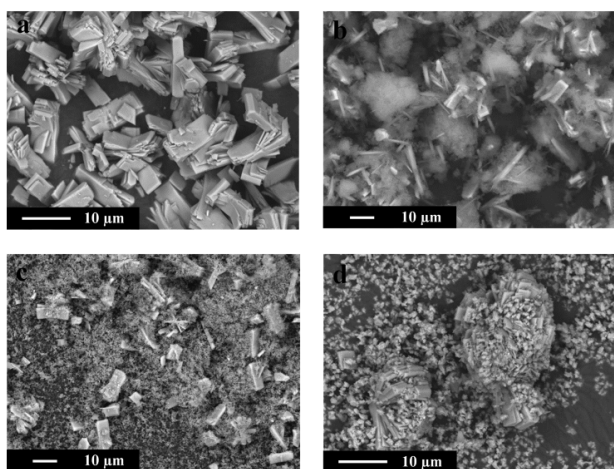


Figure 7. SEM images of (a) $IWW_{\text{recycle}}-GeO_2^{\text{fllt}}-SDA_{IWW}$, (b) $IWW_{\text{recycle}}-GeO_2^{\text{fllt}}-SDA_{UTL}$, (c) $IWW_{\text{recycle}}-GeO_2^{\text{fllt}}-SDA_{ITH}$, and (d) $IWW-5$.

Phase selectivity of crystallization using GeO_2^{fllt} or $GeO_2^{\text{microfllt}}$ can be rationalized considering previously proposed mechanisms of zeolite formation¹⁵ (Scheme 3). The following steps of SDA-assisted crystallization of zeolites are generally accepted: (1) induction period—depolymerization of the sources of Ge- and Si-producing oligomeric Si_kGe_l anions; (2) nucleation—the formation of organic–inorganic nuclei, composed of the SDA^+ cations and $Si_xGe_yO_z^{w-}$ polyanions (Si_xGe_y in Scheme 3), followed by (3) aggregation of $[SDA](Si_xGe_y)$ species into assemblies—crystal growth.

Typically, the resulting zeolite framework consists of building units with a structure similar to that of the stable oligomeric ions that form $[SDA](Si_xGe_y)$ nuclei.⁴⁰ Based on the FTIR (Figure Sb) and TEM (Figures S3 and 4) results, the presence of sub-nano fragments of the IWW zeolite (Si_kGe_l) cannot be excluded in $GeO_2^{\text{microfllt}}$, while GeO_2^{fllt} evidently contains both IWW nanoparticles (zeolite seeds, Scheme 3) and Si_kGe_l , playing a role in the crystallization process. Particularly for mixed seed-SDA-containing systems formed when using GeO_2^{fllt} , the phase composition of crystallization products is most likely determined by the relative stability of the different nuclei, that is, (i) $[SDA](Si_xGe_y)$ leading to the formation of either ITH , UTL , or IWW depending on the SDA, (ii) $[SDA][Si_kGe_l]$ leading to the formation of the IWW phase, and (iii) IWW seeds. The selectivity of zeolite crystallization was independent of the SDA, thus showing that the $[SDA](Si_xGe_y)$ nuclei were less stable than IWW seeds. The formation of large and uniform crystals of $IWW_{\text{recycle}}-GeO_2^{\text{fllt}}-SDA_{IWW}$ (Figure 7a, Scheme 3) supports a cooperative seed-SDA-assisted crystallization without an induction period and characterized by rapid crystal growth. Conversely, despite not affecting zeolite phase selectivity, $[SDA_{UTL}](Si_xGe_y)$ and $[SDA_{ITH}](Si_xGe_y)$ apparently restrict the growth of IWW crystals (Scheme 3, Figure 7b,c).

However, the presence of Si_kGe_l sub-nano IWW fragments apparently has no effect on the selectivity of zeolite formation when using SDA_{UTL}/SDA_{ITH} and $GeO_2^{\text{microfllt}}$. This may be explained by the instability of the relatively small IWW entities, which are susceptible to depolymerization—degradation during the induction period/nucleation. The resulting smaller Si–Ge–O species can be further utilized to form/grow the most

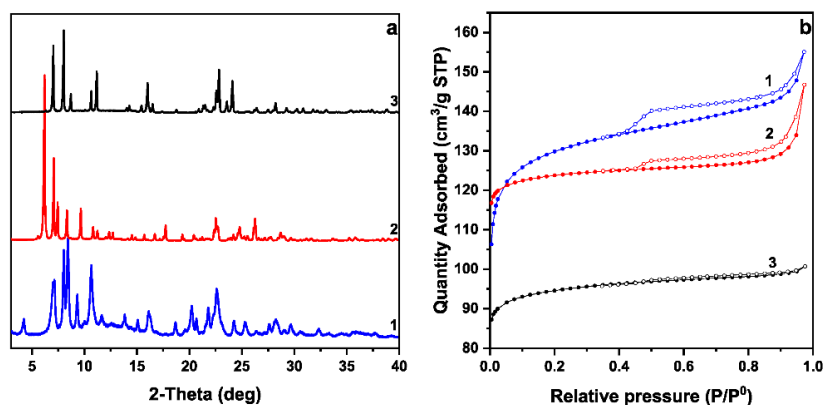


Figure 8. (a) XRD patterns and (b) N₂ adsorption (filled symbols) and desorption (empty symbols) isotherms of zeolite_{recycle}-GeO₂^{microfilt}-SDA_{IWW} (1), zeolite_{recycle}-GeO₂^{microfilt}-SDA_{UTL} (2), and zeolite_{recycle}-GeO₂^{microfilt}-SDA_{ITH} (3).

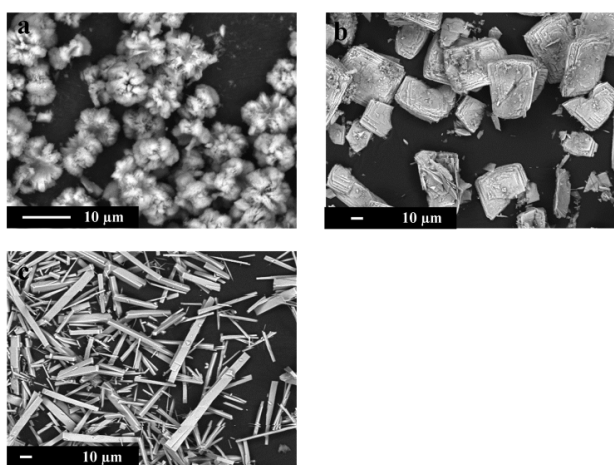


Figure 9. SEM images of (a) zeolite_{recycle}-GeO₂^{microfilt}-SDA_{IWW}, (b) zeolite_{recycle}-GeO₂^{microfilt}-SDA_{UTL}, and (c) zeolite_{recycle}-GeO₂^{microfilt}-SDA_{ITH}.

stable [SDA](Si_xGe_y) entities, forming pure ITH and UTL phases when using SDA_{ITH} and SDA_{UTL}, respectively (Scheme 3).

Post-Synthesis Incorporation of Al, Ti, and Sn: Textural and Acidic Properties. In agreement with refs 10 and 11 and 41, the XRD patterns of zeolites degermanated either in acidic or in neutral medium (Figure S5) indicated that the structure ordering of medium-pore ITH and large-pore IWW zeolites is maintained, while the structural transformation of the UTL framework prevented its post-synthesis functionalization. Here, the IWW-5-H₂O-25°C-16h/3 sample was used to incorporate Al, Ti, and Sn atoms into the zeolite framework to demonstrate the success of the full cycle [synthesis] → [Ge leaching] → [resynthesis with recovered Ge]/[insertion of active sites] using the same material.

IWW/Al_{post} was prepared under optimized alumination conditions reported in ref 17 while varying the concentration of the Ti/Sn source used at the metalation step (0.05–0.45 M) to ensure maximal Ge-for-Ti(Sn) isomorphous substitution without forming extra-framework TiO₂/SnO₂ species inactive in Lewis acid catalyzed reactions.⁴² The XRD patterns of all prepared IWW/Me zeolites revealed the phase purity of the materials, albeit showing diffraction lines with a lower intensity than parent IWW (Figure S6a).

N₂ adsorption/desorption isotherms indicate the microporous character of IWW/Me samples (Figure S6b) and lower values of micropore volume and BET surface area for IWW/Me versus parent IWW (Table 3). In addition, metalation of IWW-5-H₂O-25°C-16h/3 decreased the intensity of the IR band ca. 3560 cm⁻¹ corresponding to the internal silanol groups but did not remove it (Figure S6c). Noticeably, the applied concentrations of the metal source had no effect on the chemical composition (Table 3) and profile of UV-vis spectra (Figure 10) of both IWW/Ti_{post} and IWW/Sn_{post} samples.

FTIR spectroscopy of adsorbed pyridine was used to determine the type, concentration, and strength of acid sites in IWW/Me_{post} zeolites (Table 3). While Py-FTIR spectra of IWW/Al_{post} show the absorption bands (a.b.) characteristic of both Brønsted (a.b. at 1638/1545 cm⁻¹) and Lewis acid sites (a.b. at 1624/1455 cm⁻¹), IWW/Ti_{post} and IWW/Sn_{post} featured exclusively Lewis acid centers (a.b. at 1608-10/1455 cm⁻¹) (Figure S7). In line with previous reports [33, 41], the fraction of Lewis acid sites retaining adsorbed pyridine at high temperature was larger in Sn- than in Ti-substituted IWW (Figure 11a,b). IWW/Al_{post} possessed the strongest Brønsted and Lewis acid centers (Figure 11c).

The number of acid sites determined by Py-FTIR and the chemical composition of IWW/Ti_{post} (Si/Ti_{ICP-OES} = 18 and 20 vs Si/Ti_{py-FTIR} = 23 and 26) and IWW/Sn_{post} (Si/Sn_{ICP-OES} = 30 and 33 vs Si/Sn_{py-FTIR} = 32 and 34) corroborate the results of UV-vis, which revealed that the zeolites contained mostly tetrahedral Ti and Sn atoms, showing a dominant absorption band at 205 nm⁴³ (Figure 10).

Overall, the results indicate incomplete Ge-for-metal substitution during post-synthesis metalation of IWW-5-H₂O-25°C-16h/3. The number of framework metal atoms decreased in the following order: IWW/Al_{post} (Si/Al_{py-FTIR} = 26) = IWW/Ti_{post} (Si/Ti_{py-FTIR} = 23–26) > IWW/Sn_{post} (Si/Sn_{py-FTIR} = 32–34). In turn, post-synthesized IWW/Al_{post} and IWW/Sn_{post} contained a much higher concentration of incorporated metals than directly synthesized Al-IWW_{hydro} and Sn-IWW_{hydro} (Table 3). This result indicates that the atom efficiency of post-synthesis is higher than that of hydrothermal isomorphous substitution in IWW germanosilicate.

Catalytic Behavior of Al-, Ti-, Sn-Substituted IWW Zeolites. The catalytic performance of post-synthesized IWW/Me_{post} zeolites was tested in model reactions, such as (1) THP of 1-hexanol with 3,4-dihydro-2H-pyran (Scheme

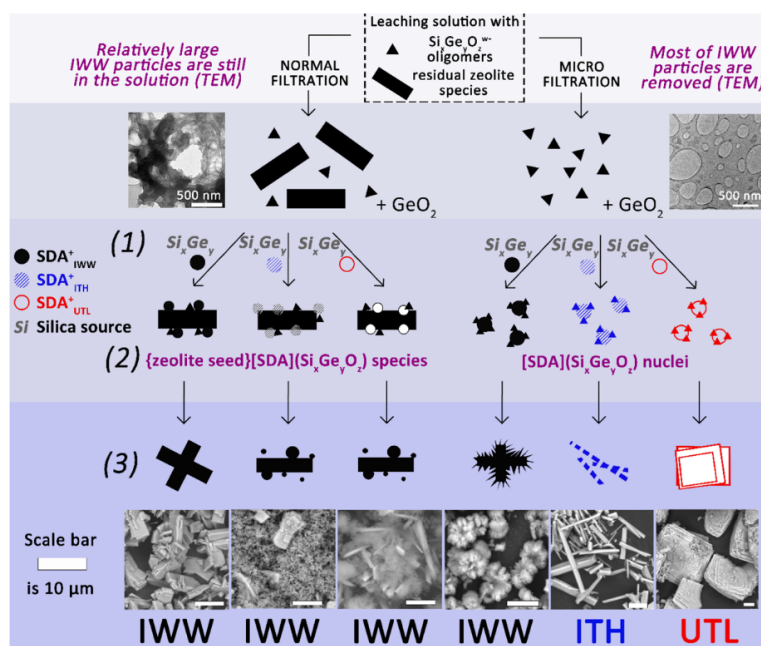
Scheme 3. Plausible Mechanism of Seed-SDA-Assisted Crystallization of Different Germanosilicate Zeolites Using $\text{GeO}_2^{\text{filt}}$ or $\text{GeO}_2^{\text{microfilt}}$ as a Source of Ge.

Table 3. Chemical Composition and Textural and Acidic Properties of Zeolite Catalysts under Study

sample	textural properties		acidic properties, $\mu\text{mol/g}$			Si/Me		Si/Ge
	V_{micro} , cm^3/g	S_{BET} , m^2/g	C_{L}	C_{B}	C_{Σ}	ICP-OES	Py-FTIR	
IWW-5	0.17	474	9		9	5 ^a		5.3
IWW-5- H_2O -25°C-16h/3	0.10	249				70 ^a		70.4
IWW/ $\text{Ti}_{\text{post}}/0.05$ M	0.11	332	680		680	18 ^b	23 ^b	71.3
IWW/ $\text{Ti}_{\text{post}}/0.25$ M	0.11	322	571		571	20 ^b	26 ^b	70.7
TS-1	0.10	510	550		550	28 ^b	29 ^b	
IWW/ $\text{Sn}_{\text{post}}/0.05$ M	0.12	338	490		490	30 ^c	32 ^c	71.8
IWW/ $\text{Sn}_{\text{post}}/0.45$ M	0.12	352	477		477	33 ^c	34 ^c	71.5
Sn-IWW _{hydro}	0.15	420	97		97	101 ^c	171 ^c	3.1
IWW/ Al_{post}	0.15	444	220	170	390	17 ^d	26 ^d	70.4
Al-IWW _{hydro}	0.14	430	170	110	280	25 ^d	36 ^d	4.2

^aSi/Ge. ^bSi/Ti. ^cSi/Sn. ^dSi/Al.

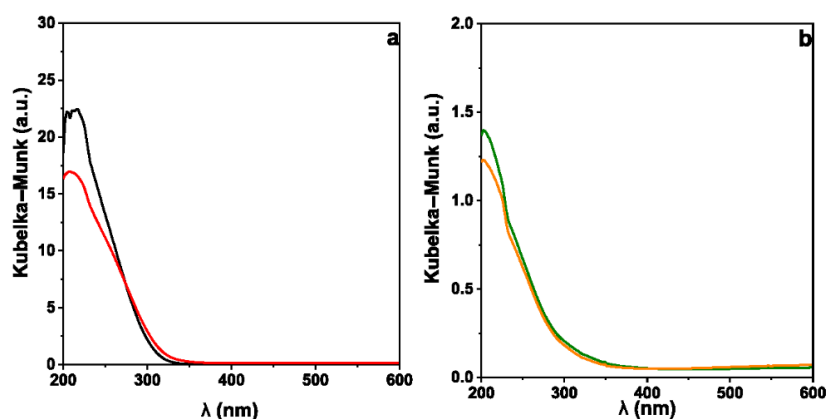


Figure 10. UV-vis spectra of (a) IWW/ $\text{Ti}_{\text{post}}/0.05$ M (red line), IWW/ $\text{Ti}_{\text{post}}/0.25$ M (black line) and (b) IWW/ $\text{Sn}_{\text{post}}/0.05$ M (orange line), IWW/ $\text{Sn}_{\text{post}}/0.45$ M (green line).

4a), which is known to be catalyzed by Brønsted acid sites,⁴⁴
 (2) epoxidation of 1-octene (Scheme 4b) efficiently catalyzed

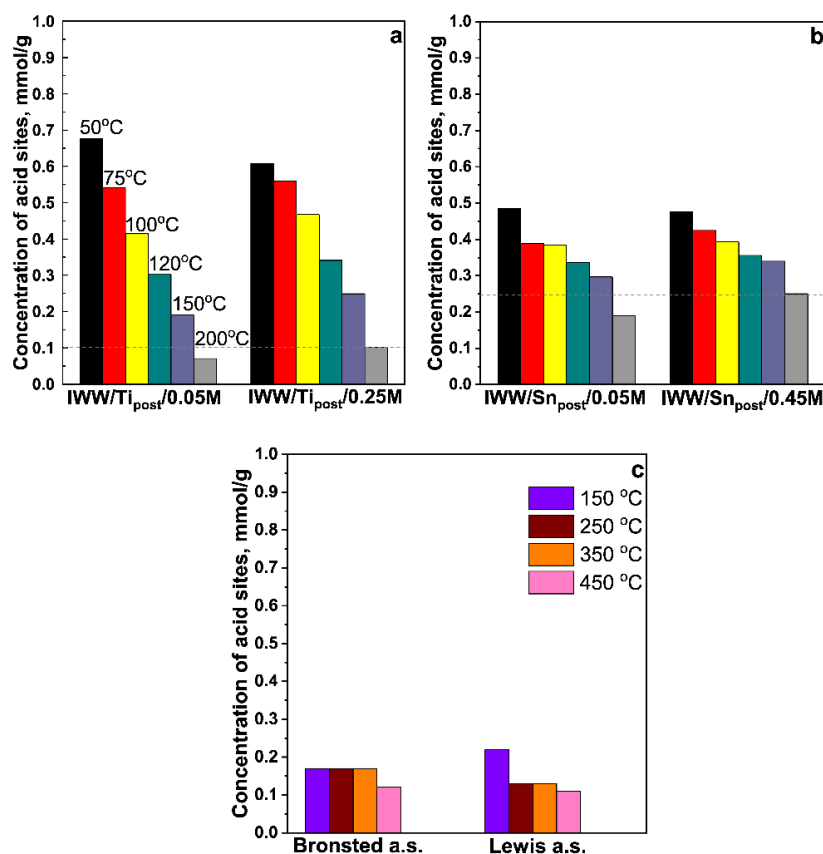
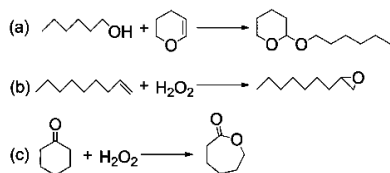


Figure 11. Concentration of acid sites in (a) $\text{IWW}/\text{Ti}_{\text{post}}$ (b) $\text{IWW}/\text{Sn}_{\text{post}}$ and (c) $\text{IWW}/\text{Al}_{\text{post}}$ zeolites retaining adsorbed pyridine at different temperatures.

Scheme 4. Catalytic Reactions: (a) THP of 1-Hexanol, (b) Epoxidation of 1-Octene, and (c) BVO of Cyclohexanone.



by Ti Lewis acid sites, and (3) BVO of cyclohexanone with hydrogen peroxide (Scheme 4c) proceeding on Sn Lewis acid centers.¹⁵

The activities of $\text{IWW}/\text{Me}_{\text{post}}$ were compared with those of hydrothermally synthesized $\text{Al-IWW}_{\text{hydro}}$ and of commercial TS-1 zeolites with close Si/Al and Si/Ti ratios, respectively (Table 3). In turn, the maximal concentration of Sn in $\text{Sn-IWW}_{\text{hydro}}$ (Si/Sn = 101) reached during hydrothermal crystallization was much lower than that reached when using the two-step post-synthesis approach (Si/Sn = 30–33).

$\text{IWW}/\text{Al}_{\text{post}}$ and $\text{IWW}/\text{Ti}_{\text{post}}/0.25$ M catalyzed the selective formation of targeted products in THP of 1-hexanol and epoxidation of 1-octene, respectively (Table 4). In contrast, germanosilicate IWW-5 was inactive in both reactions. The results support the post-synthesis generation of acid sites active in THP and epoxidation reactions upon incorporation of Al and Ti atoms into the IWW framework. On the other hand, in line with a previous study⁴⁵ reporting tetrahedrally coordinated Ge acted as active sites in BVO, both IWW-5 germanosilicate

Table 4. Activities of Me-Substituted Zeolite Catalysts in the Model Acid-Catalyzed Reactions

catalyst	process	targeted product	TOF, h^{-1}
IWW-5	THP	THP ether of 1-hexanol	
$\text{Al-IWW}_{\text{hydro}}$			687 ^a
$\text{IWW}/\text{Al}_{\text{post}}$			987 ^a
IWW-5	epoxidation	1,2-epoxyoctane	
TS-1			81 ^b
$\text{IWW}/\text{Ti}_{\text{post}}/0.25$ M			123 ^b
IWW-5	BVO	ϵ -caprolactone	3 ^c
$\text{Sn-IWW}_{\text{hydro}}$			2 ^d
$\text{IWW}/\text{Sn}_{\text{post}}/0.45$ M			13 ^d

^aReferred to per Al site. ^bReferred to per Ti site. ^cReferred to per Ge site. ^dReferred to per (Ge + Sn) site.

and Sn-containing $\text{IWW}/\text{Sn}_{\text{post}}/0.45$ M catalysts showed selective conversion of cyclohexanone to ϵ -caprolactone.

The conversion versus time profiles for individual catalysts are shown in Figure S8. $\text{IWW}/\text{Me}_{\text{post}}$ (Me = Al, Ti) samples demonstrated higher conversions (100 and 49% after 120 min for $\text{IWW}/\text{Al}_{\text{post}}$ and $\text{IWW}/\text{Ti}_{\text{post}}/0.25$ M, respectively) than hydrothermally synthesized zeolites (52 and 39% for $\text{Al-IWW}_{\text{hydro}}$ and TS-1, respectively). In BVO of cyclohexanone, IWW-5 germanosilicate and Sn-containing $\text{IWW}/\text{Sn}_{\text{post}}/0.45$ M catalysts showed similar conversions of cyclohexanone (Figure S8c). In turn, the TOF number of $\text{IWW}/\text{Sn}_{\text{post}}/0.45$ M was ~ 4 times higher than that of IWW-5 , thus showing the higher activity of tetrahedrally coordinated Sn than that of Ge

sites (Table 4). Enhanced activity of post-synthesized IWW/Ti_{post}/0.25 M (TOF = 123 h⁻¹, Table 4), IWW/Al_{post} (987 h⁻¹), and IWW/Sn_{post}/0.45 M (13 h⁻¹) versus commercial TS-1 (81 h⁻¹) and hydrothermally synthesized Al-IWW_{hydro} (687 h⁻¹) and Sn-IWW_{hydro} (2 h⁻¹) may be explained by a higher accessibility of acid sites in IWW/Me_{post} catalysts because of (i) their smaller crystal sizes (Figure S9); (ii) occurrence of metalation preferentially in the outer part of the crystals, as shown for post-synthesis incorporation of Al or Sn in refs 18 and 46.

CONCLUSIONS

Our detailed study of the effect of treatment conditions and textural properties of germanosilicate zeolites on the degree of Ge leaching from ITH, IWW, and UTL frameworks highlighted the suppression of Ge recovery with the increase in medium acidity and in zeolite crystal size or with the decrease in zeolite pore diameter. Therefore, prolonging the acid treatment results in leaching a higher amount of Ge from medium-pore ITH with a large crystal size (40 × 10 × 5 μm), without affecting the degree of leaching for ITH with smaller crystals (2 × 0.5 × 0.5 μm), large-pore IWW, and extra-large pore UTL zeolites. Optimization of the Ge leaching conditions (e.g., acid nature and concentration and treatment duration) allowed to achieve up to 78–94% Ge recovery from the zeolites under study. Therefore, efficient Ge leaching can be achieved even in water under ambient conditions, which is especially important for potential environmentally friendly applications of this method.

The method for parent zeolite separation from leaching solution (i.e., filtration vs microfiltration) determines the phase selectivity of zeolite formation when reusing extracted GeO₂. The germanium oxide recovered from a given zeolite via microfiltration was efficiently used as a versatile source of Ge, as shown by the synthesis of UTL, ITH, and IWW zeolites, while a “memory effect”, that is, formation of germanosilicates with the topology of the parent zeolite, independently of synthesis conditions, was observed for GeO₂ recovered by filtration.

The results from chemical analysis, Py-FTIR, and catalytic tests reveal that functionalization of the degermanated IWW zeolite by post-synthesis isomorphous substitution is a more atom-efficient method for the incorporation of Al, Ti, and Sn atoms into the zeolite framework than hydrothermal crystallization.

Ultimately, the proposed sequential degermanation–remetalation approach is an effective approach for the cost-efficient preparation of germanosilicate zeolite-based catalysts, which may broaden their use in Brønsted, Lewis, or even bifunctional catalysis after incorporating different metal sites.

ASSOCIATED CONTENT

Supporting Information

The Supporting Information is available free of charge at <https://pubs.acs.org/doi/10.1021/acssuschemeng.0c01336>.

XRD patterns and N₂ adsorption/desorption isotherms of original germanosilicate zeolites; HRTEM images of leaching solution and GeO₂^{filt} and GeO₂^{microfilt} samples; XRD patterns of germanosilicate zeolites before and after acidic leaching; XRD patterns, N₂ adsorption/desorption isotherms, and FTIR spectra of parent IWW, degermanated, and metallated IWW/Me_{post} zeolites;

FTIR spectra of IWW/Me_{post} zeolites retaining adsorbed pyridine at different temperatures; conversion versus time profiles for 1-hexanol in THP reaction, 1-octene in epoxidation reaction, and cyclohexanone in BVO reaction over catalysts under investigation; SEM images of zeolite catalysts under study; and description of Py-FTIR and catalytic experiments (PDF)

AUTHOR INFORMATION

Corresponding Author

Mariya V. Shamzhy – Department of Physical and Macromolecular Chemistry & Charles University Center of Advanced Materials, Faculty of Science, Charles University, 12843 Prague 2, Czech Republic; orcid.org/0000-0002-1979-6817; Email: mariya.shamzhy@natur.cuni.cz

Authors

Jin Zhang – Department of Physical and Macromolecular Chemistry & Charles University Center of Advanced Materials, Faculty of Science, Charles University, 12843 Prague 2, Czech Republic

Qudi Yue – Department of Physical and Macromolecular Chemistry & Charles University Center of Advanced Materials, Faculty of Science, Charles University, 12843 Prague 2, Czech Republic; orcid.org/0000-0003-2046-5238

Michal Mazur – Department of Physical and Macromolecular Chemistry & Charles University Center of Advanced Materials, Faculty of Science, Charles University, 12843 Prague 2, Czech Republic; orcid.org/0000-0001-5044-5284

Maksym Opanasenko – Department of Physical and Macromolecular Chemistry & Charles University Center of Advanced Materials, Faculty of Science, Charles University, 12843 Prague 2, Czech Republic

Jiří Cejka – Department of Physical and Macromolecular Chemistry & Charles University Center of Advanced Materials, Faculty of Science, Charles University, 12843 Prague 2, Czech Republic

Complete contact information is available at: <https://pubs.acs.org/10.1021/acssuschemeng.0c01336>

Notes

The authors declare no competing financial interest.

ACKNOWLEDGMENTS

We thank Dr. Carlos Henrique Vieira Melo for proofreading this manuscript. J.Z. acknowledges the support of the Grant agency of Charles University for the project 243-251284 and Czech Science Foundation for the project 19-21534S. J.Č. acknowledges the support of the Czech Science Foundation to the project EXPRO (19-27551X). M.M., M.O., M.V.S., and J.Č. acknowledge OP VVV “Excellent Research Teams” project no. CZ.02.1.01/0.0/0.0/15_003/0000417—CUCAM.

REFERENCES

- (1) Dorset, D. L.; Strohmaier, K. G.; Kliewer, C. E.; Corma, A.; Diaz-Cabañas, M. J.; Rey, F.; Gilmore, C. J. Crystal Structure of ITQ-26, a 3D Framework with Extra-Large Pores. *Chem. Mater.* **2008**, *20*, 5325–5331.
- (2) Jiang, J.; Jorda, J. L.; Diaz-Cabañas, M. J.; Yu, J.; Corma, A. The Synthesis of an Extra-Large-Pore Zeolite with Double Three-Ring Building Units and a Low Framework Density. *Angew. Chem., Int. Ed.* **2010**, *49*, 4986–4988.

- (3) Paillaud, J.-L.; Harbuzaru, B.; Patarin, J.; Bats, N. Extra-Large-Pore Zeolites with Two-Dimensional Channels Formed by 14 and 12 Rings. *Science* **2004**, *304*, 990–992.
- (4) Kang, J. H.; Xie, D.; Zones, S. I.; Smeets, S.; McCusker, L. B.; Davis, M. E. Synthesis and Characterization of CIT-13, a Germanosilicate Molecular Sieve with Extra-Large Pore Openings. *Chem. Mater.* **2016**, *28*, 6250–6259.
- (5) Zhou, Y.; Kadam, S. A.; Shamzhy, M.; Čejka, J.; Opanasenko, M. Isorecticular UTL-derived zeolites as model materials for probing pore size-activity relationship. *ACS Catal.* **2019**, *9*, 5136–5146.
- (6) Eliášová, P.; Opanasenko, M.; Wheatley, P. S.; Shamzhy, M.; Mazur, M.; Nachtigall, P.; Roth, W. J.; Morris, R. E.; Čejka, J. The ADOR Mechanism for the synthesis of New Zeolites. *Chem. Soc. Rev.* **2015**, *44*, 7177–7206.
- (7) Wheatley, P. S.; Chlubná-Eliášová, P.; Greer, H.; Zhou, W.; Seymour, V. R.; Dawson, D. M.; Ashbrook, S. E.; Pinar, A. B.; McCusker, L. B.; Opanasenko, M.; Čejka, J.; Morris, R. E. Zeolites with Continuously Tuneable Porosity. *Angew. Chem., Int. Ed.* **2014**, *53*, 13210–13214.
- (8) Roth, W. J.; Nachtigall, P.; Morris, R. E.; Wheatley, P. S.; Seymour, V. R.; Ashbrook, S. E.; Chlubná, P.; Grajciar, L.; Položij, M.; Zukal, A.; Shvets, O.; Čejka, J. A Family of Zeolites with Controlled Pore Size Prepared using a Top-Down Method. *Nat. Chem.* **2013**, *5*, 628–633.
- (9) Mazur, M.; Wheatley, P. S.; Navarro, M.; Roth, W. J.; Položij, M.; Mayoral, A.; Eliášová, P.; Nachtigall, P.; Čejka, J.; Morris, R. E. Synthesis of 'unfeasible' zeolites. *Nat. Chem.* **2016**, *8*, 58–62.
- (10) Shamzhy, M.; Opanasenko, M.; Tian, Y.; Konyshva, K.; Shvets, O.; Morris, R. E.; Čejka, J. Germanosilicate Precursors of ADORable Zeolites Obtained by Disassembly of ITH, ITR, and IWR Zeolites. *Chem. Mater.* **2014**, *26*, 5789–5798.
- (11) Chlubná-Eliášová, P.; Tian, Y. Y.; Pinar, A. B.; Kubů, M.; Čejka, J.; Morris, R. E. The Assembly-Disassembly-Organization-Reassembly Mechanism for 3D-2D-3D Transformation of Germanosilicate IWW Zeolite. *Angew. Chem., Int. Ed.* **2014**, *53*, 7048–7052.
- (12) Kasneryk, V.; Shamzhy, M.; Opanasenko, M.; Wheatley, P. S.; Morris, S. A.; Russell, S. E.; Mayoral, A.; Trachta, M.; Čejka, J.; Morris, R. E. Expansion of the ADOR Strategy for the Synthesis of Zeolites: The Synthesis of IPC-12 from Zeolite UOV. *Angew. Chem., Int. Ed.* **2017**, *56*, 4324–4327.
- (13) Kasneryk, V.; Shamzhy, M.; Opanasenko, M.; Wheatley, P. S.; Morris, R. E.; Čejka, J. Insight into the ADOR zeolite-to-zeolite transformation: the UOV case. *Dalton Trans.* **2018**, *47*, 3084–3092.
- (14) Kasneryk, V.; Shamzhy, M.; Zhou, J.; Yue, Q.; Mazur, M.; Mayoral, A.; Luo, Z.; Morris, R. E.; Čejka, J.; Opanasenko, M. Vapour-phase-transport rearrangement technique for the synthesis of new zeolites. *Nat. Commun.* **2019**, *10*, 5129.
- (15) Shamzhy, M.; Opanasenko, M.; Concepción, P.; Martínez, A. New Trends in Tailoring Active Sites in Zeolite-Based Catalysts. *Chem. Soc. Rev.* **2019**, *48*, 1095–1149.
- (16) Gao, F.; Jaber, M.; Bozhilov, K.; Vicente, A.; Fernandez, C.; Valtchev, V. Framework Stabilization of Ge-Rich Zeolites via Postsynthesis Alumination. *J. Am. Chem. Soc.* **2009**, *131*, 16580–16586.
- (17) Shamzhy, M. V.; Eliášová, P.; Vitvarová, D.; Opanasenko, M. V.; Firth, D. S.; Morris, R. E. Post-Synthesis Stabilization of Germanosilicate Zeolites ITH, IWW, and UTL by Substitution of Ge for Al. *Chem.—Eur. J.* **2016**, *22*, 17377–17386.
- (18) Shamzhy, M. V.; Opanasenko, M. V.; Ramos, F. S. d. O.; Brabec, L.; Horáček, M.; Navarro-Rojas, M.; Morris, R. E.; Pastore, H. d. O.; Čejka, J. Post-Synthesis Incorporation of Al into Germanosilicate ITH Zeolites: the Influence of Treatment Conditions on the Acidic Properties and Catalytic Behavior in Tetrahydropyranlation. *Catal. Sci. Technol.* **2015**, *5*, 2973–2984.
- (19) Hussain, A. I.; Palani, A.; Aitani, A. M.; Čejka, J.; Shamzhy, M.; Kubů, M.; Al-Khattaf, S. S. Catalytic cracking of vacuum gasoil over -SVR, ITH, and MFI zeolites as FCC catalyst additives. *Fuel Process. Technol.* **2017**, *161*, 23–32.
- (20) Shamzhy, M.; Ramos, F. S. d. O. Tuning of acidic and catalytic properties of IWR zeolite by post-synthesis incorporation of three-valent elements. *Today* **2015**, *243*, 76–84.
- (21) El-Roz, M.; Lakiss, L.; Vicente, A.; Bozhilov, K. N.; Thibault-Starzyk, F.; Valtchev, V. Ultra-fast framework stabilization of Ge-rich zeolites by low-temperature plasma treatment. *Chem. Sci.* **2014**, *5*, 68–80.
- (22) Kots, P. A.; Sushkevich, V. L.; Tyablikov, O. A.; Ivanova, I. I. Synthesis of Zr-containing BEC-type germanosilicate with high Lewis acidity. *Microporous Mesoporous Mater.* **2017**, *243*, 186–192.
- (23) Sastre, G.; Pulido, A.; Castañeda, R.; Corma, A. Effect of the Germanium Incorporation in the Synthesis of EU-1, ITQ-13, ITQ-22, and ITQ-24 Zeolites. *J. Phys. Chem. B* **2004**, *108*, 8830–8835.
- (24) Castañeda, R.; Corma, A.; Fornés, V.; Rey, F.; Rius, J. Synthesis of a New Zeolite Structure ITQ-24, with Intersecting 10- and 12-Membered Ring Pores. *J. Am. Chem. Soc.* **2003**, *125*, 7820–7821.
- (25) Shvets, O. V.; Shamzhy, M. V.; Yaremov, P. S.; Musilová, Z.; Procházková, D.; Čejka, J. Isomorphous Introduction of Boron in Germanosilicate Zeolites with UTL Topology. *Chem. Mater.* **2011**, *23*, 2573–2585.
- (26) Ren, X.; Liu, J.; Li, Y.; Yu, J.; Xu, R. Hydrothermal Synthesis of an ITH-Type Germanosilicate Zeolite in a Non-Concentrated Gel System. *J. Porous Mater.* **2013**, *20*, 975–981.
- (27) Castañeda, R.; Corma, A.; Fornés, V.; Martíneztriguero, J.; Valencia, S. Direct synthesis of a 9×109×10 member ring zeolite (Al-ITQ-13): A highly shape-selective catalyst for catalytic cracking. *J. Catal.* **2006**, *238*, 79–87.
- (28) Corma, A.; Rey, F.; Valencia, S.; Jordá, J. L.; Rius, J. A Zeolite with Interconnected 8-, 10- and 12-Ring Pores and its Unique Catalytic Selectivity. *Nat. Mater.* **2003**, *2*, 493–497.
- (29) Corma, A.; Rey, F.; Valencia, V.; Martínez, T. Microporous Crystalline Zeolite Material (Zeolite ITQ-22), Synthesis Method Thereof and Use of Same as a Catalyst. U.S. Patent 20,050,182,278 A1, 2008.
- (30) Shamzhy, M. V.; Shvets, O. V.; Opanasenko, M. V.; Yaremov, P. S.; Sarkisyan, L. G.; Chlubná, P.; Zukal, A.; Marthala, V. R.; Hartmann, M.; Čejka, J. Synthesis of Isomorphously Substituted Extra-Large Pore UTL Zeolites. *J. Mater. Chem.* **2012**, *22*, 15793–15803.
- (31) Muniz, F. T. L.; Miranda, M. A. R.; Morilla dos Santos, C.; Sasaki, J. M. The Scherrer equation and the dynamical theory of X-ray diffraction. *Acta Crystallogr., Sect. A: Found. Adv.* **2016**, *72*, 385–390.
- (32) Cychosz, K. A.; Guillet-Nicolas, R.; García-Martínez, J.; Thommes, M. Recent Advances in the Textural Characterization of Hierarchically Structured Nanoporous Materials. *Chem. Soc. Rev.* **2017**, *46*, 389–414.
- (33) Emeis, C. A. Determination of Integrated Molar Extinction Coefficients for Infrared Absorption Bands of Pyridine Adsorbed on Solid Acid Catalysts. *J. Catal.* **1993**, *141*, 347–354.
- (34) Harris, J. W.; Cordon, M. J.; Di Iorio, J. R.; Vega-Vila, J. C.; Ribeiro, F. H.; Gounder, R. Titration and Quantification of Open and Closed Lewis Acid Sites in Sn-Beta Zeolites that Catalyze Glucose Isomerization. *J. Catal.* **2016**, *335*, 141–154.
- (35) Shamzhy, M.; Přeč, J.; Zhang, J.; Ruau, V.; El-Siblani, H.; Mintova, S. Quantification of Lewis acid sites in 3D and 2D TS-1 zeolites: FTIR spectroscopic study. *Catal. Today* **2020**, *345*, 80–87.
- (36) Hammond, C. Intensification Studies of Heterogeneous Catalysts: Probing and Overcoming Catalyst Deactivation During Liquid Phase Operation. *Green Chem.* **2017**, *19*, 2711–2728.
- (37) Corma, A.; Puche, M.; Rey, F.; Sankar, G.; Teat, S. J. A Zeolite Structure (ITQ-13) with Three Sets of Medium-Pore Crossing Channels Formed by 9- and 10-Rings. *Angew. Chem., Int. Ed.* **2003**, *42*, 1156–1159.
- (38) Corma, A.; Díaz-Cabañas, M. J.; Rey, F.; Nicolopoulos, S.; Boulahya, K. ITQ-15: The first ultralarge pore zeolite with a bi-directional pore system formed by intersecting 14- and 12-ring channels, and its catalytic implications. *Chem. Commun.* **2004**, *12*, 1356–1357.

(39) Bartlett, P. N.; Cummings, C. Y.; Levason, W.; Pugh, D.; Reid, G. Halometallate Complexes of Germanium(II) and (IV): Probing the Role of Cation, Oxidation State and Halide on the Structural and Electrochemical Properties. *Chem.—Eur. J.* **2014**, *20*, 5019–5027.

(40) Lim, I. H.; Schrader, W.; Schüth, F. The formation of zeolites from solution - Analysis by mass spectrometry. *Microporous Mesoporous Mater.* **2013**, *166*, 20–36.

(41) Kasneryk, V. I.; Shamzhy, M. V.; Opanasenko, M. V.; Čejka, J. Tuning of Textural Properties of Germanosilicate Zeolites ITH and IWW by Acidic Leaching. *J. Energy Chem.* **2016**, *25*, 318–326.

(42) Luo, H. Y.; Lewis, J. D.; Román-Leshkov, Y. Lewis Acid zeolites for biomass conversion: perspectives and challenges on reactivity, synthesis, and stability. *Annu. Rev. Chem. Biomol. Eng.* **2016**, *7*, 663–692.

(43) Ratnasamy, P.; Srinivas, D.; Knozinger, H. Active Sites and Reactive Intermediates in Titanium Silicate Molecular Sieves. *Adv. Catal.* **2004**, *35*, 1–169.

(44) Liu, M.; Veselý, O.; Eliášová, P.; Shamzhy, M.; Lyu, P.; Grajciar, L. Identification of the Most Active Sites for Tetrahydropyrynylation in Zeolites: MFI as a Test Case. *Catal. Today* **2020**, *345*, 165–174.

(45) Xu, H.; Jiang, J.; Yang, B.; Wu, H.; Wu, P. Effective Baeyer-Villiger oxidation of ketones over germanosilicates. *Catal. Commun.* **2014**, *55*, 83–86.

(46) Dapsens, P. Y.; Mondelli, C.; Jagielski, J.; Hauert, R.; Pérez-Ramírez, J. Hierarchical Sn-MFI zeolites prepared by facile top-down methods for sugar isomerisation. *Catal. Sci. Technol.* **2014**, *4*, 2302–2311.

Toward Controlling Disassembly Step within the ADOR Process for the Synthesis of Zeolites

Jin Zhang, Ondřej Veselý, Zdeněk Tošner, Michal Mazur, Maksym Opanasenko, Jiří Čejka, and Mariya Shamzhy*

Cite This: *Chem. Mater.* 2021, 33, 1228–1237

Read Online

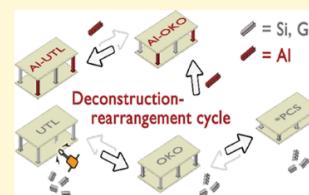
ACCESS |

Metrics & More

Article Recommendations

Supporting Information

ABSTRACT: The application of the Assembly–Disassembly–Organization–Reassembly (ADOR) protocol to the synthesis of germanosilicate zeolites has become a major milestone in material design by enabling the preparation of previously unknown “isoreticular” zeolites with tunable building units (i.e., $-d4r-$, $-s4r-$, $-O-$) connecting crystalline layers. Two processes operating in the disassembly step, deconstructive “deintercalation” and reconstructive “rearrangement”, determine the structure of ADOR-derived zeolites. However, independent management of these key ADOR processes, which would be desirable to regulate the characteristics of the products, has remained elusive thus far. Herein, we report a new method for controlling the primary steps of the ADOR process and present the first example of a “cycled” structural transformation of interlayer units ($d4r \rightarrow s4r \rightarrow d4r$) in the germanosilicate UTL zeolite under “slow deintercalation”/“fast rearrangement” conditions. The “slow deintercalation” mode of ADOR enabled us to prepare the previously known OKO, *PCS, IPC-7 zeolites via gradual reduction of interlayer units in UTL ($d4r \rightarrow d4r/s4r \rightarrow s4r \rightarrow s4r/O-$), in contrast to conventional rearrangement-driven synthesis ($-O- \rightarrow s4r/O- \rightarrow s4r...$). X-ray powder diffraction (XRD), sorption, and solid-state NMR time-resolved studies revealed that the “slow deintercalation/fast rearrangement” modification of ADOR makes it possible to adjust the pore architecture of germanosilicate zeolites toward increasing their micropore size, which has never been achieved before in the classical ADOR mechanism. Therefore, “slow deintercalation” or “slow deintercalation/fast rearrangement” routes provide a tool for controlling the “isoreticular” zeolite structure. Ultimately, the results from this study may facilitate the design of previously predicted but inaccessible members of the ADORable zeolite family.



1. INTRODUCTION

Zeolites are microporous crystalline elementosilicates (E = Al, Ti, Sn, Ge, among others) widely used in adsorption, separation, and catalysis. Hydrothermal crystallization, the traditional method for the preparation of zeolites via a sequence of reversible polymerization/depolymerization steps, has made it possible to synthesize most of the 252 zeolite framework types known thus far.¹ However, the high lattice energies of most theoretically predicted frameworks have precluded the direct synthesis of zeolites with unusual structural and textural characteristics (e.g., those with odd-membered rings).² The recently discovered ADOR strategy (involving Assembly–Disassembly–Organization–Reassembly steps) applicable to germanosilicate zeolites benefits from the irreversibility of the final material-forming step and thus has allowed synthetic chemists to expand the number of zeolites.³ The fascinating chemistry of germanosilicate zeolites, particularly the postsynthesis modification of their framework structure and chemical composition,^{4–8} has been comprehensively reviewed in ref 9

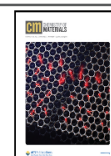
The success of the ADOR approach in the preparation of new zeolites has been already exemplified by the disassembly–organization–reassembly of UTL,^{10,11} UOV,^{12,13} IWW,^{14–16} and *CTH^{17–19} germanosilicate frameworks composed of silica layers connected with Ge-enriched $d4r$ units selectively removable upon hydrolysis (Scheme 1). Studies^{20–22} on UTL

germanosilicate revealed that two key processes operating in the disassembly step determine the structure/pore architecture of a zeolite formed upon ADOR transformation: (i) “deintercalation”, that is, breaking of Ge–O(Ge) or Ge–O(Si) bonds and diffusion of some or all species that left the zeolite framework off the interlayer space and (ii) “rearrangement” of some species, which might not have diffused out of the interlayered space to form various interlayer-connecting units in a “daughter” zeolite. The concentration of water molecules inside the pores plays a key role in both the breaking and making of the T–O bonds in zeolites²³ during the disassembly step. High-water experiments (liquid-to-solid ratio >100 ml/g) have shown that (1) the complete deintercalation of $d4r$ units off UTL framework leading to the IPC-1P layered precursor of PCR zeolite (containing $-O-$ interlayer linkages) is completed within ca. 5 min, regardless of pH and temperature, while (2) rearrangement of IPC-1P (kinetic product of hydrolysis) into an IPC-2P precursor of the OKO zeolite containing $-s4r-$ interlayer

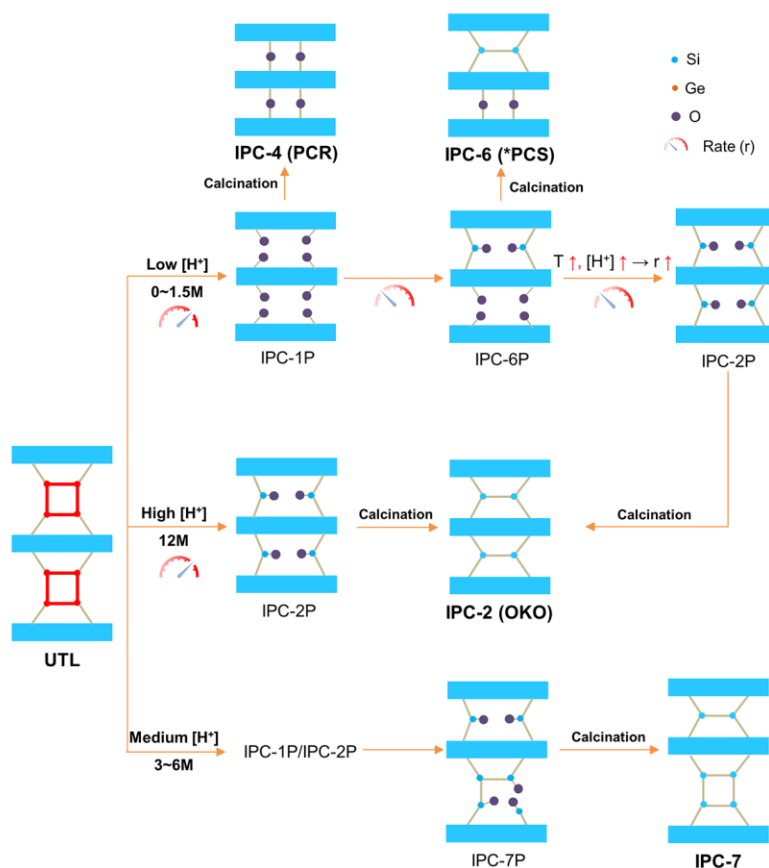
Received: October 12, 2020

Revised: January 20, 2021

Published: February 5, 2021



Scheme 1. Controlling the Rate of Rearrangement within “Fast Deintercalation/Rearrangement” Mode of the ADOR Strategy for the Synthesis of UTL-Derived Zeolites (Based on the Results of Refs 20–22, 24, 26)



linkages (thermodynamic product) proceeds through an IPC-6P intermediate, the precursor of the stage-structured *PCS zeolite containing both PCR- and OKO-type linkages in a 1:1 ratio. The IPC-1P rearrangement has been shown to accelerate with the acidity/temperature (Scheme 1, top).²² Thus, varying the rate of rearrangement process in highly liquid systems by adjusting the pH of UTL disassembly has made it possible to synthesize a series of “isoreticular” zeolites with the same crystalline layers but different connectivity (Scheme 1):^{24–26} 10 × 8-ring PCR, 12 × 10-ring OKO, 12 × 10-ring and 10 × 8-ring *PCS, and 14 × 12-ring and 12 × 10-ring IPC-7.

Although fully hydrolyzing to IPC-1P in high-water experiments, UTL was recently reported to disassemble into IPC-2P when the water-to-solid ratio was decreased to 0.2–50 mL/g.²⁷ The latter, noncomplete UTL disassembly can be related to the deceleration of the Ge–O(Si) bond cleavage with the decrease in the water content (low-water conditions) and to the inhibiting transport of leached species in highly viscous, low-liquid systems. Such species trapped in the interlayer space not only negatively affect the textural characteristics of daughter IPC-*n* zeolites²⁷ but also contribute to the uncontrolled rearrangement of interlayer linkages. Conversely, controlling both deconstructive and reconstructive processes operating on the disassembly step provides a way to synthesize the previously predicted but inaccessible families of “isoreticular” zeolites.^{28,29}

Continuous control over the porosity of the UTL-derived ADORable zeolites is crucial for applications in separation and shape-selective catalysis.²⁴ In contrast to UTL, the fast

“deintercalation/rearrangement” mode of ADOR was not efficient in tuning the interlayer linkages in zeolites formed upon the disassembly of UOV,^{12,13} IWW,¹⁵ ITH, and ITR³⁰ germanosilicates. Herein, we report for the first time the synthesis of UTL-derived “isoreticular” zeolites via a gradual reduction of the *d4r* interlayer units ($d4r \rightarrow d4r/s4r \rightarrow s4r \rightarrow s4r/O-$), a mechanism markedly different from the “fast deintercalation/rearrangement” mode of the ADOR strategy (Scheme 1) that was used so far.^{12,13,17,18,29,30} HCl-induced, slow UTL deintercalation in water-free alcohol medium enabled the preparation of previously known IPC-*n* (*n* = 2, 6, 7) zeolites with typical structural and textural characteristics. In turn, the “slow deintercalation”/“fast rearrangement” regime operating in a water–alcohol medium in the presence of a framework-building element source promoted the “cycled” structural transformation of the interlayer units ($d4r \rightarrow s4r \rightarrow d4r$) in the UTL zeolite. In contrast to classical ADOR, which allows us to control the decrease in the pore size of daughter zeolites (e.g., UTL → IPC-*n* transformation), the approach reported here may be useful for adjusting the pore architecture of germanosilicate zeolites toward increasing their micropore size.

2. EXPERIMENTAL SECTION

2.1. Synthesis of UTL Zeolite. UTL zeolite characterized by Si/Ge = 4.5 was synthesized using SDA of (6R,10S)-6,10-dimethyl-5-azoniaspiro decane (DMAD) hydroxide, according to ref 31. A gel with a composition of 0.67 SiO₂/0.33 GeO₂/0.25DMAD/30 H₂O was heated to 175 °C for 7 days under agitation (60 rpm). The solid products were recovered by filtration, washed with deionized water, and

dried overnight at 70 °C. Then, the zeolites were calcined at 550 °C for 6 h in the air flow.

2.2. Postsynthesis of UTL Zeolite. **2.2.1. Treatment with Water–Alcohol Solutions.** The UTL zeolite was treated with pure alcohol (methanol, ethanol, *i*-propanol) and 20, 40, and 60% solutions of the respective alcohols in water (Table 1).

Table 1. Water–Alcohol Solutions Used for Slow Disassembly of the UTL Zeolite

alcohol concentration, wt %	<i>m</i> (water), g	<i>m</i> (alcohol), g
0	160	0
20	128	32
40	96	64
60	64	96
100	0	160

In total, 160 mL of each solution was heated to 60 °C and 1 g of UTL added. The samples were collected after 1, 3, 5, 18, and 24 h. The solid was separated by centrifugation, washed with pure alcohol (respective to each solution), and dried at room temperature. The dried samples were calcined at 550 °C for 6 h in an air flow.

2.2.2. Treatment with a HCl–Ethanol Solution. The UTL zeolite was treated with a 1.25 M solution of HCl in EtOH (Sigma Aldrich). As the HCl in ethanol is highly flammable at high temperatures, the experiment must be performed at temperatures below 16 °C or in a closed autoclave. To suppress the rearrangement process, we chose to perform the disassembly in an open vessel at 0 °C. Thus, 160 mL of the solution was cooled down to 0 °C and 1 g of UTL added. The samples were collected periodically for 60 days. The solid was separated by centrifugation, washed with absolute ethanol, and dried at room temperature. The dry samples were calcined at 550 °C for 6 h in an air flow.

2.2.3. Treatment with Al-Containing Water–Methanol Solutions. Aluminum nitrate nonahydrate (98%, Aldrich) was used as the Al source. In total, 134 mL of methanol was mixed with 38 mL of water and heated to 60 °C. Then, 34.1 g of aluminum nitrate nonahydrate was dissolved in a water–methanol mixture, subsequently adding 1 g of UTL to 160 mL of the 1 M Al(NO₃)₃ water–methanol solution (water-to-methanol w/w 40/60). The samples were collected periodically for 60 days. The solid was separated by centrifugation, washed with absolute methanol, and dried at room temperature. The dried samples were calcined at 550 °C for 6 h in an air flow.

2.3. Characterization. The structure and crystallinity of the materials were examined by X-ray powder diffraction (XRD) on a Bruker AXS D8 Advance diffractometer with a Vantec-1 detector in the Bragg–Brentano geometry using Cu K α radiation (1.54056 Å). Before the measurements, the samples were ground gently and packed into the holder to decrease the effect of the preferential orientation of individual crystals.

The morphology of the crystals was determined by scanning electron microscopy (TESCAN Vega microscope).

High-resolution transmission electron microscopy (HRTEM) images were acquired using a JEOL NEOARM 200 F microscope equipped with a Schottky-type field emission gun at an accelerating voltage of 200 kV. The samples were ultrasonically dispersed in ethanol and then dropped onto the carbon-coated copper grids before the measurements.

ICP-OES (ThermoScientific iCAP 7000) analysis was used to determine the Si, Ge, and Al content of the materials. For this purpose, a mixture of measured samples (50 mg), HF (1.8 mL), HNO₃ (1.8 mL), and HCl (5.4 mL) were placed in the microwave in a closed vessel at *T* = 140 °C for 35 min. Then, a saturated solution of H₃BO₃ (5.4 mL) was added to ensure the complexation of the excess HF. After digestion, the solutions under analysis were collected in 250 mL flasks, measuring the volume with ultrapure water.

The Ar adsorption/desorption isotherms were collected at –186 °C using a 3Flex (Micromeritics) static volumetric apparatus. All samples were degassed using SmartVac Prep (Micromeritics) at 300 °C under a

vacuum for 8 h before the sorption measurements. The specific surface area was evaluated using the Brunauer–Emmett–Teller (BET) method and the adsorption data in the range of a relative pressure from *p*/*p*⁰ = 0.05–0.25.³² The t-plot method was applied to determine the volume of micropores (*V*_{mic}).³³ The adsorbed amount at a relative pressure *p*/*p*⁰ = 0.975 reflects the total adsorption capacity (*V*_{tot}). The pore size distributions were calculated using the density functional theory (DFT) model.³⁴

Solid-state ²⁷Al NMR spectra were recorded on a Bruker Avance III HD spectrometer working with a 9.4 T standard-bore superconducting magnet (²⁷Al Larmor frequency of 104.26 MHz). The samples were packed into a thin-wall 3.2 mm zirconia rotor and rotated at a MAS rate of 15 kHz using a Bruker 3.2 mm HX CP-MAS probe. A pulse of 1.0 μs (B1 field approximately 95 kHz) with a relaxation delay of 1 s was applied, averaging 2048 transients. The spectra were referenced to a saturated solution of Al(NO₃)₃ in D₂O.

The concentrations of Lewis (cL) and Brønsted (cB) acid sites were determined after pyridine (Py) adsorption, followed by Fourier transform infrared (FTIR) spectroscopy on a Nicolet iS50 spectrometer with a transmission MCT/B detector. The zeolite was pressed into self-supporting wafers with a density of ~10 mg/cm² and activated in situ at 450 °C for 4 h. Pyridine adsorption was performed at 150 °C for 20 min at a partial pressure of 600–800 Pa, followed by desorption for 20 min. Before adsorption, pyridine was degassed in a series of freezing and thawing cycles. All spectra were recorded with a resolution of 4 cm^{–1} by collecting 128 scans for a single spectrum at room temperature. cL and cB values were evaluated from the integral intensities of bands at 1454 cm^{–1} (cL) and at 1545 cm^{–1} (cB) using the molar absorption coefficients $\epsilon(L) = 2.2 \text{ cm}^2/\mu\text{mol}$ and $\epsilon(B) = 1.7 \text{ cm}^2/\mu\text{mol}$.³⁵

3. RESULTS AND DISCUSSION

3.1. From Complete Suppression to Slow Deintercalation: Water–Alcohol Systems. The XRD patterns of the parent UTL zeolite (with Si/Ge = 4.5) and the samples treated with different alcohols (liquid-to-solid ratio = 160 mL/g) showed the same positions and relative intensities of the characteristic diffraction lines (Figure 1), revealing the lack of the disassembly in water-free alcohol medium.

Once the water was added, the UTL zeolite began to transform into IPC-*n* materials (Scheme 1), as revealed by the development of the XRD patterns over time (Figure S1). To assess the effect of the water-to-solid ratio on the progress of the UTL disassembly, the zeolite samples were treated with water–

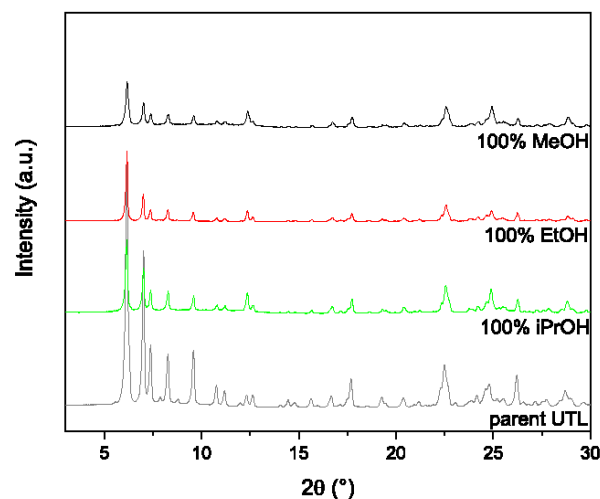


Figure 1. Powder XRD patterns of UTL after 24 h treatment in pure MeOH, EtOH, and *i*PrOH at 60 °C, liquid-to-solid ratio = 160 mL/g.

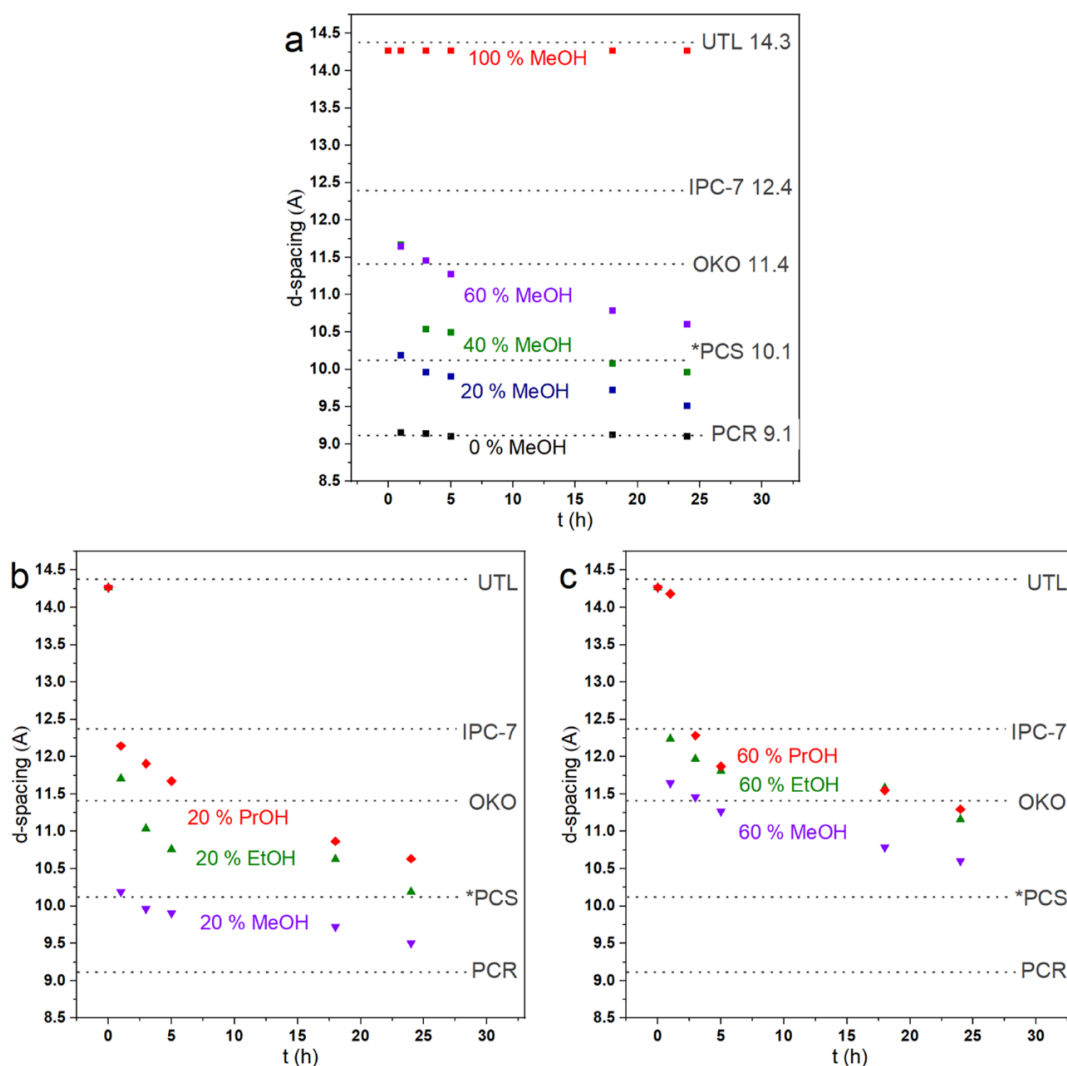


Figure 2. Evolution of the (200) *d*-spacings in zeolites recovered from water–alcohol solutions and subsequently calcined vs MeOH concentration (a) or the type of 20% (b) or 60% alcohol solution (c) at 60 °C; liquid-to-solid ratio = 160 mL/g.

alcohol solutions of different concentrations (Table 1) while keeping the liquid-to-solid ratio high. Figure 2 shows how the interlayer (200) *d*-spacing in calcined samples changes from 14.4 Å (characteristic of UTL) to 11.4 Å (characteristic of OKO), 10.1 Å (characteristic of *PCS), or 9.1 Å (characteristic of PCR), depending on the composition of the liquid medium and on the duration of the treatment. Full deintercalation of *d*4*r* units off the UTL framework with a formation of PCR zeolite (Scheme 1) was observed only in 0% MeOH (water-to-solid ratio = 160 mL/g), while the *PCS zeolite was formed in 20% MeOH (water-to-solid ratio = 128 mL/g) in 1 h (Figure 2a). The lack of PCR-to-*PCS (or OKO) transformation in pure water highlights the efficient suppression of the rearrangement process under the conditions used for this purpose. Decreasing the water-to-solid ratio decelerated the process of UTL-to-*PCS transformation, completed after 1 and 18 h in 20 and 40% MeOH, respectively. The strong effect of the water content on the progress of the UTL disassembly (first shown here under rearrangement-suppressing conditions) univocally demonstrates that even a small change in the water content affects how fast the Ge–O(Si) bonds are cleaved.

The type of alcohol used as a solvent is another factor that affects the time required for the completion of the UTL deintercalation, decreasing in the following sequence (Figure 2b,c): *i*PrOH > EtOH > MeOH. Increasing the kinetic diameter of the alcohol (MeOH (3.6 Å) << EtOH (4.4 Å) < *i*PrOH (4.7 Å)) may limit the formation of the solvation shell around leached Ge species in zeolite pores. Moreover, lowering the polarity of the alcohol in the same sequence (MeOH (0.76) > EtOH (0.65) > *i*PrOH (0.55)) may hinder the transport of leached species from the interlayer space due to the decreased solubility of germanium oxide.³⁶

A stepwise decrease in the zeolite (200) *d*-spacing with treatment time, observed in all studied UTL–water–alcohol systems (Figure 2), suggests that the formation of the IPC-*n* zeolites occurs according to the “slow deintercalation” mechanism, that is, through the gradual reduction of the interlayer units in the germanosilicate zeolite (*d*4*r* → *d*4*r*/*s*4*r* → *s*4*r* → *s*4*r*/-*O*-). In contrast, the previously reported approach for the preparation of the IPC-*n* zeolites is based on the rearrangement of -*O*- units in the rapidly formed IPC-1P layered precursor (i.e., -*O*- → *s*4*r*/-*O*- → *s*4*r* transforma-

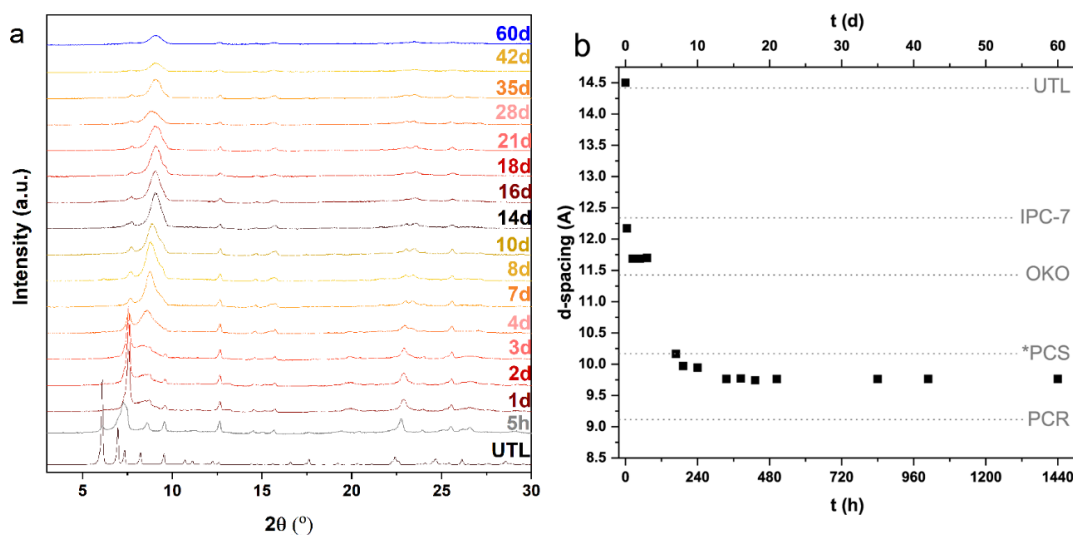


Figure 3. Evolution of powder XRD patterns (a) and the (200) *d*-spacings (b) in IPC-*n* zeolites recovered from an anhydrous HCl/EtOH solution ($T = 0\text{ }^{\circ}\text{C}$) and subsequently calcined.

tion).^{20–22,24,25} The XRD patterns (Figure S1) of IPC-7, OKO, and *PCS zeolites prepared here for the first time via the “slow deintercalation” of UTL in a water–alcohol medium showed phase purity and high crystallinity, albeit with poorer textural properties (Table S1) than their previously reported analogues.^{10,24,25,27,37,38} Lower BET area and micropore volume may be caused by a partial blockage of zeolite pores with leached germanium oxide species.

Considering these preliminary results and the ability of Cl^- anions to break the Ge–O(Si) bonds, thereby forming GeCl_4 , highly soluble in alcohols, the following study has focused on studying the UTL disassembly in a water-free Cl^- –EtOH system.

3.2. Slow Deintercalation at Suppressed Rearrangement: Synthesis of “Isoreticular” Zeolites in Water-Free $[\text{Cl}^-]$ –Ethanol Systems. To control the removal of leached species from the pores of IPC-*n* zeolites while slowing down the breakage of Ge–O(Si) bonds, UTL disassembly was attempted in a water-free ethanolic HCl solution. Importantly, both germanium alkoxychlorides and tetrachloride, formed in such a UTL–HCl/EtOH system, are highly soluble in ethanol. The treatment was performed at a temperature ($T = 0\text{ }^{\circ}\text{C}$) low enough to slow down the rearrangement process.

Analysis of the change in the (200) *d*-spacing of zeolite samples (Figure 3) recovered from the HCl/ethanol medium after 5 h to 10 days highlights the “slow deintercalation” regime of the UTL disassembly. Indeed, similarly to the water–alcohol systems, *d*4*r* interlayer linkages in UTL were gradually destroying to form IPC-7 (5 h), OKO (1–3 days), and finally *PCS (7–10 days) zeolites. The process of UTL-to-*PCS conversion upon low-temperature Cl^- -assisted deintercalation is clearly slower than that of the water-induced disassembly discussed above (Figures 2 and 3). In agreement with the “slow deintercalation” mechanism of IPC-*n* formation and the facile diffusion of the leached Ge species out of the interlayer space in a water-free HCl/ethanol medium, the decrease in the *d*-spacings of “isoreticular” zeolites is accompanied by an increase in the Si/Ge ratio (Table S1): UTL (Si/Ge = 4.5) < IPC-7 (Si/Ge = 6.3) < OKO (Si/Ge = 8.0) < *PCS (Si/Ge = 16.0 after 10 days of the treatment). STEM-EDS map analysis (Figure S2) shows a

uniform distribution of Ge in the parent UTL and treated samples, suggesting that the transformation occurs evenly in crystals. No signs of the final product of UTL deintercalation (PCR zeolite) are detected, but the (200) diffraction line characteristic of the *PCS zeolite decreased in intensity and widened in water-free HCl/ethanol with the prolonging of the treatment, even up to 60 days (Figure 3). The rearrangement process, accelerating with time due to the accumulation of leached species, may explain the stability of *PCS against further deintercalation. This assumption is in line with the increase in the Ge concentration of *PCS samples over time (Si/Ge = 16.0 and 13.4 after 10 and 35 days, respectively).

Consistent with the XRD results, the TEM images of the samples recovered from the UTL–HCl/EtOH system showed layer spacings characteristic of the respective IPC-*n* zeolites. The crystalline material formed after 5 h (Figure 4a) was characterized by lattice fringe separations of 1.4 and 1.2 nm, corresponding to alternate *d*4*r* and *s*4*r* interlayer linkages typical of the IPC-7 zeolite, while the sample treated for 1 day (Figure 4b) exhibited the *d*-spacing corresponding exclusively to *s*4*r* connections of crystalline layers indicative of the OKO zeolite.

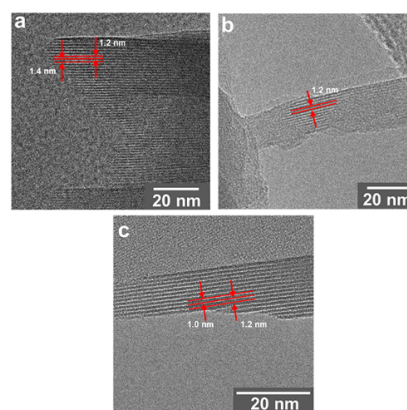


Figure 4. TEM images of the samples recovered from the UTL–anhydrous HCl/EtOH systems after 5 h (a), 1 day (b), and 10 days (c) and subsequently calcined.

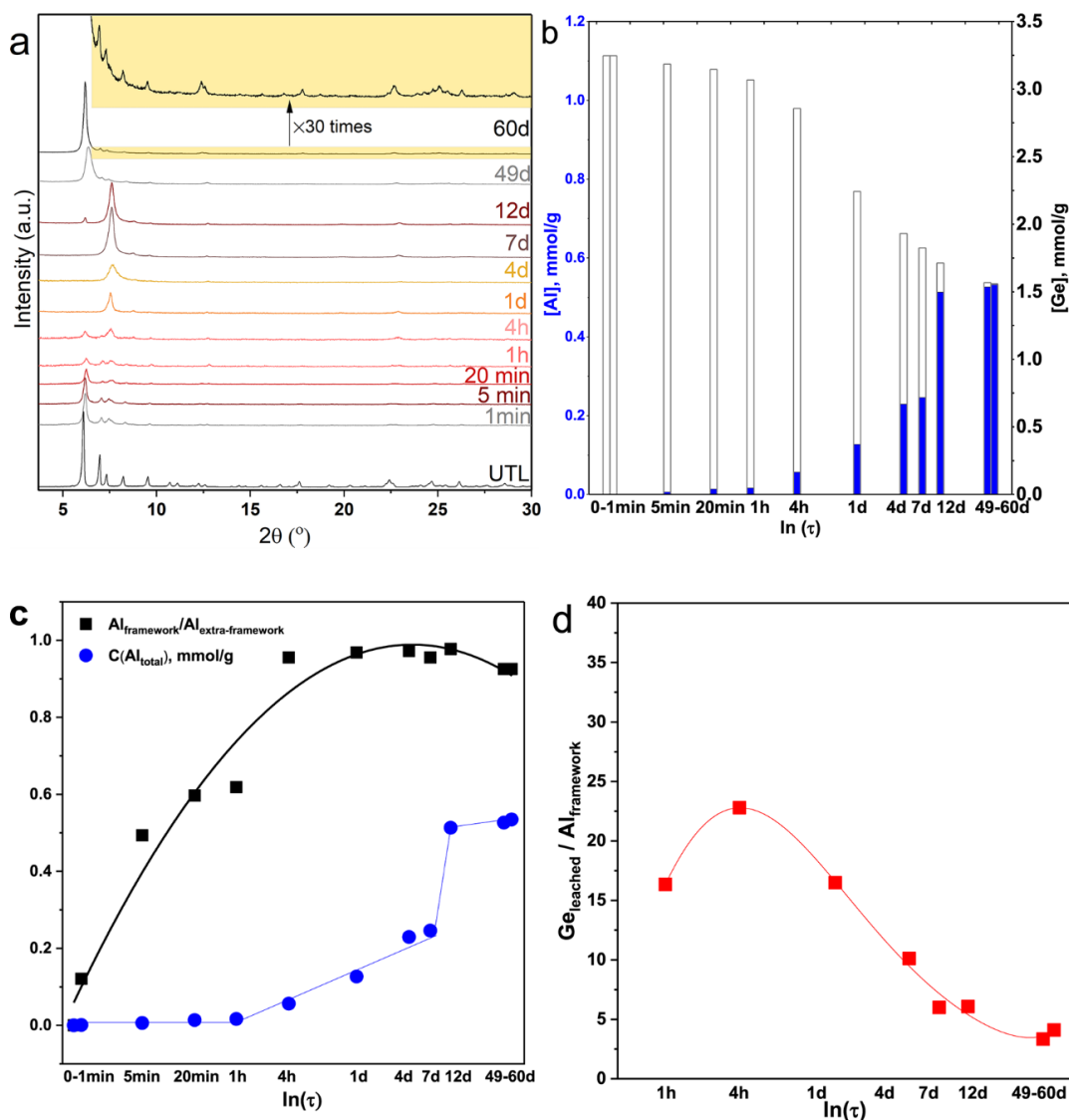


Figure 5. Evolution of XRD patterns (a), Al and Ge contents (b), total concentrations of Al and fractions of framework Al atoms (c), ratios between Ge leached from UTL framework and Al incorporated (d) for the samples recovered from Al-containing water–methanol solution ($T = 60$ °C) and subsequently calcined.

Lastly, the product recovered after 10 days (Figure 4c) demonstrated two distinct interlayer spacings of 1.2 and 1.0 nm characteristic of *PCS. A detailed analysis of the TEM image of stage-structured IPC-7 (Figure S3) revealed a higher ordering of the sample prepared via “slow deintercalation” route than the previously reported analogue formed in 5 M HCl aqueous solution.²⁴ Similarly to ref 24, the *PCS zeolite prepared in this study (Figure S4) showed a small degree of faulting, but the overall ratio of characteristic interlayer spacings in the sample was close to 1:1.

The IPC-*n* zeolites synthesized via a “slow deintercalation” of UTL showed the BET area and micropore volume similar to those of the previously reported analogous zeolites prepared in aqueous HCl solutions via conventional “fast deintercalation/rearrangement” route (Table S1), albeit with a higher Ge content (Si/Ge = 6.3–16 vs 80–100). The chemical composition of these IPC-*n* materials prepared via the “slow deintercalation” of UTL reflects different mechanisms of UTL

disassembly despite leading to the same “isoreticular” zeolites with typical structural and textural properties.

3.3. “Slow Deintercalation/Fast Rearrangement”: Cycled Structural Transformation of UTL in Water–Alcohol Systems Containing a Source of T-Atoms. Controlling the rates of the deintercalation and rearrangement processes within the ADOR strategy is particularly relevant for the rational engineering of new materials. Regulating the rate of the rearrangement at the “fast deintercalation” has already been successfully applied to prepare different UTL-derived ADORable zeolites,^{26,39} but the potential of the rearrangement process to accompany the “slow deintercalation” of germanosilicate zeolites has never been exploited for material design and is therefore addressed below.

In low-water, high-liquid systems (i.e., water–alcohol or HCl/ethanol solutions), sufficiently high concentrations of silicate species involved in the rearrangement process are difficult to reach within a reasonable pH range of stability of

zeolite layers.^{40,41} For this reason, Al was used as an additive to promote the rearrangement of interlayer linkages and (optionally) to generate acid sites in IPC-*n* zeolites. The XRD patterns of the samples recovered after 1 min to 1 h from an Al-containing water–methanol solution were similar to those of the parent UTL zeolite, albeit showing a remarkable decrease in the intensities of diffraction lines (Figure 5a). These results reveal a disordering of the UTL framework. In turn, no change was found in the Ge concentration of the corresponding samples with respect to the parent UTL zeolite (Figure 5b), thus indicating that no Ge leached out of zeolite pores.

The XRD pattern of the material sampled after 4 h contained two visible (200) diffraction lines related to UTL (6.2°) and OKO (7.8°),¹⁰ while prolonging the treatment not only removed the interlayer peak of UTL (after 1 day) but also increased the intensity of the (200) reflection of OKO, peaking after 7 days. After 12 days of treatment, the (200) reflection of OKO decreased sharply and the (200) diffraction line corresponding to UTL recovered. The increase in the intensity and the narrowing of the interlayer reflection over time (12–60 days) indicate an increasing structure ordering in the renovating zeolite. Unprecedentedly, the full restoration of the UTL framework was observed after 60 days under the “slow disassembly”/fast rearrangement conditions applied. It is evident from the XRD pattern of the respective sample showing diffraction lines characteristic of UTL, although of lower intensities and larger widths compared to that of the parent zeolite (Figure 5a). The latter result is consistent with a smaller size of the crystals of zeolite (Figure S5) recovered after long-term treatment. Similarly, the crushing of the zeolite crystals was reported in ref 27 upon mechanochemically assisted hydrolysis of UTL. Consistently with XRD, the TEM images of both the parent and the restored UTL samples demonstrated stacked layers with a 1.4 nm repeat, which is characteristic of UTL (Figure 6).

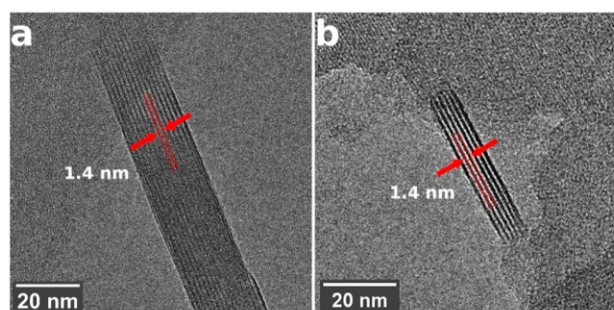


Figure 6. TEM images of the parent UTL zeolite (a) and the sample recovered from an Al-containing water–methanol solution after 60 days and subsequently calcined (b).

The gradual decrease in the Ge content of the zeolite during the 4 h to 12 day period was accompanied by an increase in the Al concentration (Figure 5b). Accordingly, the ²⁷Al MAS NMR spectra (Figure S6) revealed a progressive incorporation of Al atoms into the zeolite frameworks as the intensity of the peak corresponding to the extraframework Al (0 ppm) slightly decreased, while the intensity of the peak assigned to the tetrahedrally coordinated framework Al atoms (~54 ppm) increased markedly (Figure S6). The analysis of the variation of the ratio between Ge leached from the UTL framework and Al incorporated (Figure 5d) shows the delayed character of the

rearrangement process. While the Ge_{leached}/Al_{framework} ratio reached 15–25 during 1–4 h, it gradually decreased over time to 4 after 49–60 days. The UTL-like material restored after 60 days of the treatment had Si/Al = 24 and Si/Ge = 9 and was characterized by the uniform distribution of Al in the crystal, as shown in the STEM-EDS maps (Figure S7).

The structural transformations of UTL in the Al-containing water–methanol system were also highlighted by the change in pore size distribution (PSD; Figure 7a) and micropore volume (Figures 7b and S8). The UTL-to-OKO conversion (20 min to 12 days of the treatment) was reflected in the change from bimodal to monomodal PSD.²⁷ In turn, OKO-to-UTL restoration was accompanied by the re-emergence of the peak related to larger (14-ring) pores in the PSD curve. However, the exact positions and the relative areas of the peaks shown in the PSD curves of the original and restored UTL zeolites should be carefully analyzed because the framework composition and therefore the probe–framework interactions decisive for the evaluation of pore size²⁷ significantly change upon the UTL-to-Al-UTL transformation. The decrease in crystallinity (Figure 5a) and the evident blockage of zeolite pores with Ge species (Figure 5b) match the substantially reduced micropore volumes of the UTL samples after 1–20 min of treatment (from 0.21 cm³/g for the parent UTL to 0.08–0.09 cm³/g; Figure 7b). Increasing the structure ordering of OKO within 1–7 days increased the *V*_{micro} (up to 0.11 cm³/g, which is slightly lower than *V*_{micro} characteristic for the typical OKO samples).^{10,24,25,37,38,42} The renovated Al-UTL-like material surpasses the previously reported Al-substituted UTL zeolites^{7,43–45} with respect to the number of strong Brønsted (0.30 mmol/g) and Lewis (0.20 mmol/g) acid centers (Figure S9) serving as active sites in a number of important catalytic transformations,^{1,46} albeit with a slightly lower *V*_{micro} (0.18 cm³/g) than the values characteristic of the hydrothermally synthesized zeolites (0.19–0.23 cm³/g).^{43–45,47,48}

Overall, the results presented in Figures 5–7 suggest the following plausible mechanism of UTL → Al-OKO → Al-UTL transformation (Scheme 2):

1. Slow hydrolysis of Ge–O(Si) linkages results in the distortion of the UTL framework and temporary blockage of the pore system with the leached Ge species (1 min to 1 h under the conditions used in this study).
2. Progressively leached germanium is removed from the pores and while the concentration of extra-framework Al species increased. The resulting Al-poor OKO zeolite (1 h to 1 day) is characterized by low crystallinity and a high fraction of octahedral Al.
3. Al incorporation into the framework along with self-organization of zeolite layers (1–12 days) leads to higher crystallinity of the resulting Al-enriched OKO zeolite with Al predominantly in framework positions.
4. Al-assisted rearrangement continues at suppressed deintercalation and results in the reconstruction of the *d*4*r* units characteristic of UTL zeolite (12–60 days).

4. CONCLUSIONS

Deintercalation upon germanosilicate zeolite hydrolysis (disassembly) can be efficiently decelerated in water–alcohol or anhydrous HCl–ethanol media. The “slow deintercalation” mode of ADOR was successfully used to synthesize previously known UTL-derived “isoreticular” zeolites with typical structural and textural properties, but with a higher content of Ge. In

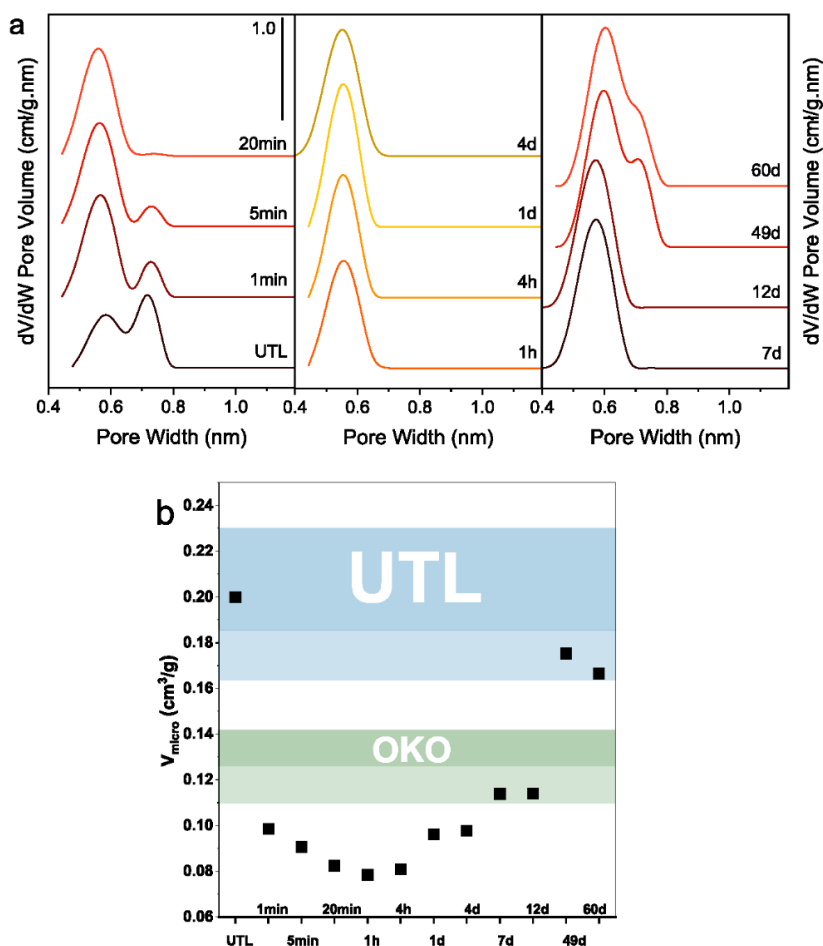
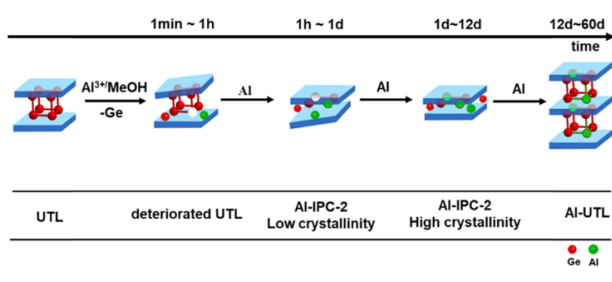


Figure 7. Evolution of the pore-size distribution (a) and micropore volume (b) for the samples recovered from Al-containing water–methanol solutions ($T = 60\text{ }^{\circ}\text{C}$) and subsequently calcined. The ranges of V_{micro} for UTL and OKO zeolites previously reported in the literature^{42,43,47,48} are shown as blue and green rectangles, respectively.

Scheme 2. “Slow Deintercalation/Fast Rearrangement” of UTL Germanosilicate in Al-Containing Water–Methanol Solution



contrast to conventional synthesis of IPC- n materials based on building up the interlayer units ($-O- \rightarrow s4r/-O- \rightarrow s4r...$) in rapidly deintercalated zeolite, the “slow deintercalation” approach enables the preparation of ADORable zeolites via a gradual reduction of original interlayer units ($d4r \rightarrow d4r/s4r \rightarrow s4r \rightarrow s4r/-O-$), a mechanism suitable for the structural transformation of most germanosilicate zeolites.

By promoting heteroelement-induced rearrangement while decelerating the deintercalation in the water–alcohol systems containing a source of T-atoms, we showed for the first time the cycled structural transformation of interlayer units ($d4r \rightarrow s4r \rightarrow$

$d4r$) in the UTL zeolite. This result reveals the potential of “deintercalation/fast rearrangement” modification of ADOR for adjusting the pore architecture of germanosilicate zeolites toward increasing their micropore size. Moreover, heteroatoms efficiently incorporated as potential active sites in the germanosilicate framework (up to 0.5 mmol/g), thereby highlighting the usefulness of this new approach for catalyst engineering.

■ ASSOCIATED CONTENT

Supporting Information

The Supporting Information is available free of charge at <https://pubs.acs.org/doi/10.1021/acs.chemmater.0c03993>.

XRD patterns of UTL zeolites treated with alcohol aqueous solutions; textural characteristics and chemical analysis of IPC- n zeolites; STEM images and EDS mapping of parent UTL and IPC- n zeolites; TEM images of IPC-7 and *PCS zeolites; SEM images and FTIR spectra of parent UTL zeolite and UTL-60d sample recovered from Al-containing water–methanol solution after 60 days; ^{27}Al MAS NMR, STEM images, EDS mapping, and Ar adsorption/desorption isotherms of samples recovered from Al-containing water–methanol solution after 1 min to 60 days (PDF)

AUTHOR INFORMATION

Corresponding Author

Mariya Shamzhy – Department of Physical and Macromolecular Chemistry & Charles University Center of Advanced Materials, Faculty of Science, Charles University, 12843 Prague, Czechia; orcid.org/0000-0002-1979-6817; Email: mariya.shamzhy@natur.cuni.cz

Authors

Jin Zhang – Department of Physical and Macromolecular Chemistry & Charles University Center of Advanced Materials, Faculty of Science, Charles University, 12843 Prague, Czechia

Ondřej Veselý – Department of Physical and Macromolecular Chemistry & Charles University Center of Advanced Materials, Faculty of Science, Charles University, 12843 Prague, Czechia

Zdeněk Tošner – Department of Physical and Macromolecular Chemistry & Charles University Center of Advanced Materials, Faculty of Science, Charles University, 12843 Prague, Czechia

Michal Mazur – Department of Physical and Macromolecular Chemistry & Charles University Center of Advanced Materials, Faculty of Science, Charles University, 12843 Prague, Czechia; orcid.org/0000-0001-5044-5284

Maksym Opanasenko – Department of Physical and Macromolecular Chemistry & Charles University Center of Advanced Materials, Faculty of Science, Charles University, 12843 Prague, Czechia

Jiří Čejka – Department of Physical and Macromolecular Chemistry & Charles University Center of Advanced Materials, Faculty of Science, Charles University, 12843 Prague, Czechia; orcid.org/0000-0003-1400-1031

Complete contact information is available at:

<https://pubs.acs.org/10.1021/acs.chemmater.0c03993>

Notes

The authors declare no competing financial interest.

ACKNOWLEDGMENTS

We thank Dr. Carlos Henrique Vieira Melo for editing this manuscript. This work was supported by the Czech Science Foundation through projects No. 20-12099S (Z.T. and M.S.) and EXPRO No. 19-27551X (O.V. and J.Č.). J.Z. acknowledges the support of the Grant Agency of Charles University for the project 1398119. M.O. thanks the Primus Research Program of the Charles University (project number PRIMUS/17/SCI/22 “Soluble zeolites”). Support by OP VVV “Excellent Research Teams”, project No. CZ.02.1.01/0.0/0.0/15_003/0000417—CUCAM is also acknowledged.

REFERENCES

- (1) Shamzhy, M.; Opanasenko, M.; Concepción, P.; Martínez, A. New trends in tailoring active sites in zeolite-based catalysts. *Chem. Soc. Rev.* **2019**, *48*, 1095–1149.
- (2) Li, X.; Deem, M. W. Why Zeolites Have So Few Seven-Membered Rings. *J. Phys. Chem. C* **2014**, *118*, 15835–15839.
- (3) Eliášová, P.; Opanasenko, M.; Wheatley, P. S.; Shamzhy, M.; Mazur, M.; Nachtigall, P.; Roth, W. J.; Morris, R. E.; Čejka, J. The ADOR mechanism for the synthesis of new zeolites. *Chem. Soc. Rev.* **2015**, *44*, 7177–7206.

(4) Burel, L.; Kasian, N.; Tuel, A. Quasi All-Silica Zeolite Obtained by Isomorphous Degermanation of an As-Made Germanium-Containing Precursor. *Angew. Chem., Int. Ed.* **2014**, *53*, 1360–1363.

(5) Xu, H.; Jiang, J. G.; Yang, B. T.; Zhang, L.; He, M. Y.; Wu, P. Post-Synthesis Treatment gives Highly Stable Siliceous Zeolites through the Isomorphous Substitution of Silicon for Germanium in Germanosilicates. *Angew. Chem., Int. Ed.* **2014**, *53*, 1355–1359.

(6) Liu, X.; Xu, H.; Zhang, L.; Han, L.; Jiang, J. G.; Oleynikov, P.; Chen, L.; Wu, P. Isomorphous Incorporation of Tin Ions into Germanosilicate Framework Assisted by Local Structural Rearrangement. *ACS Catal.* **2016**, *6*, 8420–8431.

(7) Shamzhy, M. V.; Eliášová, P.; Vitvarová, D.; Opanasenko, M. V.; Firth, D. S.; Morris, R. E. Post-Synthesis Stabilization of Germanosilicate Zeolites ITH, IWW, and UTL by Substitution of Ge for Al. *Chem. Eur. J.* **2016**, *22*, 17377–17386.

(8) Opanasenko, M.; Parker, W. O.; Shamzhy, M.; Montanari, E.; Bellettato, M.; Mazur, M.; Millini, R.; Čejka, J. Hierarchical Hybrid Organic-Inorganic Materials with Tunable Textural Properties Obtained Using Zeolitic-Layered Precursor. *J. Am. Chem. Soc.* **2014**, *136*, 2511–2519.

(9) Opanasenko, M.; Shamzhy, M.; Wang, Y.; Yan, W.; Nachtigall, P.; Čejka, J. Synthesis and Post-Synthesis Transformation of Germanosilicate Zeolites. *Angew. Chem., Int. Ed.* **2020**, *59*, 19380–19389.

(10) Roth, W. J.; Nachtigall, P.; Morris, R. E.; Wheatley, P. S.; Seymour, V. R.; Ashbrook, S. E.; Chlubná, P.; Grajciar, L.; Polozij, M.; Zukal, A.; Shvets, O.; Čejka, J. A family of zeolites with controlled pore size prepared using a top-down method. *Nat. Chem.* **2013**, *5*, 628–633.

(11) Mazur, M.; Wheatley, P. S.; Navarro, M.; Roth, W. J.; Polozij, M.; Mayoral, A.; Eliášová, P.; Nachtigall, P.; Čejka, J.; Morris, R. E. Synthesis of ‘unfeasible’ zeolites. *Nat. Chem.* **2016**, *8*, 58–62.

(12) Kasneryk, V.; Shamzhy, M.; Opanasenko, M.; Wheatley, P. S.; Morris, S. A.; Russell, S. E.; Mayoral, A.; Trachta, M.; Čejka, J.; Morris, R. E. Expansion of the ADOR Strategy for the Synthesis of Zeolites: The Synthesis of IPC-12 from Zeolite UOV. *Angew. Chem., Int. Ed.* **2017**, *56*, 4324–4327.

(13) Kasneryk, V.; Shamzhy, M.; Opanasenko, M.; Wheatley, P. S.; Morris, R. E.; Čejka, J. Insight into the ADOR zeolite-to-zeolite transformation: the UOV case. *Dalton Trans.* **2018**, *47*, 3084–3092.

(14) Chlubná-Eliášová, P.; Tian, Y. Y.; Pinar, A. B.; Kubů, M.; Čejka, J.; Morris, R. E. The Assembly-Disassembly-Organization-Reassembly Mechanism for 3D-2D-3D Transformation of Germanosilicate IWW Zeolite. *Angew. Chem., Int. Ed.* **2014**, *53*, 7048–7052.

(15) Kasneryk, V.; Shamzhy, M.; Zhou, J.; Yue, Q.; Mazur, M.; Mayoral, A.; Luo, Z.; Morris, R. E.; Čejka, J.; Opanasenko, M. Vapour-phase-transport rearrangement technique for the synthesis of new zeolites. *Nat. Commun.* **2019**, *10*, No. 5129.

(16) Lu, K.; Huang, J.; Jiao, M.; Zhao, Y.; Ma, Y.; Jiang, J.; Xu, H.; Ma, Y.; Wu, P. Topotactic conversion of Ge-rich IWW zeolite into IPC-18 under mild condition. *Microporous Mesoporous Mater.* **2021**, *310*, No. 110617.

(17) Firth, D. S.; Morris, S. A.; Wheatley, P. S.; Russell, S. E.; Slawin, A. M. Z.; Dawson, D. M.; Mayoral, A.; Opanasenko, M.; Polozij, M.; Čejka, J.; Nachtigall, P.; Morris, R. E. Assembly-Disassembly-Organization-Reassembly Synthesis of Zeolites Based on cfi-Type Layers. *Chem. Mater.* **2017**, *29*, 5605–5611.

(18) Liu, X.; Mao, W.; Jiang, J.; Lu, X.; Peng, M.; Xu, H.; Han, L.; Che, S.-A.; Wu, P. Topotactic Conversion of Alkali-Treated Intergrown Germanosilicate CIT-13 into Single-Crystalline ECNU-21 Zeolite as Shape-Selective Catalyst for Ethylene Oxide Hydration. *Chem. Eur. J.* **2019**, *25*, 4520–4529.

(19) Kang, J. H.; Xie, D.; Zones, S. L.; Davis, M. E. Transformation of Extra-Large Pore Germanosilicate CIT-13 Molecular Sieve into Extra-Large Pore CIT-5 Molecular Sieve. *Chem. Mater.* **2019**, *31*, 9777–9787.

(20) Morris, S. A.; Bignami, G. P. M.; Tian, Y.; Navarro, M.; Firth, D. S.; Čejka, J.; Wheatley, P. S.; Dawson, D. M.; Slawinski, W. A.; Wragg, D. S.; Morris, R. E.; Ashbrook, S. E. In situ solid-state NMR and XRD studies of the ADOR process and the unusual structure of zeolite IPC-6. *Nat. Chem.* **2017**, *9*, 1012–1018.

- (21) Henkelis, S. E.; Morris, S. A.; Mazur, M.; Wheatley, P. S.; McHugh, L. N.; Morris, R. E. Monitoring the assembly–disassembly–organisation–reassembly process of germanosilicate UTL through in situ pair distribution function analysis. *J. Mater. Chem. A* **2018**, *6*, 17011–17018.
- (22) Henkelis, S. E.; Mazur, M.; Rice, C. M.; Wheatley, P. S.; Ashbrook, S. E.; Morris, R. E. Kinetics and Mechanism of the Hydrolysis and Rearrangement Processes within the Assembly–Disassembly–Organization–Reassembly Synthesis of Zeolites. *J. Am. Chem. Soc.* **2019**, *141*, 4453–4459.
- (23) Heard, C. J.; Grajciar, L.; Uhlík, F.; Shamzhy, M.; Opanasenko, M.; Čejka, J.; Nachtigall, P. Zeolite (In)Stability under Aqueous or Steaming Conditions. *Adv. Mater.* **2020**, *32*, No. 2003264.
- (24) Wheatley, P. S.; Chlubná-Elišásová, P.; Greer, H.; Zhou, W. Z.; Seymour, V. R.; Dawson, D. M.; Ashbrook, S. E.; Pinar, A. B.; McCusker, L. B.; Opanasenko, M.; Čejka, J.; Morris, R. E. Zeolites with Continuously Tuneable Porosity. *Angew. Chem., Int. Ed.* **2014**, *53*, 13210–13214.
- (25) Verheyen, E.; Joos, L.; Van Havenbergh, K.; Breynaert, E.; Kasian, N.; Gobechiya, E.; Houthoofd, K.; Martineau, C.; Hinterstein, M.; Taulelle, F.; Van Speybroeck, V.; Waroquier, M.; Bals, S.; Van Tendeloo, G.; Kirschhock, C. E. A.; Martens, J. A. Design of zeolite by inverse sigma transformation. *Nat. Mater.* **2012**, *11*, 1059–1064.
- (26) Henkelis, S. E.; Mazur, M.; Rice, C. M.; Bignami, G. P. M.; Wheatley, P. S.; Ashbrook, S. E.; Čejka, J.; Morris, R. E. A procedure for identifying possible products in the assembly–disassembly–organization–reassembly (ADOR) synthesis of zeolites. *Nat. Protoc.* **2019**, *14*, 781–794.
- (27) Rainer, D. N.; Rice, C. M.; Warrender, S. J.; Ashbrook, S. E.; Morris, R. E. Mechanochemically assisted hydrolysis in the ADOR process. *Chem. Sci.* **2020**, *11*, 7060–7069.
- (28) Trachta, M.; Bludský, O.; Čejka, J.; Morris, R. E.; Nachtigall, P. From Double-Four-Ring Germanosilicates to New Zeolites: In Silico Investigation. *ChemPhysChem* **2014**, *15*, 2972–2976.
- (29) Hermann, J.; Trachta, M.; Nachtigall, P.; Bludský, O. Theoretical investigation of layered zeolite frameworks: Surface properties of 2D zeolites. *Catal. Today* **2014**, *227*, 2–8.
- (30) Shamzhy, M.; Opanasenko, M.; Tian, Y. Y.; Konyshaya, K.; Shvets, O.; Morris, R. E.; Čejka, J. Germanosilicate Precursors of ADORable Zeolites Obtained by Disassembly of ITH, ITR, and IWR Zeolites. *Chem. Mater.* **2014**, *26*, 5789–5798.
- (31) Shvets, O. V.; Shamzhy, M. V.; Yaremov, P. S.; Musilova, Z.; Procházková, D.; Čejka, J. Isomorphous Introduction of Boron in Germanosilicate Zeolites with UTL Topology. *Chem. Mater.* **2011**, *23*, 2573–2585.
- (32) Brunauer, S.; Emmett, P. H.; Teller, E. Adsorption of Gases in Multimolecular Layers. *J. Am. Chem. Soc.* **1938**, *60*, 309–319.
- (33) Lippens, B. C.; de Boer, J. H. Studies on pore systems in catalysts: V. The t method. *J. Catal.* **1965**, *4*, 319–323.
- (34) Jagiello, J.; Thommes, M. Comparison of DFT characterization methods based on N₂, Ar, CO₂, and H₂ adsorption applied to carbons with various pore size distributions. *Carbon* **2004**, *42*, 1227–1232.
- (35) Emeis, C. A. Determination of Integrated Molar Extinction Coefficients for Infrared Absorption Bands of Pyridine Adsorbed on Solid Acid Catalysts. *J. Catal.* **1993**, *141*, 347–354.
- (36) Hohman, J. N.; Kim, M.; Bednar, H. R.; Lawrence, J. A.; McClanahan, P. D.; Weiss, P. S. Simple, robust molecular self-assembly on germanium. *Chem. Sci.* **2011**, *2*, 1334–1343.
- (37) Zukal, A.; Shamzhy, M.; Kubů, M.; Čejka, J. The effect of pore size dimensions in isoreticular zeolites on carbon dioxide adsorption heats. *J. CO₂ Util.* **2018**, *24*, 157–163.
- (38) Jagiello, J.; Sterling, M.; Eliášová, P.; Opanasenko, M.; Zukal, A.; Morris, R. E.; Navaro, M.; Mayoral, A.; Crivelli, P.; Warringham, R.; Mitchell, S.; Perez-Ramírez, J.; Čejka, J. Structural analysis of IPC zeolites and related materials using positron annihilation spectroscopy and high-resolution argon adsorption. *Phys. Chem. Chem. Phys.* **2016**, *18*, 15269–15277.
- (39) Bignami, G. P. M.; Dawson, D. M.; Seymour, V. R.; Wheatley, P. S.; Morris, R. E.; Ashbrook, S. E. Synthesis, Isotopic Enrichment, and Solid-State NMR Characterization of Zeolites Derived from the Assembly, Disassembly, Organization, Reassembly Process. *J. Am. Chem. Soc.* **2017**, *139*, 5140–5148.
- (40) Iler, R. K.; K, I. R. *The Chemistry of Silica: Solubility, Polymerization, Colloid and Surface Properties and Biochemistry of Silica*; Wiley, 1979; pp 30–49.
- (41) Baes, C. F.; Mesmer, R. E., *The Hydrolysis of Cations*; Wiley, 1976, pp 112–349.
- (42) Zhou, Y.; Kadam, S. A.; Shamzhy, M.; Čejka, J.; Opanasenko, M. Isoreticular UTL-Derived Zeolites as Model Materials for Probing Pore Size–Activity Relationship. *ACS Catal.* **2019**, *9*, 5136–5146.
- (43) Shamzhy, M. V.; Shvets, O. V.; Opanasenko, M. V.; Yaremov, P. S.; Sarkisyan, L. G.; Chlubna, P.; Zukal, A.; Marthala, V. R.; Hartmann, M.; Čejka, J. Synthesis of isomorphously substituted extra-large pore UTL zeolites. *J. Mater. Chem.* **2012**, *22*, 15793–15803.
- (44) Shamzhy, M. V.; Shvets, O. V.; Opanasenko, M. V.; Kurfirtova, L.; Kubicka, D.; Čejka, J. Extra-Large-Pore Zeolites with UTL Topology: Control of the Catalytic Activity by Variation in the Nature of the Active Sites. *Chemcatchem* **2013**, *5*, 1891–1898.
- (45) Žilková, N.; Shamzhy, M.; Shvets, O.; Čejka, J. Transformation of aromatic hydrocarbons over isomorphously substituted UTL: Comparison with large and medium pore zeolites. *Catal. Today* **2013**, *204*, 22–29.
- (46) Přeč, J.; Pizarro, P.; Serrano, D. P.; Čejka, J. From 3D to 2D zeolite catalytic materials. *Chem. Soc. Rev.* **2018**, *47*, 8263–8306.
- (47) Paillaud, J. L.; Harbuzaru, B.; Patarin, J.; Bats, N. Extra-large-pore zeolites with two-dimensional channels formed by 14 and 12 rings. *Science* **2004**, *304*, 990–992.
- (48) Corma, A.; Diaz-Cabanas, M. J.; Rey, F.; Nicolououlas, S.; Boulahya, K. ITQ-15: The first ultralarge pore zeolite with a bi-directional pore system formed by intersecting 14- and 12-ring channels, and its catalytic implications. *Chem. Commun.* **2004**, *12*, 1356–1357.

Cite this: *Catal. Sci. Technol.*, 2020,
10, 8254

Solvent-free ketalization of polyols over germanosilicate zeolites: the role of the nature and strength of acid sites†

Lunia Podolean,^a Jin Zhang,^b Mariya Shamzhy,^b
Vasile I. Pârvulescu ^{*a} and Jiří Čejka ^b

Isomorphous substitution of silicon for germanium affords germanosilicate zeolites with weak acid centers capable of catalyzing key reactions such as Baeyer–Villiger oxidation of ketones and etherification of levulinic acid. Herein, we show for the first time that UTL (Si/Ge = 4.2) and IWW (Si/Ge = 7.2) germanosilicate zeolites are active and selective catalysts of polyol (e.g., ethylene glycol, glycerol and 1,4-butanediol) ketalization to dioxolanes. Large-pore IWW outperformed the extra-large-pore UTL zeolite in the ketalization of polyols, thus indicating diffusion limitations in bulky platelet-like UTL crystals. FTIR spectroscopy of adsorbed pyridine revealed the Lewis acidity of the UTL zeolite, whereas the more active IWW catalyst was characterized by water-induced Brønsted acidity. Increasing the activation temperature (200–450 °C) reduced the concentration of Brønsted acid centers in the IWW germanosilicate (i.e., 0.16; 0.07 and 0.05 mmol g⁻¹ for T_{act} = 200, 300 and 450 °C, respectively) but increased the number of Lewis acid sites in both zeolites. Under optimized reaction conditions (e.g., acetone/glycerol = 25, T_{act} = 300 °C), almost total transformation of glycerol into solketal was achieved within 3 h of reaction time over the IWW zeolite at room temperature (>99% yield of the target product). The results from the present study clearly show that weak acid centers of germanosilicate zeolites can serve as active sites in ketalization reactions.

Received 23rd August 2020,
Accepted 10th October 2020

DOI: 10.1039/d0cy01662d

rsc.li/catalysis

Introduction

Large- and especially extra-large-pore zeolites had been highly targeted but rarely obtained as synthesis products until researchers recognized the structure-directing ability of germanium towards the formation of frameworks with small *d4r* and *d3r* units.^{1,2} Following this strategy, new low-framework density structures such as BEC,³ IWS,⁴ ITV⁵ and UTL,^{6,7} among others, were successfully synthesized. However, germanosilicates have two significant limitations: the high cost of Ge and their low hydrothermal stability.^{2,8,9} Nevertheless, the high lability of Si–O–Ge and Ge–O–Ge linkages in acid/neutral aqueous media and the preferential location of Ge atoms in *d4r* units of UTL,^{10–12} UOV,^{13,14}

IWW^{15,16} and *CTH¹⁷ have been recently exploited for controllable framework disassembly, thereby enabling the top-down synthesis of 2D precursors of new 3D zeolites.¹ Moreover, the post-synthesis substitution of Ge by other three^{18,19} or tetravalent elements^{20–23} combined with recovery and recycling of leached germanium²⁴ generates acid sites of variable strength while enhancing the hydrolytic stability and reducing the cost of such zeolites. Thus, for Ge-poor zeolites (Si/Ge > 20), instability is no longer a critical issue.

Despite recent achievements in the design of germanosilicate zeolites, these prospective materials have only been used as catalysts in a limited number of applications. Among these materials, germanosilicate zeolites with UTL, IWW and EWO structures were found to catalyze the Baeyer–Villiger oxidation of 2-adamantanone,²² esterification of levulinic acid,²⁵ and hydration of ethylene oxide to ethylene glycol.²⁶ Notwithstanding these recent advances highlighting the catalytic activity of germanosilicate zeolites, our knowledge of the nature of active sites in these catalysts remains limited. In addition, the scarce information on the acidity of specific germanosilicate zeolites is controversial. For example, Kasian *et al.* detected both Brønsted and Lewis acid sites in the UTL zeolite,²⁷ whereas other studies based on FTIR characterization suggested only the presence of Lewis acidity.^{7,28}

^a Faculty of Chemistry, Department of Organic Chemistry, Biochemistry and Catalysis, University of Bucharest, 4-12 Regina Elisabeta Av., S3, 030018 Bucharest, Romania. E-mail: vasile.parvulescu@chimie.unibuc.ro

^b Department of Physical and Macromolecular Chemistry & Charles University Center of Advanced Materials, Faculty of Science, Charles University, Hlavova 8, 12843 Prague, Czechia. E-mail: jiri.cejka@natur.cuni.cz

† Electronic supplementary information (ESI) available: S1: ¹H and ¹³C NMR spectra of the reaction product (Fig. 8); S2: FTIR spectra of the IWW zeolite subjected to dose-by-dose adsorption of water, followed by saturation with pyridine; S3: variation of conversion with molecule size. See DOI: 10.1039/d0cy01662d

Glycerol acetalization with aldehydes and ketones is especially important for using overproduced biodiesel glycerols to synthesize cyclic acetals and ketals^{29–31} as prospective fuel additives.³² Glycerol ketalization with acetone is generally performed in the presence of a Brønsted or Lewis acid catalyst (Scheme 1), yielding two products: the target 2,2-dimethyl-4-hydroxymethyl-1,3-dioxolane (solketal) and 2,2-dimethyl-1,3-dioxan-5-ol.

Solketal is used as 1) an additive to improve oxidation stability and the octane number of liquid fuels, 2) a versatile solvent and a plasticizer in the polymer industry and 3) a solubilizing and suspending agent in pharmaceutical preparations, as recently reported.³² To date, different types of solid acids with strong acid sites such as aluminosilicate zeolites,³³ heteropolyacids^{34–36} and MOFs³⁷ have proved their ability to catalyze the acetalization of aldehydes and ketones.

The state of the art described above thus encouraged us to further investigate the catalytic performance of weak acidic germanosilicate zeolites, including **IWW** and **UTL**. The surprisingly high catalytic activity of both germanosilicates in the liquid-phase ketalization of glycerol under solvent-free conditions prompted us to perform this detailed investigation of the zeolite structure and acidity effect on the reaction outcome. For this purpose, here we address the catalytic performances of **IWW** and **UTL** germanosilicates and of the commercial large-pore aluminosilicate zeolites beta (**BEA**) and mordenite (**MOR**) in the ketalization of different polyols in relation to the structural and acidic properties of the catalysts by XRD, N₂ adsorption/desorption, SEM, and FTIR spectroscopy of adsorbed pyridine.

Experimental

Synthesis of zeolites

Structure-directing agents (SDAs). 1,5-Bis-(methylpyrrolidinium)pentane dihydroxide (MPP(OH)₂) and (6*R*,10*S*)-6,10-dimethyl-5-azoniaspirodecane hydroxide (DMAD(OH)) were prepared according to ref. 38 and 39.

Hydrothermal synthesis. The **IWW** zeolite sample was synthesized using MPP(OH)₂ as the SDA according to Corma *et al.*³⁸ The gel with a composition of 0.80 SiO₂:0.20 GeO₂:0.25 MPP(OH)₂:15 H₂O was transferred into a Teflon-lined autoclave and heated to 175 °C for 7 days.

The **UTL** zeolite was synthesized according to ref. 40. A gel with a composition of 0.67 SiO₂:0.33 GeO₂:0.25 DMAD(OH):30 H₂O was heated to 175 °C for 7 days under agitation (60 rpm). The solid products were then recovered by filtration, washed with deionized water, and dried overnight at 70 °C. Finally, the **IWW** and **UTL** zeolites were calcined in an air

flow at 580 and 550 °C, respectively. The calcination time was 6 h, whereas the temperature ramp was 1 °C min⁻¹.

Characterization

The phase purity of the zeolites was examined by X-ray powder diffraction (XRD) using a Bruker AXS-D8 Advance diffractometer with a graphite monochromator and a position-sensitive detector (Vântec-1) using CuKα radiation ($\lambda = 1.5418 \text{ \AA}$, 40 kV, 40 mA) in the Bragg–Brentano geometry at a scan rate of 0.25° (2 θ) min⁻¹ in the 3–40° 2 θ range. The samples were ground gently and carefully packed into a holder before the measurement.

The size and morphology of the zeolite crystals were examined by scanning electron microscopy (SEM, JEOL JSM-5500LV microscope). For these measurements, the crystals were coated with a thin layer of platinum (~10 nm) using a BAL-TEC SCD-050 instrument.

The chemical compositions of the zeolite samples were determined by ICP/OES (ThermoScientific iCAP 7000) analysis. In total, 50 mg of zeolite were mineralized in a mixture of 2 ml of HF, 4 ml of HNO₃, and 4 ml of HCl in a microwave oven. After cooling, the excess HF was eliminated by complexation with 15 ml of a saturated solution of H₃BO₃, treating the final mixture in a microwave oven. Then, the solutions under analysis were collected and diluted in ultrapure water to a total volume of 250 ml. The leached species in the liquid phases was checked by ICP-OES (Agilent Technologies, Santa Clara, CA, USA, 700 Series) after calibrating the instrument with standard solutions.

Nitrogen adsorption/desorption isotherms were measured on ASAP 2020 (Micromeritics) static volumetric apparatus at -196 °C. Before the sorption measurements, all the samples were degassed with a turbo molecular pump at 300 °C for 8 h. The *t*-plot method⁴¹ was applied to determine the volume of micropores (V_{micro}).

The nature and strength of acid sites in the germanosilicate zeolites were determined by FTIR spectroscopy of adsorbed pyridine (FTIR-Py). For this purpose, the zeolites were pressed into self-supporting wafers to a density of ~10 mg cm⁻² and *in situ* activated at $T = 200, 300$ or 450 °C and $p = 5 \times 10^{-5} \text{ Torr}$ for 4 h. In particular experiments, water calibrated aliquots were gradually introduced into the cell at 25 °C, followed by pyridine adsorption. Excess pyridine (Py) was adsorbed at 25 °C for 20 minutes, followed by 20 minute desorption at the same temperature. Thermodesorption of Py was performed at 25, 50, 75, 100, 120 and 150 °C for the germanosilicate zeolites and at 150, 250, 350, and 450 °C for the aluminosilicate zeolites for 20 min. FTIR spectra were recorded using a Nicolet iS50 spectrometer with a transmission MTC/B detector with a resolution of 4 cm⁻¹ by collecting 128 scans for a single spectrum at room temperature. The spectra were treated using Omnic 8.2 (Thermo Scientific) program. For baseline correction, the spectrum of the activated wafer was subtracted from the spectra collected after Py adsorption/



Scheme 1 Glycerol ketalization with acetone.

desorption. The concentrations of Brønsted acid sites in germanosilicate and reference aluminosilicate zeolites were evaluated from the integral intensity of the band at 1545 cm^{-1} using the absorption coefficient $\varepsilon = 1.7\text{ cm}^2\text{ mol}^{-1}$.⁴² The concentrations of Lewis acid sites in aluminosilicate zeolites were evaluated from the integral intensities of the bands at 1454 cm^{-1} using the absorption coefficient $\varepsilon(L) = 2.2\text{ cm}^2\text{ mol}^{-1}$,⁴² whereas the number of Lewis acid sites in germanosilicates was estimated based on the integral intensity of the band at 1611 cm^{-1} . To determine the area of the peak characteristic of coordinatively bonded (1611 cm^{-1}) and H-bonded (1596 cm^{-1}) Py, the resulting spectral curve was fitted using the Gaussian line shape. IR peak centers were fixed within $\pm 5\text{ cm}^{-1}$, and the full widths at half maxima were constrained between 5 cm^{-1} and 20 cm^{-1} .

The differential thermal and thermogravimetric analysis of the neat and spent catalysts was carried out using a TG-DTA analyser (Shimadzu Apparatus) on 4–6 mg samples in a nitrogen flow of 10 ml min^{-1} , at a heating rate of $10\text{ }^\circ\text{C min}^{-1}$ from room temperature to $600\text{ }^\circ\text{C}$, using an Al crucible and alumina as reference.

Catalytic tests

Before the catalytic tests, the germanosilicate zeolites were activated by heating to different temperatures (200 , 300 , and $450\text{ }^\circ\text{C}$) with a rate of $10\text{ }^\circ\text{C min}^{-1}$ and maintaining the selected temperature for 2 hours. Typically, 5 mg of the catalyst and 1 mmol glycerol, ethylene glycol or 1,4-butanediol were mixed with excess ketone (5 or 25 mmol). The catalytic tests were performed in glass vials with magnetic stirring at room temperature or $80\text{ }^\circ\text{C}$ for 3 hours. After the reaction time elapsed, the reaction mixture was cooled, and a small amount of ethanol (up to a total volume of 1 ml) was added to solubilize the untransformed glycerol that usually forms a separate phase. The mixture was then centrifuged, filtered and dried over sodium sulphate. In total, $200\text{ }\mu\text{l}$ of the final solution were slowly evaporated at $45\text{ }^\circ\text{C}$ overnight to remove the solvent. For recycling studies, after each catalytic cycle, the catalyst was immediately centrifuged, washed several times with ethanol and acetone, dried at $40\text{ }^\circ\text{C}$ and subjected to another catalytic run, thus avoiding a longer contact with moisture. To identify possible leaching of active species, the reaction mixture was removed after the 1 hour catalytic test then filtered, and the separated liquid was investigated under the same reaction conditions for another 2 or 12 hours.

Silylation of reaction products before the injection into a chromatographic column was required to increase their volatility and to derivatize the free hydroxyls of polyols. For this purpose, $150\text{ }\mu\text{L}$ of derivatization agent (1% w/w of trimethylchlorosilane in *N,O*-bis(trimethylsilyl)trifluoroacetamide) was mixed with $50\text{ }\mu\text{L}$ of pyridine as a catalyst. The derivatization occurred at $60\text{ }^\circ\text{C}$ for 30 min. The final products were analyzed by GC-MS (THERMO Electron Corporation, ISQ LT Single Quadrupole GC-MS system TRACE

1310, equipped with a TG-5SilMS column $30\text{ m} \times 0.25\text{ mm} \times 0.25\text{ }\mu\text{m}$) and NMR spectroscopy (Bruker Advance III UltraShield 500 MHz spectrometer, operating at 500.13 MHz for ^1H NMR, 125.77 MHz for ^{13}C NMR). For GC analysis, the injector was set up at $250\text{ }^\circ\text{C}$. The temperature in the oven was kept at $50\text{ }^\circ\text{C}$ for 1 min and then increased to $250\text{ }^\circ\text{C}$ at a rate of $7\text{ }^\circ\text{C min}^{-1}$.

Reference commercial aluminosilicate zeolites were used for comparison with the UTL and IWW germanosilicate catalysts. Commercial BEA zeolites with different Si/Al ratios included BEA-12.5 (Si/Al = 12.5, CP814E, purchased from Zeolyst), BEA-25 (Si/Al = 25, CP814Q, Zeolyst), and BEA-75 (Si/Al = 75, CZB-150 from Clariant). The commercial MOR zeolite was MOR-10 (Si/Al = 10, CBV-20A, Zeolyst).

Results and discussion

Physicochemical properties of germanosilicate zeolites

XRD patterns of both germanosilicate zeolites (Fig. 1A) correspond to those reported in the literature,^{6,7} confirming their phase purity. Both the IWW and UTL samples showed type I isotherms characteristic of microporous materials (Fig. 1B). The micropore volume of the medium-pore IWW was lower than that of the extra-large pore UTL zeolite ($0.11\text{ versus }0.21\text{ cm}^3\text{ g}^{-1}$, Table 2).

Fig. 2 depicts the SEM images of the IWW (A) and UTL (B) zeolites illustrating the important differences between the two samples. IWW possesses homogeneous $0.5 \times 0.5 \times 0.5\text{ }\mu\text{m}$ -sized rectangular crystals, whereas the UTL zeolite shows quite uniform thin rectangular $30 \times 25 \times 1\text{ }\mu\text{m}$ -sized crystals (Table 1).

In line with previously reported results, the FTIR spectra of both the IWW and UTL zeolites (Fig. 3A) display characteristic bands of silanol (3740 cm^{-1}) and germanol ($3660\text{--}3680\text{ cm}^{-1}$) groups.^{28,43–45} The remarkably more intensive band at *ca.* 3740 cm^{-1} in the spectrum of the IWW sample is consistent with its smaller crystal size/higher external surface (Tables 1 and 2) bearing terminal silanol groups. A weak and broad band apparent at $3600\text{--}3400\text{ cm}^{-1}$ in the spectra of the zeolites activated at 200 and $300\text{ }^\circ\text{C}$ is

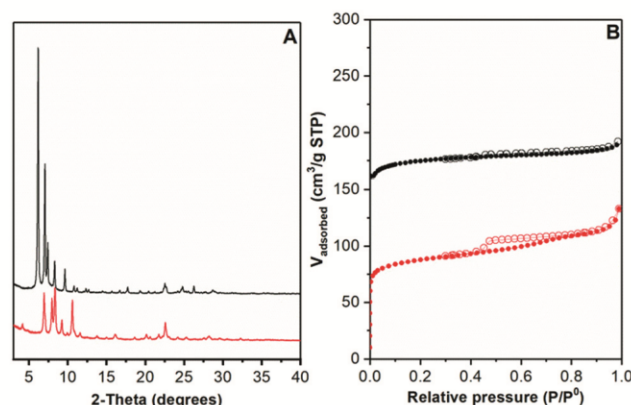


Fig. 1 XRD patterns (A) and nitrogen adsorption/desorption isotherms (B) of IWW (–) and UTL (–) zeolites.

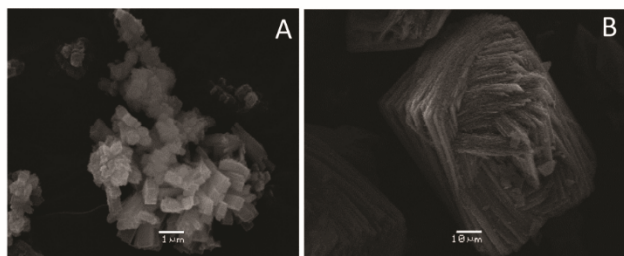


Fig. 2 SEM images of the IWW (A) and UTL (B) zeolites.

indicative of hydrogen-bonded OH groups attributed to adsorbed water.

The adsorption of pyridine on both the IWW and UTL zeolites gave rise to absorption bands (a.b.) characteristic of: 1) pyridine coordinatively bonded to Ge Lewis acid sites, **LAS-Py**, at $\nu_{8a} = 1611$ and $\nu_{19b} = 1452$ cm^{-1} ; 2) H-bonded pyridine, **H-Py**, at $\nu_{8a} = 1596$ and $\nu_{19b} = 1443$ cm^{-1} ; 3) physically adsorbed pyridine, **phys-Py**, at $\nu_{8b} = 1577$ and $\nu_{19b} = 1438$ cm^{-1} (Fig. 3B).^{46,47}

In agreement with ref. 46, the ν_{19b} absorption bands of **H-Py** and **LAS-Py** overlapped, while the respective ν_{8a} bands were well-resolved and thus used here for semi-quantitative estimation of Ge Lewis acid centers. Nevertheless, the determination of the molar absorption coefficient for the ν_{8a} band and hence quantification of LAS in both IWW and UTL was precluded by the unavoidable contribution of **H-Py**. The markedly higher intensity of the ν_{8a} -LAS band in UTL vs. IWW (Fig. 3B) suggested an enhanced number of Lewis acid sites in the former. Although ref. 27 reported that Brønsted acidity was characteristic of the UTL germanosilicate, no sign

Table 1 Chemical composition and crystal sizes of the germanosilicate zeolites

Sample	Chemical composition				Crystal size, μm
	mol%	mmol g^{-1}			
	Si	Ge	Ge	Si/Ge	
IWW	87.8	12.2	1.9	7.2	$0.5 \times 0.5 \times 0.5$
UTL	80.8	19.2	2.8	4.2	$30 \times 25 \times 1$

Table 2 Chemical composition and textural and acidic properties of the reference aluminosilicate zeolites

Sample	Si/Al	Concentration of acid sites, mmol g^{-1}			V_{micro} , $\text{cm}^3 \text{g}^{-1}$	S_{ext} , $\text{m}^2 \text{g}^{-1}$
		B	L	Σ		
BEA-12.5	12.5	0.31	0.32	0.63	0.16	220
BEA-25	25	0.33	0.19	0.52	0.25	210
BEA-75	75	0.05	0.07	0.12	0.20	220
MOR-10	10	0.56	0.35	0.91	0.14	70
IWW	—	0.16 ^a	n.d. ^d	n.d.	0.11	94
		0.07 ^b				
		0.05 ^c				
UTL	—	—	n.d. ^d	n.d.	0.21	40

^a $T_{\text{act}} = 200$ °C. ^b $T_{\text{act}} = 300$ °C. ^c $T_{\text{act}} = 450$ °C. ^d n.d. - not determined due to the restrictions of FTIR-Py.

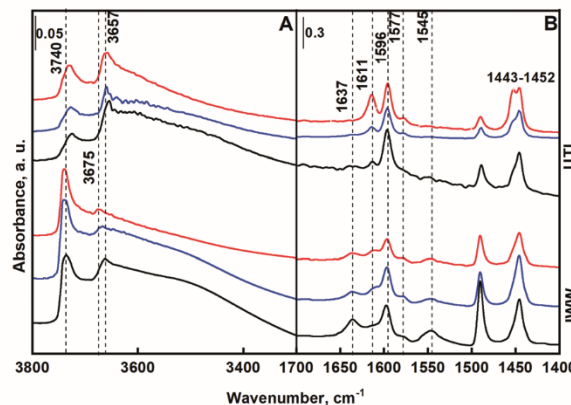


Fig. 3 FTIR spectra of the UTL and IWW zeolites after (A) activation at $T_{\text{act}} = 200$ (-), 300 (-), and 450 °C (-) and (B) adsorption/desorption of Py at $T = 25$ °C. Regions of OH- (A) and Py-ring (B) vibrations.

of Brønsted acid centers was detected in the UTL zeolite activated at different temperatures (Fig. 3B). In contrast to UTL, the FTIR-Py spectra of the IWW germanosilicate indicated the presence of the Brønsted acid centers (a.b. of **BAS-Py** at $\nu_{19b} = 1545$ cm^{-1} and $\nu_{8a} = 1637$ cm^{-1}). The evolution of the band at ca. 1545 cm^{-1} with the temperature of pyridine desorption (Fig. 4B) revealed that the Brønsted acid sites of the IWW germanosilicate are much weaker than those of aluminum-containing zeolites (Fig. 5A and ref. 28).

The concentration of the Brønsted acid sites in the IWW zeolite evaluated from the integral intensity of the band at 1545 cm^{-1} (Fig. 3B) decreases with the increase in activation temperature: 0.16 mmol g^{-1} ($T_{\text{act}} = 200$ °C), 0.07 mmol g^{-1} (300 °C) and 0.05 mmol g^{-1} (450 °C). The weakness of Ge-associated Brønsted acid sites and the variation of their concentration as a function of the activation conditions may be related to the water-induced nature of such acid centers. To validate this assumption, the IWW zeolite activated at $T = 450$ °C was subjected to dose-by-dose adsorption of water, followed by saturation with pyridine monitored using FTIR spectroscopy. The gradual adsorption of water resulted in the progressive diminishing a.b. of **LAS-Py** at $\nu_{8a} = 1611$ cm^{-1} with simultaneously growing intensity of the **BAS-Py** a.b. at $\nu_{19b} = 1545$ cm^{-1} (Fig. S2†).

Similarly, the water-induced formation of Brønsted acid sites in Sn-BEA and their reactivity were recently reported.⁴⁷ The decreasing a.b. of **LAS-Py** in the spectra of the IWW zeolite with decreasing activation temperature/increasing water loading accompanied by the increase in the intensity of the absorption band of **BAS-Py** (Fig. 3B and S2†) may suggest a similar mechanism of Lewis-to-Brønsted acid site conversion for Sn- and Ge-containing zeolites: adsorption of water on tetrahedrally coordinated Ge atoms (Lewis acid centers, $\equiv\text{Si}-\text{O}-\text{Ge}(\text{OSi})_3$) followed by the formation of bridging OH groups (Brønsted acid centers, $\equiv\text{Si}-(\text{OH})-\text{Ge}(\text{SiO})_3(\text{OH})(\text{H}_2\text{O})$). Conversely, the increase in activation temperature positively affected the number of Lewis acid sites in the UTL germanosilicate (~3 times higher integral intensity of $\nu_{8a} = 1611$ cm^{-1} for the zeolite activated at 450 vs. 200 °C, Fig. 4B).

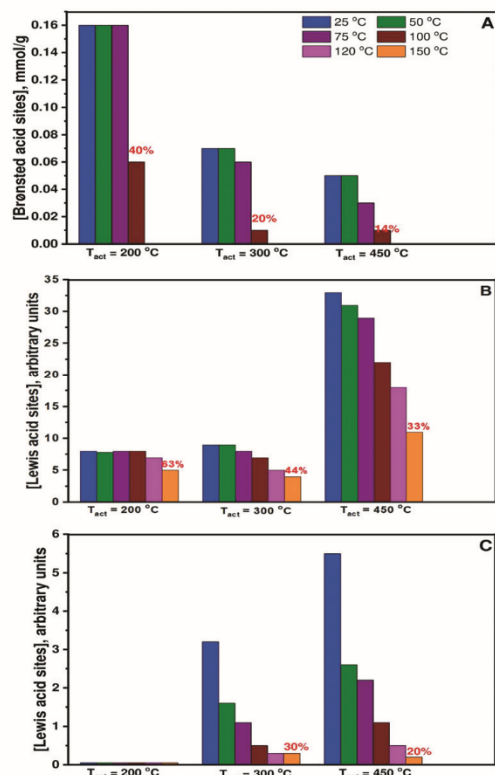


Fig. 4 Number of Brønsted acid sites in the IWW zeolite vs. T_{act} (A) and of Lewis acid sites in the UTL (B) and IWW (C) zeolites vs. T_{act} as determined from the desorption of pyridine at different temperatures. $x\%$ values correspond to the fraction of acid sites keeping the adsorbed pyridine after desorption at 100 °C (A) or 150 °C (B).

The result is in agreement with the lower hydrolytic stability of the UTL zeolite vs. the IWW zeolite previously reported in ref. 15 and 16.^{15,16} Thus, the

number of Lewis acid sites detected by FTIR-Py in UTL activated at 450 °C and lacking adsorbed water (Fig. 3A) reflects the number of four-coordinated Ge atoms accessible for pyridine molecules. In turn, the adsorbed water observed after UTL activation at 200–300 °C (Fig. 3A) is expected to hydrolyze the Ge–O–Si linkages decreasing the number of framework Ge atoms and hence detectable LAS.

Noticeably, the number of acid sites detected by FTIR-Py (Fig. 4) can hardly be correlated to the chemical composition of the germanosilicates under study (Table 1). The result can be explained, considering the (i) sterical limitations for probe molecule interaction with neighboring acid sites located in close proximity to each other – the situation which is characteristic of germanosilicate zeolites known for the preferential location of Ge atoms in *d4r* units of the framework;⁴⁸ (ii) low strength of Ge acid centers (*i.e.*, the shift of pyridine adsorption-desorption equilibrium to the desorption even at low temperature).

The XRD patterns of the reference commercial BEA and MOR zeolites highlight the lack of any crystalline admixtures (Fig. 5A), whereas the results of N_2 adsorption/desorption reveal reasonable values of micropore volumes characteristic of those materials (Table 2).

FTIR-Py showed the presence of both Brønsted and Lewis acid sites in the aluminosilicate zeolites. The total number of acid centers decreased with the increase in the Si/Al ratio (Table 2). Importantly, all the aluminosilicate zeolites had much stronger acid sites than the IWW and UTL germanosilicates (Fig. 5B shows the results of FTIR-Py for BEA-12.5 and MOR-10 to exemplify this general trend).

The crystal size of the BEA-12.5, BEA-25 and MOR-10 samples was comparable to that of the IWW germanosilicate, while BEA-75 showed bigger crystals (Fig. 6 and 2).

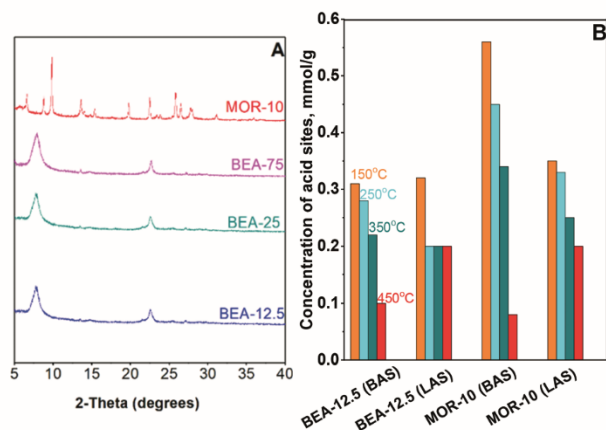


Fig. 5 XRD patterns (A) and concentrations of Brønsted (BAS) and Lewis (LAS) acid sites as determined from the desorption of pyridine at different temperatures (B) of the reference aluminosilicate zeolites. The samples were activated at $T = 450$ °C for 2 h.

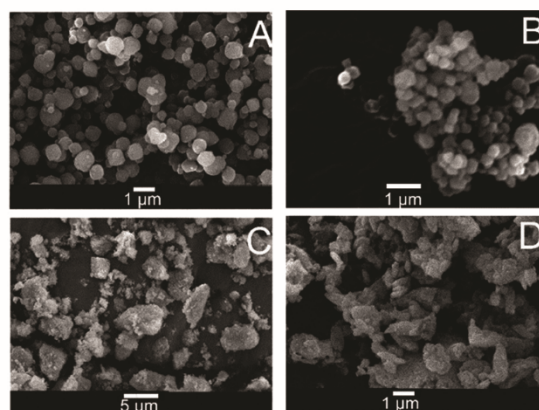


Fig. 6 SEM images of BEA-12.5 (A), BEA-25 (B), BEA-75 (C) and MOR-10 (D) zeolites.

Catalytic behavior of the germanosilicate zeolites in the ketalization of polyols

The main issue of the ketalization reaction is its low equilibrium constant and the need to remove the water produced in the reaction or to use excess ketone to shift the equilibrium to the product side. The research performed in this study used the second approach. Table 3 compiles comparative results assessed with the **IWW** and **UTL** germanosilicates for the ketalization of different polyols.

Depending on the nature of the reagent, the polyol conversion ranged from 7 to >99% at $T = 80\text{ }^{\circ}\text{C}$ after 3 h, whereas the selectivity was higher than 99% for both catalysts in the reactions with diols. When glycerol is used, a side-product 2,2-dimethyl-1,3-dioxan-5-ol can be formed and as a result, in this case, the selectivity varies between 96 and 99%. Increasing the ketone (*e.g.*, 2-butanone *vs.* acetone) or polyol(1,4-butanediol *vs.* glycerol *vs.* ethylene glycol) size decreased the conversion for both germanosilicates (Table 3 and S2†). The result may indicate diffusion limitations for reagents in the **IWW** and **UTL** germanosilicates; the trend was more pronounced for **UTL** featuring bigger crystals. Decreasing the reaction temperature to room temperature, as expected, decreased the conversion for both glycerol and



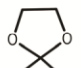
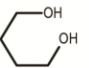

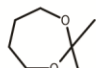
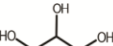

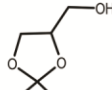


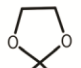
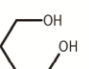

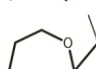
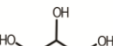

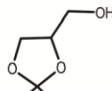
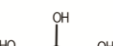

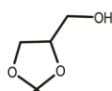


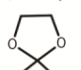
ethylene glycol ketalization with acetone (Table 3, entry 7 and 8). Even at room temperature, ketalization proceeded with satisfactory conversions (Table 3).

Table 4 compares the conversions of polyols achieved with the **IWW** and **UTL** germanosilicates activated at different temperatures and those of the commercial aluminosilicate zeolites.

The internal diffusion effect on the rate of glycerol ketalization cannot be ruled out for the **UTL** germanosilicate, which has the largest crystals (Fig. 2B) and the lowest glycerol conversion values (16–39%) *vs.* the **IWW** and commercial aluminosilicate **BEA** zeolites (Table 4). Conversely, the conversions of glycerol achieved over the **IWW** germanosilicate (40–50%) were comparable to those of commercial aluminosilicate **BEA** (45–48%) and exceeded the conversion over the **MOR** (14%) zeolite, which showed the highest concentration of strong acid sites, both Brønsted and Lewis (Table 2).

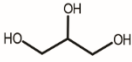

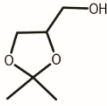
The crystallite size of the zeolites was earlier reported as one of the important factors for the glycerol conversion.⁴⁹ Smaller crystal sizes seem to improve the diffusion of reactants due to a short path. Accordingly, diffusion limitation generated in the mordenite (**MOR**) pores results in a lower glycerol conversion. According to the data presented in Tables 1–4, a correlation between the volume of the

Table 3 Catalytic performance of the **IWW** and **UTL** germanosilicates in the ketalization of polyols

Nr.	Polyol	Ketone	Main product	$T\text{ }^{\circ}\text{C}$	IWW		UTL	
					Conversion (%)	Selectivity (%)	Conversion (%)	Selectivity (%)
1				80	>99	>99	>99	>99
2				80	69	>99	59	99
3				80	63	97	56	>98
4				80	96	>99	98	>99
5				80	51	98	49	>99
6				80	19	96	7	98
7				25	56	98	27	97
8				25	89	>99	90	>99

Reaction conditions: 1 mmol polyol, 5 mmol ketone, 3 h, solvent-free, 5 mg catalyst. The catalysts were activated at 300 °C.

Table 4 Comparison of the catalytic performances of **IWW** and **UTL** activated at different temperatures with the commercial aluminosilicate zeolites

Nr.	Polyol	Ketone	Main product	Catalyst (activation temperature)	Conversion (%)	Selectivity (%)
1				UTL (450)	17	96
2				IWW (450)	41	96
3				UTL (300)	27	97
4				IWW (300)	56	98
5				UTL (200)	36	97
6				IWW (200)	46	98
7				BEA-12.5 (450)	53	98
8				BEA-25 (450)	57	96
11				BEA-75 (450)	49	96
12				MOR 10 (450)	15	95

Reaction conditions: 1 mmol polyol, 5 mmol ketone, 3 h, solvent-free, RT, 5 mg catalyst.

micropores, the surface area of the catalysts and conversion can be seen over the commercial zeolites, especially the **BEA** ones. The conversions (Table 4) over the commercial zeolites increase with the increase of the volume of the micropores and surface area. The surface area of the germanosilicate zeolites is lower than that of the commercial ones, while the yields are comparable or even higher than those over the commercial zeolites. The **UTL** catalyst has a higher surface area and larger crystals, but it has a smaller volume of micropores compared to **IWW**. Accordingly, the conversion generated over the **UTL** zeolite is comparable with that over **MOR**, which also possesses a smaller volume of micropores and larger crystals. However, the textural properties of catalysts only are not enough to explain the similar activity of the germanosilicate zeolites, which have a small surface area and weaker acid sites, with **BEA**. In this context, the acidic properties of the catalyst also play an important role and the collected results suggest that even the weak acid sites of the germanosilicate zeolites serve as active centers in the ketalization reaction. The conversion values of the commercial **BEA** zeolites (Table 4) cannot be correlated with the Si/Al ratio or with the overall concentration of acid sites only. However, to some extent, a correlation exists between the Brønsted acid sites and the conversion or B/L acid site ratio. Varying from 0.97 to 1.7 and 0.7 B/L ratio in the **BEA** zeolites lead to 53, 57 and 49% conversion, respectively. The results suggest that even the weak acid sites of the germanosilicate zeolites serve as active centers in the ketalization reaction. Consistently, with the increase in the number of Brønsted acid sites of the **IWW** zeolite and with the enhanced strength of the Lewis acid sites of **UTL** with the decrease in activation temperature (Fig. 4), the optimal temperature for **IWW** is 300 °C, whereas the optimal temperature for **UTL** is 200 °C. The decrease in the activity of the zeolite catalyst with the increase in the concentration of aluminum acid centers (Tables 2 and 4) is consistent with the high affinity of framework Al towards the water formed in the reaction (Scheme 1), which may compete with the reagents for the adsorption on active sites.⁵⁰ Indeed, hydrophobization of an Al-rich HY zeolite (CBV600, Si/Al ratio = 2.6) with an organosilane surfactant was recently reported to improve the efficiency of solvent-free glycerol-to-solketal conversion at

room temperature.⁵¹ In the case of MFI zeolites, increase of hydrophobicity leads also to a higher TOF.⁵² As a result, strong acidity in this type of biphasic reaction is not always an advantage. In contrast to Al, Ge incorporation into the frameworks of some silica zeolites decreased water uptake, thus allowing the preparation of weak solid acids characterized by moderate hydrophilicity.^{53,54} Moreover, water adsorption on the Ge Lewis sites of both germanosilicate zeolites may promote the *in situ* generation of Brønsted acid centers, which are more active in the ketalization of glycerol compared to the Lewis acid sites.⁵⁵

Conversion to solketal *vs.* time for the **BEA-25**, **IWW** and **UTL** catalysts is presented in Fig. 7. For the germanosilicate zeolites, the increase of the activity is more evident in the first two hours: for **IWW**, the conversion increases from around 30 to more than 50% in the first two hours leading after that to a slightly higher conversion than for **BEA-25**. The same trend is observed for **UTL** as well, although for smaller conversions. The commercial zeolite led to a 50% conversion in the first 15 minutes when it reaches a plateau. The single phase formed after 15 minutes of reaction (Fig. 7, right). Taking into consideration the difference existing between the textural properties, Si/Ge ratio and acidity of the **IWW** and **UTL** catalysts, a similar time needed to achieve the highest

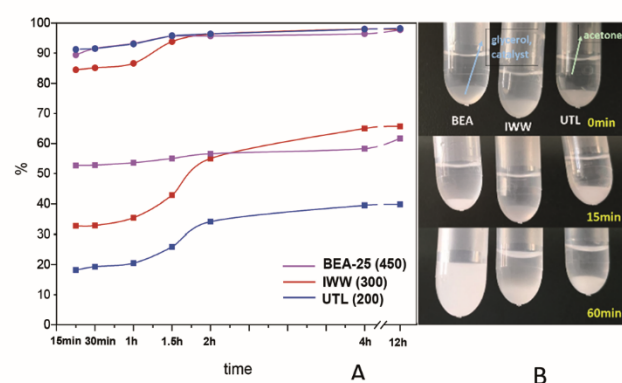


Fig. 7 (A) Time-on-stream dependence of glycerol conversion (square) and solketal selectivity (circle) over the zeolite catalysts. (B) Appearance of the reaction mixtures after 15 and 60 minutes of reaction; (B) reaction conditions: 1 mmol glycerol, 5 mmol acetone, solvent-free, RT, 5 mg catalyst.

conversion suggests that some induced species are responsible for the increase of catalytic activity and the formation of those species is a time-factor. The concentration of Brønsted acid sites per surface unit is slightly higher in the **IWW** zeolite, compared to BEA-25. However, the faster plateau reached in the presence of the **BEA** catalyst should be assumed to a larger surface area.

However, all the catalysts provided similar selectivities after 2 h of reaction. The secondary product, acetal (2,2-dimethyl-1,3-dioxan-5-ol), is formed over the **IWW** catalyst during the first hour, then subsequently glycerol is converted into solketal only.

Noticeably, when increasing the ketone-to-alcohol molar ratio to 25, the solketal yield reached 99% over the **IWW** catalyst, even at room temperature (Fig. 8). In addition, no side products, such as dioxane (2,2-dimethyl-1,3-dioxan-5-ol), or acetone condensation products (mesityl oxide) were identified when using **IWW** and **UTL** or even the commercial zeolites under these conditions. This high selectivity is usually explained by a mechanism involving the rearrangement of dioxane to dioxalane, which is catalyzed by Brønsted acid sites and favored by an increase in pore volume and by a decrease in acidity. The literature on selectivity is, however, contradictory, increasing in some cases by dealumination⁵⁶ or desilication.²⁹

Framework germanium atoms are able to not only change the local environment (reflected in the transformation of Lewis-to-Brønsted acid sites) but also leach to the liquid phase by coordination with water, as by-products of the ketalization reaction. The results from the recycling test showed that both the **UTL** and **IWW** catalysts can be reused at least 3 times without selectivity and conversion losses, when the 1:5 glycerol:acetone molar ratio is used (Fig. 9). The type of acid sites and hydrolysis reaction are the two factors mostly affecting the selectivity to solketal.⁵⁶ During the recycling, the selectivity increases slightly for the **UTL** and **BEA** catalysts. The enhancement can be explained by the adsorption of some water on the Brønsted acid sites during the catalyst recycling that can favour the rearrangement to solketal.⁵²

The commercial zeolite BEA-25 was also recycled 3 times without considerable changes in terms of conversion or selectivity. However, after the second recycling of BEA-25, it was noticed that the catalyst colour changed to yellow, which still persists after the catalyst washing. The differential thermal and thermogravimetric analysis of the fresh and spent BEA-25 and **IWW** catalysts is shown in Fig. 10.

After 3 catalytic cycles, the weight loss of the **IWW** catalyst is around 3% and for BEA-25, it is around 5% indicating

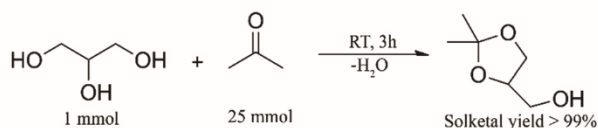


Fig. 8 Ketalization of acetone to ketal. Reaction conditions: 5 mg catalyst **IWW**, RT, 3 h magnetic stirring, solvent-free.

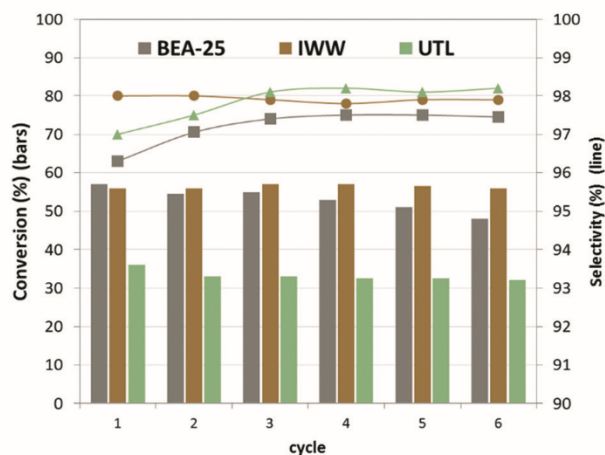


Fig. 9 Catalyst recycling results for solketal synthesis (reaction conditions: 1 mmol polyol, 5 mmol ketone, 3 h, solvent-free, RT, 5 mg catalyst).

larger deposits of coke. Also, for BEA-25, a new DTA peak occurs at temperatures between 120 and 130 °C related to these deposits. A higher deactivation of the **UTL** and **IWW** catalysts was also observed during recycling, when a higher

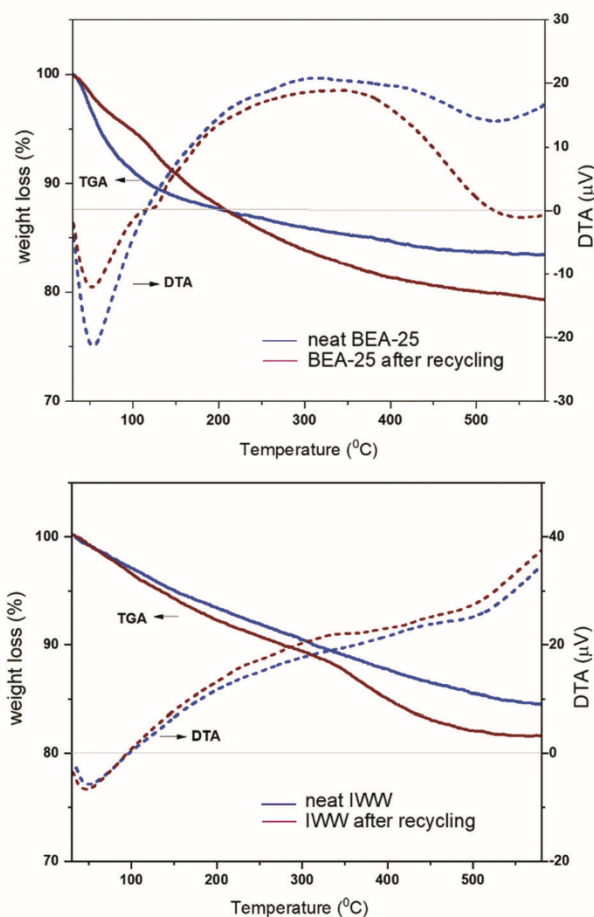


Fig. 10 The differential thermal and thermogravimetric analysis of the fresh and spent BEA-25 and **IWW** catalysts (reaction conditions: 1 mmol glycerol, 5 mmol acetone, solvent-free, RT, 5 mg catalyst, 3 cycles).

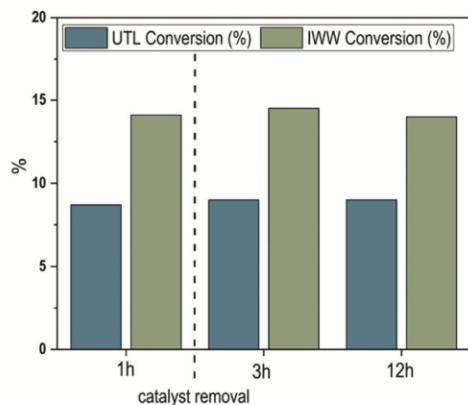


Fig. 11 Results of leaching tests over the IWW and UTL catalysts (reaction conditions: 1 mmol glycerol, 5 mmol acetone, solvent-free, RT, 5 mg catalyst. The catalysts were activated at 300 °C).

amount of acetone was used (reaction conditions from Fig. 8). However, even for ultrastable Y zeolites, washing and drying did not prevent the decrease in catalytic activity.³¹

Leached Ge species in solution after 1 h were under 0.1 ppm as determined by ICP-OES. Nevertheless, the leached Ge species were not active during the ketalization reactions, as demonstrated for glycerol (Fig. 11), with only a negligible increase in the conversion after removing the catalyst, even after 12 hours of reaction.

The comparison of the performance of the germanosilicate zeolites in ketalization reactions with the results reported in the literature shows that similar conversion/selectivity values were documented for glycerol ketalization with acetone when using other homogeneous or more complex heterogeneous catalysts, such as Lu(OTf)₃,⁵⁷ MoPO/SBA-15SiO₂,⁵⁸ Re/SiO₂,⁵⁹ and ZrO₂/SO₄ (ref. 60) or MOR,³⁰ MFI, hydrophobic HY⁵¹ or BEA zeolites,^{30,49,56} which provided similar performances, sometimes even at higher temperatures.⁶¹

Conclusions

Weak acidic germanosilicate zeolites IWW and UTL are active and selective catalysts of polyol (e.g., ethylene glycol, glycerol, 1,4 butyldiol) ketalization. Ketalization reactions with germanosilicate catalysts resulted in the exclusive formation of the target dioxolane products. The less active UTL catalyst presented a higher Ge content and a larger crystal size and volume of micropores than IWW. Based on FTIR spectroscopy of pyridine, the UTL zeolite exclusively has Lewis acidity, whereas the IWW catalyst was prone to water-induced formation of weak Brønsted acid sites. Increasing the activation temperature (200–450 °C) reduced the concentration of Brønsted acid centers in the IWW germanosilicate (i.e., 0.16; 0.07 and 0.05 mmol g⁻¹ for T_{act} = 200, 300 and 450 °C, respectively) but increased the number of Lewis acid sites in both zeolites. The IWW catalyst (40–50% solketal yield at T_{act} = 450–300 °C) outperformed not only the Lewis acidic UTL germanosilicate (16–36%, T_{act} = 450–200 °C) but also the commercial aluminosilicate zeolites MOR (15%, Si/Al = 10) and

BEA (45–48%, Si/Al = 12.5–75) with strong Brønsted and Lewis acid sites. Increasing the acetone-to-glycerol molar ratio to 25 led to a yield of >99% of the solketal product over the IWW catalyst, even at room temperature. The IWW catalyst was recycled 3 times without any conversion and selectivity losses. The IWW catalyst activity for solketal formation in terms of conversion, selectivity and recyclability is at least comparable with the commercial BEA-25 zeolite. Thus, the results of the present study demonstrate the catalytic potential of unmodified germanosilicate zeolites, thereby encouraging further research on the catalytic behavior of these materials, particularly on their stability and deactivation and regeneration modes.

Conflicts of interest

There are no conflicts to declare.

Acknowledgements

I. P. and V. P. acknowledge the support from the Government of Romania, Ministry of Research and Innovation, project PN-III-P1-1.1-PD-2016-1054 Nr. 29/2018. M. S. and J. Č. acknowledge the OP VVV “Excellent Research Teams” project No. CZ.02.1.01/0.0/0.0/15_003/0000417– CUCAM. J. Č. acknowledge the support from the Czech Science Foundation project EXPRO (19-27551X). M. S. gratefully acknowledges the financial support from the Czech Science Foundation project 20-12099S. J. Z. acknowledges the support from the Grant Agency of Charles University project 1398119 and the Czech Science Foundation project 19-21534S.

Notes and references

- 1 P. Eliášová, M. Opanasenko, P. S. Wheatley, M. Shamzhy, M. Mazur, P. Nachtigall, W. J. Roth, R. E. Morris and J. Čejka, *Chem. Soc. Rev.*, 2015, **44**, 7177–7206.
- 2 J. Li, A. Corma and J. Yu, *Chem. Soc. Rev.*, 2015, **44**, 7112–7127.
- 3 A. Corma, M. T. Navarro, F. Rey, J. Rius and S. Valencia, *Angew. Chem., Int. Ed.*, 2001, **40**, 2277–2280.
- 4 D. L. Dorset, K. G. Strohmaier, C. E. Kliever, A. Corma, M. J. Díaz-Cabañas, F. Rey and C. J. Gilmore, *Chem. Mater.*, 2008, **20**, 5325–5331.
- 5 J. Sun, C. Bonneau, Á. Cantín, A. Corma, M. J. Díaz-Cabañas, M. Moliner, D. Zhang, M. Li and X. Zou, *Nature*, 2009, **458**, 1154–1157.
- 6 J.-L. Paillaud, B. Harbuzaru, J. Patarin and N. Bats, *Science*, 2004, **304**, 990–992.
- 7 A. Corma, M. J. Díaz-Cabañas, F. Rey, S. Nicolopoulos and K. Boulahya, *Chem. Commun.*, 2004, 1356–1357, DOI: 10.1039/B406572G.
- 8 N. Žilková, M. Shamzhy, O. Shvets and J. Čejka, *Catal. Today*, 2013, **204**, 22–29.
- 9 M. Shamzhy, M. Opanasenko, P. Concepción and A. Martínez, *Chem. Soc. Rev.*, 2019, **48**, 1095–1149.
- 10 W. J. Roth, O. V. Shvets, M. Shamzhy, P. Chlubná, M. Kubů, P. Nachtigall and J. Čejka, *J. Am. Chem. Soc.*, 2011, **133**, 6130–6133.

- 11 M. Mazur, P. S. Wheatley, M. Navarro, W. J. Roth, M. Položij, A. Mayoral, P. Eliášová, P. Nachtigall, J. Čejka and R. E. Morris, *Nat. Chem.*, 2016, **8**, 58–62.
- 12 Y. Zhou, S. A. Kadam, M. Shamzhy, J. Čejka and M. Opanasenko, *ACS Catal.*, 2019, **9**, 5136–5146.
- 13 V. Kasneryk, M. Shamzhy, M. Opanasenko, P. S. Wheatley, S. A. Morris, S. E. Russell, A. Mayoral, M. Trachta, J. Čejka and R. E. Morris, *Angew. Chem., Int. Ed.*, 2017, **56**, 4324–4327.
- 14 V. Kasneryk, M. Shamzhy, M. Opanasenko, P. S. Wheatley, R. E. Morris and J. Čejka, *Dalton Trans.*, 2018, **47**, 3084–3092.
- 15 P. Chlubná-Eliášová, Y. Tian, A. B. Pinar, M. Kubů, J. Čejka and R. E. Morris, *Angew. Chem., Int. Ed.*, 2014, **53**, 7048–7052.
- 16 V. Kasneryk, M. Shamzhy, J. Zhou, Q. Yue, M. Mazur, A. Mayoral, Z. Luo, R. E. Morris, J. Čejka and M. Opanasenko, *Nat. Commun.*, 2019, **10**, 5129.
- 17 D. S. Firth, S. A. Morris, P. S. Wheatley, S. E. Russell, A. M. Z. Slawin, D. M. Dawson, A. Mayoral, M. Opanasenko, M. Položij, J. Čejka, P. Nachtigall and R. E. Morris, *Chem. Mater.*, 2017, **29**, 5605–5611.
- 18 F. Gao, M. Jaber, K. Bozhilov, A. Vicente, C. Fernandez and V. Valtchev, *J. Am. Chem. Soc.*, 2009, **131**, 16580–16586.
- 19 M. V. Shamzhy, P. Eliášová, D. Vitvarová, M. V. Opanasenko, D. S. Firth and R. E. Morris, *Chem. – Eur. J.*, 2016, **22**, 17377–17386.
- 20 M. El-Roz, L. Lakiss, A. Vicente, K. N. Bozhilov, F. Thibault-Starzyk and V. Valtchev, *Chem. Sci.*, 2014, **5**, 68–80.
- 21 P. A. Kots, V. L. Sushkevich, O. A. Tyablikov and I. I. Ivanova, *Microporous Mesoporous Mater.*, 2017, **243**, 186–192.
- 22 X. Liu, H. Xu, L. Zhang, L. Han, J. Jiang, P. Oleynikov, L. Chen and P. Wu, *ACS Catal.*, 2016, **6**, 8420–8431.
- 23 X. Liu, L. Zhang, H. Xu, J. Jiang, M. Peng and P. Wu, *Appl. Catal., A*, 2018, **550**, 11–19.
- 24 J. I. N. Zhang, Q. Yue, M. Mazur, M. Opanasenko, M. V. Shamzhy and J. Čejka, *ACS Sustainable Chem. Eng.*, 2020, **8**, 8235–8246.
- 25 V. I. Kasneryk, M. V. Shamzhy, M. V. Opanasenko and J. Čejka, *J. Energy Chem.*, 2016, **25**, 318–326.
- 26 X. Liu, W. Mao, J. Jiang, X. Lu, M. Peng, H. Xu, L. Han, S.-A. Che and P. Wu, *Chem. – Eur. J.*, 2019, **25**, 4520–4529.
- 27 N. Kasian, G. Vanbutsele, K. Houthoofd, T. I. Koranyi, J. A. Martens and C. E. A. Kirschhock, *Catal. Sci. Technol.*, 2011, **1**, 246–254.
- 28 M. Shamzhy, O. V. Shvets, M. V. Opanasenko, D. Procházková, P. Nachtigall and J. Čejka, *Adv. Porous Mater.*, 2013, **1**, 103–113.
- 29 J. Kowalska-Kuś, A. Held and K. Nowińska, *ChemCatChem*, 2020, **12**, 510–519.
- 30 J. Kowalska-Kuś, A. Held, M. Frankowski and K. Nowińska, *J. Mol. Catal. A: Chem.*, 2017, **426**, 205–212.
- 31 L. Li, T. I. Korányi, B. F. Sels and P. P. Pescarmona, *Green Chem.*, 2012, **14**, 1611–1619.
- 32 C. J. A. Mota, C. X. A. da Silva, N. Rosenbach, J. Costa and F. da Silva, *Energy Fuels*, 2010, **24**, 2733–2736.
- 33 S. S. Poly, M. A. R. Jamil, A. S. Touchy, S. Yasumura, S. M. A. H. Siddiki, T. Toyao, Z. Maeno and K.-i. Shimizu, *Mol. Catal.*, 2019, **479**, 110608.
- 34 P. Ferreira, I. M. Fonseca, A. M. Ramos, J. Vital and J. E. Castanheiro, *Appl. Catal., B*, 2010, **98**, 94–99.
- 35 N. Narkhede and A. Patel, *RSC Adv.*, 2014, **4**, 19294–19301.
- 36 M. J. da Silva, A. A. Julio and F. C. S. Dorigetto, *RSC Adv.*, 2015, **5**, 44499–44506.
- 37 M. N. Timofeeva, V. N. Panchenko, N. A. Khan, Z. Hasan, I. P. Prosvirin, S. V. Tsybulya and S. H. Jung, *Appl. Catal., A*, 2017, **529**, 167–174.
- 38 A. Corma, F. Rey, S. Valencia, J. L. Jorda and J. Rius, *Nat. Mater.*, 2003, **2**, 493–497.
- 39 O. V. Shvets, M. V. Shamzhy, P. S. Yaremov, Z. Musilová, D. Procházková and J. Čejka, *Chem. Mater.*, 2011, **23**, 2573–2585.
- 40 M. V. Shamzhy, O. V. Shvets, M. V. Opanasenko, P. S. Yaremov, L. G. Sarkisyan, P. Chlubná, A. Zúkal, V. R. Marthala, M. Hartmann and J. Čejka, *J. Mater. Chem.*, 2012, **22**, 15793–15803.
- 41 B. C. Lippens and J. H. de Boer, *J. Catal.*, 1965, **4**, 319–323.
- 42 C. A. Emeis, *J. Catal.*, 1993, **141**, 347–354.
- 43 M. Moliner, M. J. Díaz-Cabañas, V. Fornés, C. Martínez and A. Corma, *J. Catal.*, 2008, **254**, 101–109.
- 44 H. Kosslick, V. A. Tuan, R. Fricke, C. Peuker, W. Pilz and W. Storek, *J. Phys. Chem.*, 1993, **97**, 5678–5684.
- 45 M. V. Shamzhy, C. Ochoa-Hernández, V. I. Kasneryk, M. V. Opanasenko and M. Mazur, *Catal. Today*, 2016, **277**, 37–47.
- 46 M. Shamzhy, J. Přeč, J. Zhang, V. Ruau, H. El-Siblani and S. Mintova, *Catal. Today*, 2020, **345**, 80–87.
- 47 V. L. Sushkevich, P. A. Kots, Y. G. Kolyagin, A. V. Yakimov, A. V. Marikutsa and I. I. Ivanova, *J. Phys. Chem. C*, 2019, **123**, 5540–5548.
- 48 M. Opanasenko, M. Shamzhy, Y. Wang, W. Yan, P. Nachtigall and J. Čejka, *Angew. Chem., Int. Ed.*, 2020, **59**, 19380–19389.
- 49 P. Manjunathan, S. P. Maradur, A. B. Halgeri and G. V. Shanbhag, *J. Mol. Catal. A: Chem.*, 2015, **396**, 47–54.
- 50 G. Li, B. Wang and D. E. Resasco, *ACS Catal.*, 2020, **10**, 1294–1309.
- 51 M. S. Rahaman, T. K. Phung, M. A. Hossain, E. Chowdhury, S. Tulaphol, S. B. Lavani, M. O'Toole, G. A. Willing, J. B. Jasinski, M. Crocker and N. Sathitsuksanoh, *Appl. Catal., A*, 2020, **592**, 117369.
- 52 G. L. Catuzo, C. V. Santilli and L. Martins, *Catal. Today*, 2020, DOI: 10.1016/j.cattod.2020.07.008.
- 53 S. Li, V. A. Tuan, R. D. Noble and J. L. Falconer, *Ind. Eng. Chem. Res.*, 2001, **40**, 6165–6171.
- 54 C. H. Nicolas and M. Pera-Titus, *Microporous Mesoporous Mater.*, 2012, **153**, 254–262.
- 55 K. Stawicka, A. E. Díaz-Álvarez, V. Calvino-Casilda, M. Trejda, M. A. Bañares and M. Ziolek, *J. Phys. Chem. C*, 2016, **120**, 16699–16711.
- 56 N. J. Venkatesha, Y. S. Bhat and B. S. Jai Prakash, *RSC Adv.*, 2016, **6**, 18824–18833.
- 57 A. W. Pierpont, E. R. Batista, R. L. Martin, W. Chen, J. K. Kim, C. B. Hoyt, J. C. Gordon, R. Michalczyk, L. A. P. Silks and R. Wu, *ACS Catal.*, 2015, **5**, 1013–1019.

- 58 S. Gadamsetti, N. P. Rajan, G. S. Rao and K. V. R. Chary, *J. Mol. Catal. A: Chem.*, 2015, **410**, 49–57.
- 59 M. Kapkowski, W. Ambrożkiewicz, T. Siudyga, R. Sitko, J. Szade, J. Klimontko, K. Balin, J. Lełątko and J. Polanski, *Appl. Catal., B*, 2017, **202**, 335–345.
- 60 P. S. Reddy, P. Sudarsanam, B. Mallesham, G. Raju and B. M. Reddy, *J. Ind. Eng. Chem.*, 2011, **17**, 377–381.
- 61 C. X. A. da Silva, V. L. C. Gonçalves and C. J. A. Mota, *Green Chem.*, 2009, **11**, 38–41.



Quantification of Lewis acid sites in 3D and 2D TS-1 zeolites: FTIR spectroscopic study

Mariya Shamzhy^{a,*}, Jan Přeč^{a,b}, Jin Zhang^a, Valérie Ruaux^b, Hussein El-Siblani^b, Svetlana Mintova^b

^a Department of Physical and Macromolecular Chemistry, Faculty of Science, Charles University, Hlavova 2030/8, 128 43 Prague 2, Czech Republic

^b Normandie Université, ENSICAEN, UNICAEN, CNRS, Laboratoire Catalyse et Spectrochimie, 14000 Caen France



ARTICLE INFO

Keywords:

TS-1
Layered zeolites
Acidity
FTIR
Molar extinction coefficient

ABSTRACT

Titanium silicalite 1 (TS-1) zeolite is an important selective oxidation catalyst. Recently prepared layered and pillared forms expanded the application of TS-1 to the catalytic oxidation of bulky molecules. Despite progress in designing and application of titanosilicate zeolites in catalysis, only qualitative information of their acidity is available. Herein, we report thorough characterization of acid sites in TS-1 zeolites of different morphologies (3D TS-1, layered 2D TS-1, 2D TS-1 pillared either with silica (TS-1-PiSi) or silica-titania (TS-1-PITi)) using FTIR spectroscopy and probe molecules. FTIR of adsorbed pyridine was used for quantification of Ti-associated Lewis acid sites based on the integral intensity of ν_{8a} absorption band ca. 1608 cm^{-1} and measured integrated molar extinction coefficient ($\epsilon_{1608}(\text{Ti-LAS}) = 0.71 \pm 0.01\text{ cm}^2\text{ }\mu\text{mol}^{-1}$). Thermodesorption of pyridine monitored with FTIR showed that distribution of strength of Lewis acid sites is, to some extent, dependent on the way of Ti incorporation in the samples. TS-1-PITi, containing large fraction of external surface $\text{Ti}(\text{OH})(\text{OSi})_3$ species introduced post-synthesis, showed increased concentration of stronger Lewis acid centres. FTIR spectroscopy of TS-1 with pre-adsorbed quinoline and d_3 -acetonitrile probe confirmed enhanced relative concentration of external Lewis acid sites in all layered TS-1 materials (28–38%) vs. 3D TS-1 (2%).

1. Introduction

Titanosilicate zeolites are well established selective oxidation catalysts with the ability to activate aqueous hydrogen peroxide. Titanosilicate zeolites, particularly titanium silicalite 1 (TS-1, MFI topology [1,2]) are used industrially in propylene epoxidation, phenol hydroxylation, and cyclohexanone ammoxidation [3,4]. In addition, they catalyse epoxidation of C=C double bonds in general (e.g. in linear and cyclic olefins or terpenes), oxidation of alkanes to corresponding alcohols, oxidation of alcohols to ketones and organic sulfides to sulfoxides and sulfones [5,6].

Titanosilicate zeolites have titanium atoms isomorphously incorporated in the framework. These four-coordinated Ti atoms act like weak Lewis acid sites, coordinating hydrogen peroxide. Until today, about 17 type zeolites have been prepared in the titanosilicate form, either by direct hydrothermal synthesis or by post-synthesis modification. These include the TS-1 (MFI), Ti-beta (*BEA) [7], Ti-MWW [8], Ti-MOR [9], Ti-MSE [10], Ti-CON [11] and others. Also, various hierarchical and layered forms, particularly derived from TS-1, Ti-MWW [12] and Ti-UTL [13] were prepared. The main reason to develop the

hierarchical and layered titanosilicates is to reduce diffusion limitations for sterically demanding substrates in conventional zeolites [14]. Sterically demanding substrates such as cyclic olefins and terpenes cannot access the narrow micropores of medium-pore zeolites (e.g. MFI $d_p = 5.5\text{ \AA}$), and improvement provided by use of large-pore zeolite (e.g. Ti-beta) is not always sufficient.

Layered titanosilicates are obtained when a corresponding zeolite is formed via a layered precursor (e.g. Ti-MWW [8], Ti-FER [15]) or they can be prepared using the surfactant templated synthesis (layered TS-1 [16]) or using the ADOR protocol (Ti-UTL derived materials [13]). Properties of layered titanosilicates can be tuned by post-synthesis transformations, particularly by varying the interlayer distance and/or introducing new species between the layers [17]. One of such transformations is pillaring of a swollen layered titanosilicate (in a swollen material, the interlayer distance is expanded by introducing a surfactant in between the layers).

In a pillared material the layers are supported by amorphous silica pillars and thus they do not collapse upon calcination [12]. Recently, we have demonstrated that by introducing additional titanium source at pillaring step, highly active catalysts for epoxidation of cyclic olefins

* Corresponding author.

E-mail address: mariya.shamzhy@natur.cuni.cz (M. Shamzhy).

<https://doi.org/10.1016/j.cattod.2019.10.011>

Received 23 July 2019; Received in revised form 27 September 2019; Accepted 7 October 2019

Available online 14 October 2019

0920-5861/ © 2019 Elsevier B.V. All rights reserved.

and terpenes are formed [13,18].

Comparing the catalysis data in literature [19] and our experimental results [13,18,20], it can be observed that the decrease in diffusion limitations improves the catalytic activity of nanosheet vs. conventional 3D titanasilicate zeolites. However, despite a big progress in designing and applying titanasilicate zeolites in catalysis, only qualitative information on the acidity is available mainly for 3D TS-1. The results of UV-vis, FTIR and XANES spectroscopies of adsorbed probe molecules have revealed the presence of coordinatively unsaturated Ti-sites acting as Lewis acid centres in TS-1 [21–24]. In particular, Bonino et al. reported evidence for the Lewis acid character of the tetrahedral Ti sites in TS-1 based on the FTIR spectroscopy using adsorbed d_3 -acetonitrile and pyridine as complementary probe molecules. FTIR spectra of pyridine adsorbed on dehydrated TS-1 [21,22], Ti-beta [21] and Ti-MWW [25] zeolites have also indicated the presence of only Lewis acid sites. Although the nature of acid centers was unambiguously addressed for different 3D titanasilicate zeolites, to the best of our knowledge, (i) quantification of Lewis acid sites as well as (ii) estimation of acid sites distribution with respect to their strength, both influencing the catalytic behaviour of titanasilicate zeolites, have not been explored so far either for 3D or 2D TS-1 catalysts.

Besides providing valuable qualitative information on the surface chemical properties of zeolites, FTIR spectroscopy is also a powerful tool for quantitative characterization of the nature, strength and location of their active sites [26,27].

D_3 -acetonitrile (proton affinity (PA) = 783 kJ/mol), pyridine (PA = 912 kJ/mol) and alkyl-pyridines are the most frequently used molecules to probe the acidity of aluminosilicates [27]. The FTIR spectroscopy of adsorbed pyridine is usually applied for identifying the nature and quantifying the amount of acid sites in medium- and large-pore zeolites using absorption bands characteristic of pyridine adsorbed on Al-associated Brønsted (1545 cm^{-1}) and Lewis acid centres (1450 cm^{-1}) [28,29]. Temperature-programmed desorption of pyridine [30,31] and alkylpyridines are widely used to assess the strength of acid sites located either in zeolite micropores or on the external surface.

In contrast, ammonia and d_3 -acetonitrile- are more suitable probe molecules for the quantitative analysis of acid centres in small-pore zeolites, while substituted nitriles (e.g., propionitrile, 2,2-dimethylpropionitrile, isobutyronitrile and others) have been used for the quantification of the accessibility of acid sites in zeolites [32–35].

Being well established particularly for aluminosilicate catalysts, FTIR spectroscopy has been so far undeservedly underused for titanosilicates.

Herein, we report the results of detailed characterization of acid sites in titanosilicate MFI zeolites of different structures and morphologies (3D TS-1, lamellar 2D TS-1, 2D TS-1 pillared either with silica TS-1-PiSi or silica-titania TS-1-PiTi) using FTIR spectroscopy of adsorbed probe molecules. FTIR of adsorbed pyridine (kinetic diameter of 5.4 Å) characterized by relatively high basic strength was used for quantification of Ti-associated Lewis acid sites. For that, we used ν_{8a} absorption band ca 1608 cm^{-1} and determined corresponding molar extinction coefficient. The quantification of weak Lewis acid sites in TS-1 zeolites using ν_{19b} absorption band ca 1445 cm^{-1} was impeded by unavoidable contribution of H-bonded pyridine to the intensity of ν_{19b} band. A combination of pyridine-FTIR with thermal desorption provided an estimate of the acid strength distribution in titanosilicate zeolites under the study. Moreover, an accessibility of Lewis acid sites in 3D and 2D TS-1 catalysts was addressed by selective poisoning of external sites with quinoline (QUI, kinetic diameter 6.2 Å) and subsequent quantification of the internal sites using FTIR of adsorbed d_3 -acetonitrile (ACN, kinetic diameter 4.0 Å).

2. Experimental

2.1. Catalysts preparation

3D TS-1(a) catalyst was a commercial TS-1 provided by Zeolyst International. 3D TS-1(b) catalyst was synthesized from a gel with an initial molar composition 100 TEOS : 2.32 Ti(OBu)₄ : 35 TPA–OH : 4000 H₂O following a procedure from ref [36]. TEOS stands for tetraethyl orthosilicate; Ti(OBu)₄ stands for titanium(IV) butoxide; TPA–OH stands for tetrapropylammonium hydroxide which acted as a structure directing agent.

2D TS-1 was prepared following a restricted crystal growth protocol developed by Na et al. [16] and more specifically following the protocol reported in Ref. [18]. In short: a bromide-free surfactant template C₁₈H₃₇N⁺(CH₃)₂-C₆H₁₂N⁺(CH₃)₂-C₆H₁₃ in a hydroxide form (C₁₈₋₆₋₆OH₂) was used for the preparation of a synthesis mixture with a molar composition 100 TEOS : 2.5 Ti(OBu)₄ : 6 C₁₈₋₆₋₆OH₂ : 5000 H₂O. The zeolite was hydrothermally synthesized in a Teflon-lined autoclave at 155 °C for 236 h under agitation. Final product was collected by filtration, washed with distilled water, dried and part of it was calcined at 550 °C for 8 h with a temperature ramp of 2 °C. The remaining part was divided into two and was subjected to silica (yielding TS-1-PiSi) or silica-titania pillaring (yielding TS-1-PiTi).

Both TS-1-PiSi and TS-1-PiTi were prepared following the procedures reported by our group earlier [18]. In short, the as-synthesized 2D TS-1 was pillared using a TEOS (20 ml/g of zeolite) in case of TS-1-PiSi and using a mixture of TEOS and TBOTi in mass ratio 30:1 in case of TS-1-PiTi. The zeolite was mixed with the pillaring medium and stirred at 65 °C for 24 h. After the given time, the product was centrifuged, dried, hydrolyzed in water with 5% of ethanol for another 48 h and finally filtered, dried and calcined at 550 °C for 8 h with a temperature ramp of 2 °C.

2.2. Catalysts basic characterization

The structure and crystallinity of all materials was determined by X-ray powder diffraction using a Bruker AXS D8 Advance diffractometer equipped with a graphite monochromator and a position-sensitive detector Vântec-1 using Cu K α 1 radiation (45 kV and 40 mA) in Bragg–Brentano geometry. The X-ray scanning was performed in continuous scan mode in the range of 1–45° (2 θ).

The size and shape of zeolite crystals were examined by scanning electron microscopy (SEM) on a JEOL, JSM-5500LV microscope or a MIRA TESCAN microscope. The images were collected with an acceleration voltage of 30 kV. Samples were platinum sputtered before measurement.

The BET area and pore volume of all catalysts were determined by nitrogen physisorption at –196 °C using a 3Flex (Micromeritics) static volumetric apparatus. The degassing of the samples was performed prior to the measurement in a stream of helium at 300 °C for 3 h. The surface area was calculated using BET method in the range of relative pressures $p/p_0 = 0.05$ – 0.20 [37]. The adsorbed amount of nitrogen at $p/p_0 = 0.95$ reflects the total pore volume. The volume of micropores and the external surface area were determined using t -plot method [38].

Chemical composition of the materials (expressed as a Si/Ti ratio) was determined by Thermo Scientific iCAP-7600 inductively coupled plasma optical emission spectrometer (ICP-OES) equipped with peristaltic pump with a drain sensor, free-running 27.12 MHz solid state RF plasma generator, charge injection device detector (CID86) with the range of 166–847 nm and CETAC ASX 520 auto sampler. 50 mg of zeolite was mineralized in a mixture of 1.8 ml of 48% HF, 1.8 ml of 67% HNO₃, and 5.4 ml of 36% HCl in the microwave oven. After cooling, the HF excess was eliminated by the complexation with 13.5 ml of saturated solution of H₃BO₃ and final mixture was treated in microwave oven again. Thereafter, the solution under analysis was collected and

diluted by ultrapure water to a total volume of 250 ml.

Diffuse reflectance ultraviolet-visible (DR-UV/Vis) spectra were collected using Perkin-Elmer Lambda 950 Spectrometer. For that, a 2 mm quartz tube was filled with the sample. The spectra were collected in a wavelength range of 190–500 nm and converted to absorption spectra using the Kubelka-Munk function.

^{29}Si -MAS-NMR spectra were collected on a Bruker Avance III HD 500 MHz spectrometer. Chemical shifts were referred to tetramethylsilane. All samples were measured in calcined state using a sample spinning speed of 18 kHz.

2.3. Characterization of acid centres using FTIR of adsorbed probe molecules

2.3.1. Nature and concentration of acid sites

The concentration of Lewis acid sites (LAS) in titanosilicate zeolites was determined by pyridine-FTIR based on the intensities of characteristic absorption band (a.b.) at 1608 cm^{-1} . The zeolites were pressed into self-supporting wafers with a density of $\sim 10\text{ mg/cm}^2$ and *in situ* activated at $T = 450\text{ }^\circ\text{C}$ and $p = 5 \cdot 10^{-5}\text{ Torr}$ for 4 h.

To determine the temperature of PY adsorption/desorption sufficient for removal of H-bonded probe molecule while maintaining PY coordinatively-bonded to Ti-associated Lewis acid sites, an excess of PY (cca. 2 mmol PY per 1 g of zeolite) was adsorbed at $25\text{ }^\circ\text{C}$, $50\text{ }^\circ\text{C}$, $80\text{ }^\circ\text{C}$, $100\text{ }^\circ\text{C}$, $120\text{ }^\circ\text{C}$, $150\text{ }^\circ\text{C}$ and $200\text{ }^\circ\text{C}$ in 3D TS-1(a) sample. For each temperature 10 min adsorption and 10 min desorption took place. FTIR spectra were recorded using a Nicolet iS50 spectrometer with a transmission MTC/B detector with a resolution of 4 cm^{-1} by collecting 128 scans for a single spectrum at room temperature. The spectra were treated using Omnic 8.2 (Thermo Scientific) program. For the baseline correction, spectrum of activated wafer was subtracted from the spectra collected after pyridine adsorption/desorption. To determine the area of the peaks characteristic for coordinatively bonded (1608 cm^{-1}) and H-bonded (1596 cm^{-1}) pyridine the resultant spectral curve was fitted using Gaussian line shape. IR peak centers were fixed within $\pm 5\text{ cm}^{-1}$, and the full widths at half maxima were constrained to be between 5 cm^{-1} and 20 cm^{-1} .

For quantification of the concentrations of LAS in TS-1(a) samples, PY adsorption was carried out at $50\text{ }^\circ\text{C}$ (found to be optimal for the quantitative study of titanosilicates) and a partial pressure of 3.5 torr for 10 min followed by desorption for 10 min at the same temperature. C(LAS) were evaluated from the integral intensities of a.b. at 1608 cm^{-1} using molar absorption coefficients $\epsilon_{1608}(\text{Ti-LAS}) = 0.71 \pm 0.01\text{ cm}^2\text{ }\mu\text{mol}^{-1}$ determined from the linear relationship between [integrated IR band area (cm^{-1}) \times wafer cross sectional area (cm^2)] and the total moles dosed (μmol) similar to Ref. [39–41].

2.3.2. Strength of acid sites

Thermodesorption of PY was carried out at 50, 100, 150 and $200\text{ }^\circ\text{C}$ for 10 min. Distribution of Ti-associated acid centers with respect to their strength was analyzed based on the relative concentration of acid sites bearing pyridine molecules at elevated temperatures:

$$I_{1608}(T^\circ\text{C}) / I_{1608}(50^\circ\text{C}) \quad (1)$$

where

$I_{1608}(X^\circ\text{C})$ refers to the intensity of a.b. at 1608 cm^{-1} in the FTIR spectra of titanosilicate zeolites after activation followed by pyridine adsorption/desorption at $T = X^\circ\text{C}$ (X is 100, 150 and $200\text{ }^\circ\text{C}$).

2.3.3. Accessibility of acid sites

The ratio between “internal” acid sites and those located on the external surface of zeolite crystals (“external” acid centers) of TS-1 catalysts was evaluated based on the analysis of FTIR spectra of ACN adsorbed in the catalysts either after activation or after pre-adsorption of bulky QUI selectively poisoning “external” acid sites as discussed in

Ref. [42,43]. ACN adsorption was performed according to the Ref. [44], while pre-adsorption of QUI was carried out according to the protocol described in Ref. [45]. The concentrations of Ti-LAS were semi-quantitatively estimated from the integral intensities of a.b. at 2304 cm^{-1} . The fraction of „external” acid sites was evaluated as

$$[I_{2304}(\text{ACN}) - I_{2304}(\text{QUI} + \text{ACN})] / I_{2304}(\text{ACN}) \quad (2)$$

where

$I_{2304}(\text{ACN})$ refers to the intensity of a.b. at 2304 cm^{-1} in the FTIR spectra of titanosilicate zeolites after activation followed by ACN adsorption;

$I_{2304}(\text{QUI} + \text{ACN})$ refers to the intensity of a.b. at 2304 cm^{-1} in the FTIR spectra of titanosilicate zeolites after activation followed by co-adsorption of quinoline and ACN.

2.4. Characterization of acid centres using TPD of ammonia

Ammonia temperature programmed desorption (TPDA) was measured using the AutoChem II 2920 (Micromeritics, USA). Typically, 100 mg of zeolite (with grain size 0.25–0.5 mm) was inserted into quartz tubular reactor and anchored by quartz wool. Prior to TPD experiment, sample was heated in helium flow of 25 ml min^{-1} from room to the $250\text{ }^\circ\text{C}$ with defined heating rate of $10\text{ }^\circ\text{C min}^{-1}$ and held at final temperature for 10 min. Then the sample was cooled down to the $50\text{ }^\circ\text{C}$ in the flow of helium (25 ml min^{-1}). Saturation of sample with ammonia was carried out by flowing the sample bed by gas mixture of helium and ammonia (5 vol% of ammonia in He) with flow rate 10 ml min^{-1} at $50\text{ }^\circ\text{C}$ for 30 min followed by removing of weakly bounded molecules by flushing sample out under flow of helium (25 ml min^{-1}) for 30 min. Finally, TPD experiment was carried out by increasing temperature from 50 to $400\text{ }^\circ\text{C}$, at which sample was held for 5 min. The desorbed ammonia in the outlet gas was detected using thermal conductivity detector (TCD) and mass spectrometer (MS) Pfeiffer OmniStar GSD 300, Balzers, on which the mass $m/e = 4$ (He^+), 15 (NH^+), 16 (NH_2^+), 17 (NH_3^+), and 18 (H_2O^+) was monitored.

3. Results and discussion

3.1. Catalyst characterization

XRD patterns of studied catalysts (Supplementary Information (SI), Fig. S1) confirm that all of the titanosilicates synthesized have the structure intended to be obtained. Three well-defined peaks at 7.9° , 8.8° , and 8.9° 2θ corresponding to (011), (020) and (200) reflections are visible in the pattern of 3D TS-1 zeolite evidencing well-ordered structure with typical MFI architecture. In contrast, absence of the (hkl) reflections with $k \neq 0$ in the XRD patterns of both lamellar 2D TS-1 and pillared TS-1-PI catalysts indicate that the thickness of zeolite crystallites is extremely low in (010) direction (along the crystallographic b -axis). Successful pillaring of the TS-1-PITi and TS-1-PISi is proven by the presence of intensive low angle peak at 1.5° 2θ , which is characteristic of the preservation of the interlayer distance originally present in the as-synthesized 2D TS-1. This diffraction peak is not present in the XRD pattern of calcined 2D TS-1. Both 3D TS-1(a) and 3D TS-1(b) show N_2 adsorption isotherms of I type characteristic of purely microporous materials, while 2D TS-1, TS-1-PITi and TS-1-PISi were characterized by non-reversible isotherms of type II with H3 hysteresis which is typically observed for non-rigid aggregates of plate-like particles giving rise to slit-shaped mesopores. (Fig. S2) [46].

The SEM images of 3D TS-1 (a) (SI, Fig. S3a) and 3D TS-1 (b) (SI, Fig. S3b) show that the samples are composed of crystals with a size of 200 nm and 600 nm, respectively. In contrast, 2D TS-1 (SI, Fig. S3c), TS-1-PITi (SI, Fig. S3d) and TS-1-PISi (SI, Fig. S3e) are composed of aggregated nanosheet crystals.

Titanium content, crystal size and textural properties of the TS-1

Table 1
Chemical composition and textural properties of 3D and 2D TS-1 catalysts.

Zeolite	Si/Ti ^a	Crystal size ^a	BET m ² /g	S _{ext} m ² /g	V _{mic} cm ³ /g	V _{tot} cm ³ /g
3D TS-1(a)	28	200 nm	510	63	0.10	0.28
3D TS-1(b)	39	600 nm	450	60	0.13	0.22
2D TS-1	44	nanosheets	576	318	0.12	0.63
TS-1-PITi	19	nanosheets	591	338	0.10	0.55
TS-1-PISi	55	nanosheets	575	180	0.11	0.39

^a Titanium content was determined by ICP-OES analysis; crystal size was determined by SEM.

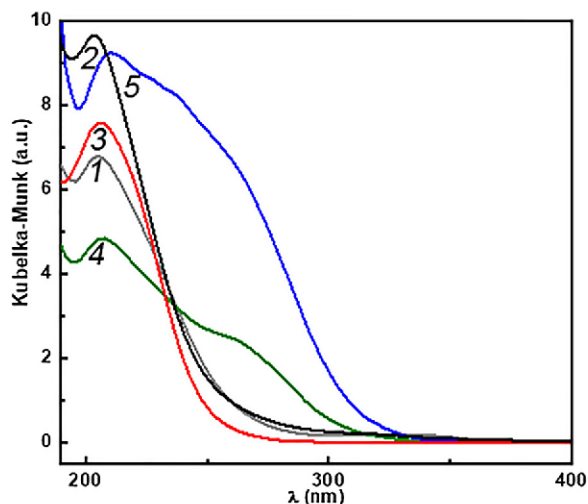


Fig. 1. DR-UV/Vis spectra of 3D TS-1(a) (1), 3D TS-1(b) (2), 2D TS-1 (3), TS-1-PISi (4), and TS-1-PITi (5).

catalysts are summarized in Table 1. Note the differences in Si/Ti ratio between 2D TS-1 (Si/Ti = 44), TS-1-PISi (Si/Ti = 55) and TS-1-PITi (Si/Ti = 19) are caused by dilution of the parent 2D TS-1 with silica pillars in TS-1-PISi and formation of additional titanium sites in TS-1-PITi, respectively [18].

UV/Vis spectra of the studied catalysts are presented in Fig. 1. The spectra of both 3D TS-1 samples and 2D TS-1 contain only one absorption band centered at 205 nm, which is characteristic of framework tetrahedrally coordinated titanium species [24]. The TS-1-PISi contains an additional band at approx. 260 nm, characteristic of isolated 5-coordinated titanium species [24]. The TS-1-PITi contains the same band with higher intensity. Presence of 5-coordinated Ti species may have two reasons. In the TS-1-PITi, majority of the 5-coordinated extra-framework species is formed in the silica-titania pillaring step, when the additional Ti source reacts with the surface of the crystalline layers. In contrast, the origin of 5-coordinated species in TS-1-PISi is not so clear. It is unlikely that Ti atoms were extracted from framework positions during pillaring or calcination; however, the observed band may represent originally surface framework Ti atoms now in contact with the amorphous silica pillars.

Remarkable increase in external surface area for 2D forms of the TS-1 (180–340 m² g⁻¹, Table 1) vs. 3D TS-1 (60 m² g⁻¹, Table 1) was accompanied with increasing number of silanol defects, as detected by ²⁹Si MAS NMR. The Q³ Si species at -102 ppm and Q⁴ Si species at -114 ppm were observed for all titanosilicates under the study (Fig. 2). Selective enhancement of the resonance band at -102 ppm in the ¹H-²⁹Si cross polarization (CP) MAS NMR experiment (Fig. 2) evidenced the assignment of respective signal to silicon atoms that are coupled with the hydrogens of the hydroxyl groups by dipolar interaction, i.e., to (SiO)₃Si–OH moieties.

Thus, according to their basic characteristics, the prepared

titanosilicates are qualified as representative 3D- and 2D TS-1 zeolites, being appropriate for comparative study on the number, strength and accessibility of Ti-associated acid sites.

3.2. Acidity of TS-1 catalysts

3.2.1. Nature, concentration and strength of acid sites

Pyridine, a versatile base molecule for probing zeolite acidity [26], was used for qualitative and quantitative study of acid sites in TS-1 catalysts in this work. The FTIR spectra of the activated TS-1 zeolites displaying the characteristic bands of free silanol groups (3743 cm⁻¹) are shown in Fig. 3 (A). Higher intensity of respective band is typical for all 2D catalysts, which is consistent with the higher external surface area of layered zeolites (Table 1) and thus increased content of terminal silanol groups. The adsorption of an excess of pyridine, followed by evacuating of physically adsorbed probe molecules gave rise to new absorption bands in 1700–1400 cm⁻¹ region (Fig. 3B). While the ν_{8b} (1577 cm⁻¹), ν_{19a} (1490 cm⁻¹) and ν_{19b} (1445 cm⁻¹) a.b. of H-bonded and LAS-Py convolutes, the ν_{8a} a.b. are well-distinguishable at 1596 cm⁻¹ (ν_{8a}-H) and 1608 cm⁻¹ (ν_{8a}-LAS), respectively [26,47]. On the other hand, no ν_{19b} absorption band characteristic of Brønsted acid sites (1545 cm⁻¹) was detected for materials under investigation, which is in line with previous reports [48,49] as well as with character of the materials (containing no T³⁺ atoms).

Relative intensities of respective ν_{8a} bands were found dependent on the temperature of pyridine adsorption/desorption (the spectra of 3D TS-1(a) zeolite are shown as representative in Fig. 4A). Intensity of ν_{8a}-LAS band at 1608 cm⁻¹ is almost constant at T = 25–50 °C. At the same time, 20–25% decrease of either ν_{8a}-H or ν_{19b}-H + LAS band intensity was observed at T = 50 °C vs. T = 25 °C (Fig. 4B). Further increase in adsorption/desorption temperature resulted not only in removal of the most of H-bonded pyridine (54–96% decreasing ν_{8a}-H at T = 70–150 °C), but also substantially reduced the intensity of ν_{8a}-LAS band (25–73% decreasing ν_{8a}-LAS at T = 70–150 °C). Difference spectra obtained by subtraction of the spectrum of activated zeolite from the ones after adsorption/desorption of pyridine show the region of OH vibrations (Fig. 4B). Decrease in intensity of absorption band ca 3743 cm⁻¹ with increasing adsorption/desorption temperature is indicative for reducing contribution of H-bonded pyridine.

Thus, low strength of Ti-associated LAS precludes full removal of H-bonded pyridine while maintaining coordinatively bonded probe molecules and therefore impedes use of routine FT-IR acidity analysis protocol widely applied for aluminosilicate zeolites (i.e., (i) saturation of the sample with pyridine at T = 150–200 °C; (ii) evacuating the sample at the same temperature and (iii) monitoring the intensity of ν_{19b} 1445 cm⁻¹ band [26]). In contrast, using the intensity of ν_{8a}-LAS was found sufficient for quantification of LAS in TS-1 catalysts after adsorption of pyridine at 50 °C. Adsorbing pyridine, the first small doses gave rise only to ν_{8a}-LAS, while ν_{8a}-H started to increase only after adding certain amount of the probe molecules. Thus, special attention was paid to proper choice of the range of pyridine concentrations (e.g., < 1.2 μmol/cm², Fig. 5) enabling to neglect contribution of H-bonded pyridine to the value of molar absorption coefficient ε₁₆₀₈(Ti-LAS). Indeed, careful analysis of the difference FTIR spectra collected in OH vibration region at increasing dosing of adsorbed pyridine revealed negligible contribution of H-bonded probe molecule when the overall adsorbed amount did not exceed 1.2 μmol/cm² (Fig. 5B). Fig. 5 shows the results obtained by adsorbing increasing quantities of pyridine in 3D TS-1 at 50 °C. In our experiments, the intensity of ν_{8a}-LAS at 1608 cm⁻¹ increases linearly with the amount of pyridine introduced. Thus, the extinction coefficient for the 1608 cm⁻¹ band on 3D TS-1 zeolite was found to be equal to 0.71 ± 0.01 cm² μmol⁻¹.

Once having the ε₁₆₀₈(Ti-LAS) value, total concentration of Lewis acid sites was calculated based on the integral intensity of ν_{8a}-LAS (1608 cm⁻¹) after adsorption and consecutive desorption of an excess of pyridine at 50 °C. The total concentrations of Lewis acid sites in the

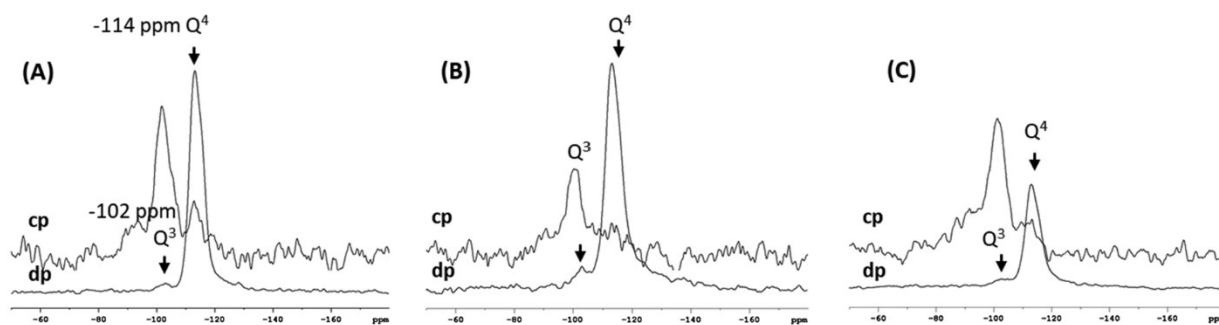


Fig. 2. Direct pulse ^{29}Si MAS NMR (dp) and ^1H - ^{29}Si CP/MAS NMR (cp) spectra of titanosilicates (A) TS-1(b), (B) 2D TS-1 and (C) TS-1-PITi.

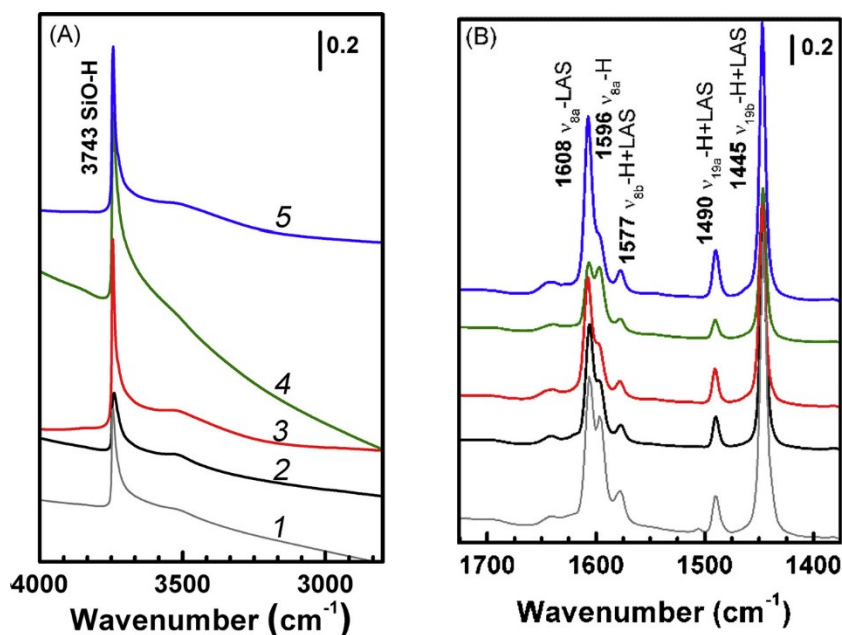


Fig. 3. FTIR spectra of 3D TS-1(a) (1), 3D TS-1(b) (2), 2D TS-1 (3), TS-1-PiSi (4), TS-1-PITi (5) activated zeolites (A); spectra after adsorption/desorption of an excess of pyridine at 50°C (B).

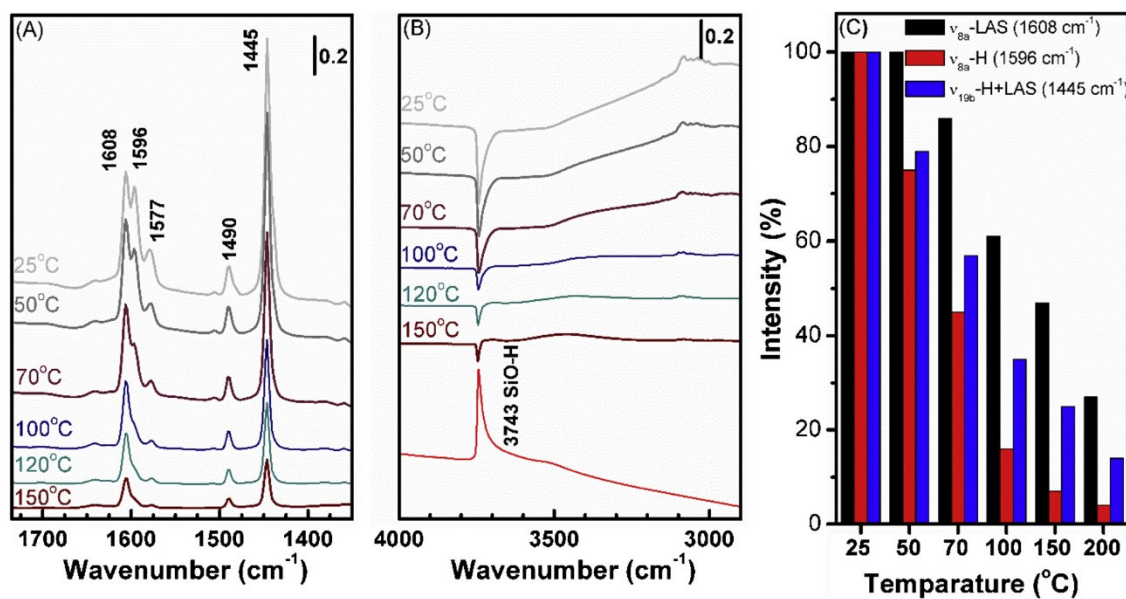


Fig. 4. FTIR spectra of 3D TS-1(a) after adsorption/desorption of pyridine at different temperatures in the region of pyridine vibrations (A). Difference FTIR spectra after adsorption/desorption of pyridine at different temperatures are compared with the spectrum of activated 3D TS-1(a) zeolite (-) in the region of OH vibrations (B). Relative change of the intensities of a.b. at 1596 cm^{-1} ($\nu_{8a}\text{-H}$) and 1608 cm^{-1} ($\nu_{8a}\text{-LAS}$) vs. temperature of pyridine adsorption/desorption in 3D TS-1 zeolite (C).

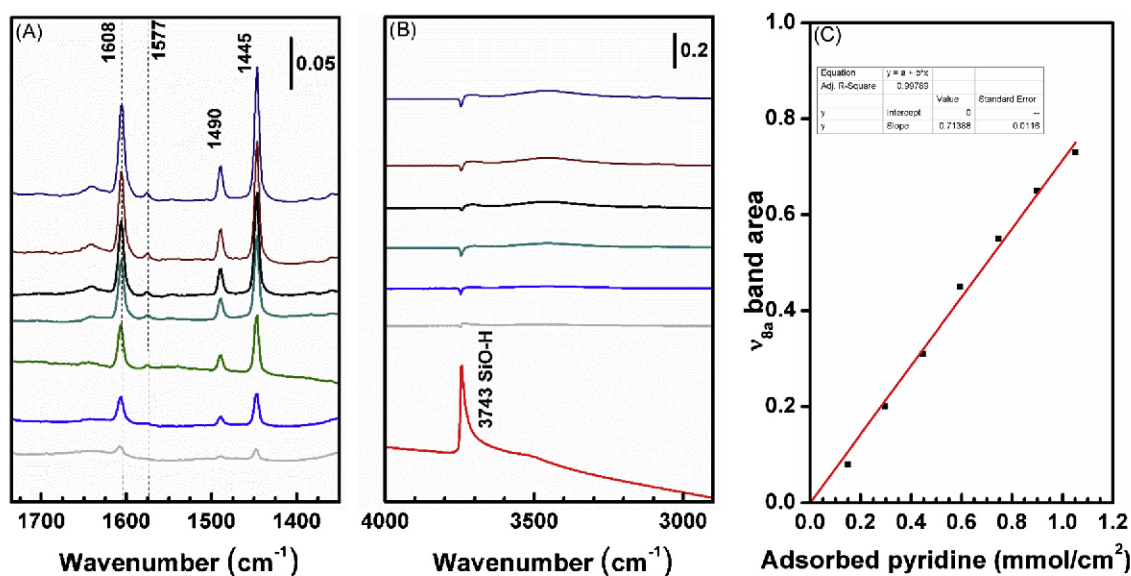


Fig. 5. FTIR spectra of 3D TS-1(a) zeolite in the region of pyridine ring vibrations at increasing dosing of pyridine adsorbed at 50 °C (A). Difference FTIR spectra collected at increasing dosing of adsorbed pyridine are compared with the spectrum of activated 3D TS-1(a) zeolite (–) in the region of OH vibrations (B). Dependence of ν_{8a} -LAS (1608 cm^{-1}) band area on the concentration of adsorbed pyridine for 3D TS-1 (a) (C).

Table 2

Concentration of Lewis acid sites in 3D and 2D TS-1 catalysts determined using FTIR-PY and TPDA.

Sample	Chemical composition		Concentration of acid sites, mmol/g	
	Si/Ti	c(Ti) mmol/g	FTIR-Py	TPDA
3D TS-1(a)	28	0.57	0.55	0.56
3D TS-1(b)	39	0.41	0.40	0.47
2D TS-1	44	0.37	0.39	n.d.
TS-1-PITi	19	0.82	0.61	0.70
TS-1-PISi	55	0.30	0.23	n.d.

TS-1 catalysts (Fig. 3B) were found to decrease in the following order: TS-1-PITi (0.61 mmol/g) > 3D TS-1 (a) (0.55 mmol/g) > 3D TS-1 (b) (0.40 mmol/g) > 2D TS-1 (0.39 mmol/g) > TS-1-PISi (0.23 mmol/g). This is in agreement with the results of TPDA (Fig. S4) used as an independent method for verification the results of FTIR-Py for the chosen TS-1 zeolite samples (Table 2). Indeed, TPDA using smaller ammonia probe molecule showed slightly higher values for the concentration of acid sites, but the difference with FTIR-Py results did not exceed 15%. On the other hand, perfect consistence between the number of acid sites and chemical composition of 3D TS-1 zeolites containing mostly tetrahedral Ti atoms (Table 2) reveals unlimited accessibility of Lewis acid sites for pyridine molecules under experimental conditions used. In contrast to pyridine, recent reports state restricted conformational freedom of alkylated pyridines in the channels of MFI [50–52], which precludes the use of such bulky probe molecules for quantification of Lewis acid sites in zeolites with ≤ 10 -ring channels. Instead, using of smaller molecular probes, e.g. ammonia, d_3 -acetonitrile [26,44] may give more complete results for small-pore zeolites. The difference between chemical composition and measured concentration of acid sites in the pillared samples (TS-1-PITi, TS-1-PISi) is observed most likely because a share of titanium is trapped inside or covered by the pillars and thus inaccessible.

The distribution of Ti-associated LAS with respect to their strength was investigated by a stepwise thermodesorption of adsorbed pyridine while recording the residual intensity of the remaining characteristic ν_{8a} -LAS (1608 cm^{-1}) band. The part of LAS, which retained adsorbed pyridine at $T = 150$ – 200 °C was evidently higher for TS-1-PITi, while

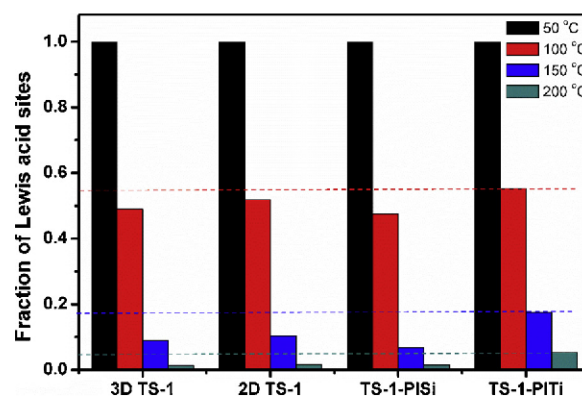


Fig. 6. Fraction of LAS for TS-1 zeolites of different structures and morphologies vs. temperature of pyridine desorption.

all 3D TS-1 (a) and (b), 2D TS-1 and TS-1-PISi showed similar fraction of stronger LAS (Fig. 6). This result is most likely connected with the contribution of $\text{Ti}(\text{OH})(\text{OSi})_3$ groups on the external surface of the titanasilicate layers created during the post-synthesis treatment. This result is in line with previous reports on the higher acid strength of mesostructured Ti-MCM-41 material and amorphous TiO_2 - SiO_2 both bearing tripodal $\text{Ti}(\text{OH})(\text{OSi})_3$ moieties forming more stable Ti-pyridine complexes than the $\text{Ti}(\text{OSi})_4$ sites in TS-1 [22,24].

On the other hand, several FTIR studies reported on the strength of Brønsted acid sites [53,54] and Lewis acid extra-framework Li^+ cations [55,56] in 3D and 2D aluminosilicate zeolites. No significant differences in acidity strength between the 3D and 2D form of the same zeolite was found [54,56] (e.g. MCM-22 vs. MCM-36 (pillared MWW layers) – a pair analogous to TS-1 and TS-1-PISi).

3.2.2. Accessibility of acid sites

To determine the amount of acid sites located on the external surface of TS-1 zeolite crystals, i.e., acid sites accessible for bulky substrates, we first adsorbed quinoline to poison the external acid sites and subsequently we introduced d_3 -acetonitrile (ACN) to determine the internal acid centres. The strength of ACN bonding to acid sites is reflected in the shift of the stretching mode of $\nu(\text{C}\equiv\text{N})$ to higher frequencies if to compare with 2265 cm^{-1} characteristic of ACN in liquid

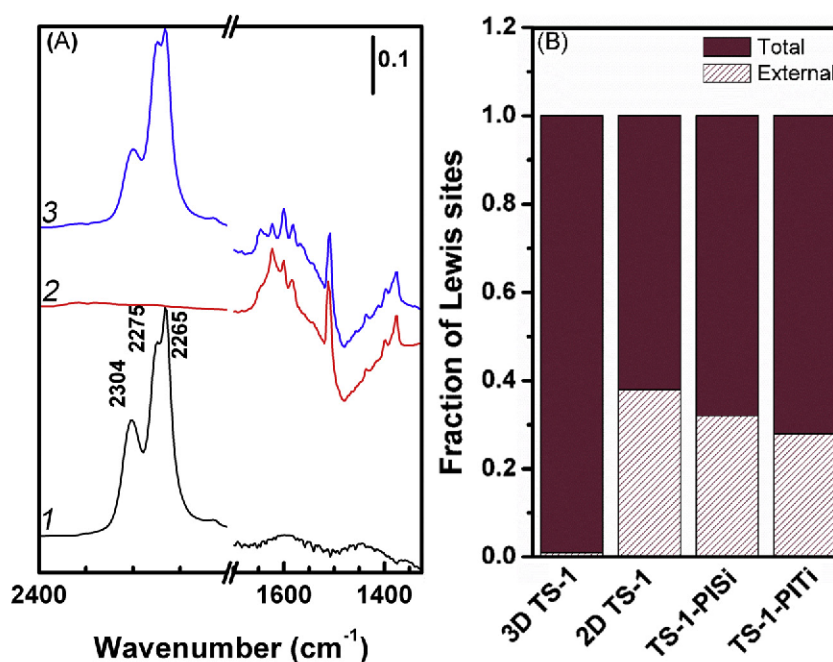


Fig. 7. FTIR spectra of 2D TS-1 after adsorption of AN (1), quinoline (2), and co-adsorption of quinoline and d₃-acetonitrile (3) (A). Fraction of external LAS in TS-1 catalysts determined using FTIR of co-adsorbed quinoline and d₃-acetonitrile (B).

phase [57]. In particular, the spectra of ACN adsorbed in TS-1 zeolites (spectra of 2D TS-1 shown as an example in Fig. 7A) contain a single band at 2304 cm⁻¹ attributed to CN vibration of the probe molecule interacting with weak Ti-associated Lewis sites as well as 2 other peaks corresponding to ACN adsorbed on silanol groups (2275 cm⁻¹), and physisorbed ACN (2265 cm⁻¹). IR spectra of ACN adsorbed on activated 2D TS-1 and those collected after QUI pre-adsorption are compared in Fig. 7A. It can be seen that quinoline pre-adsorption obviously decreased the intensity of the peak I₂₃₀₄ attributed to the interaction between ACN and Ti-Lewis acid sites. Thus, the comparison between the I₂₃₀₄ (ACN) and I₂₃₀₄ (QUI + ACN) allow to determine the fraction of Ti-associated LAS located on the external surface of TS-1 crystals. Noticeably, all layered 2D TS-1, TS-1-PISi and TS-1-PITi zeolites showed similar fraction of external acid centers (28–38%, Fig. 7B), while the fraction for 3D TS-1 was negligible (2%, Fig. 7B). These results are in agreement with previously reported higher catalytic activity of layered forms of TS-1 zeolites vs. 3D TS-1 in reactions involving bulky molecules [18,19].

4. Conclusions

Methodology for quantification of Lewis acid sites in titanasilicate zeolites using FT-IR analysis of adsorbed pyridine species was developed and applied to characterize TS-1 catalysts of different structures and morphologies (3D TS-1, lamellar 2D TS-1, 2D TS-1 pillared either with silica TS-1-PISi or silica-titania TS-1-PITi). The Ti-associated Lewis acid centres are, in contrast to aluminosilicate zeolites, of a low strength and this was found precluding the use of routine protocol to quantify LAS (i.e., monitoring the intensity of ν_{19b} 1445 cm⁻¹ band [26]). Instead, the total concentration of Lewis acid sites in TS-1 catalysts was shown to be accurately determined after adsorption/desorption of an excess of pyridine at 50 °C from the integral intensity of ν_{8a}-LAS (1608 cm⁻¹) absorption band. Molar extinction coefficient for the respective band was determined ε₁₆₀₈(Ti-LAS) = 0.71 ± 0.01 cm μmol⁻¹. Note this band can be used for quantification thank to absence of Brønsted acid sites in the titanasilicate zeolites.

Thermodesorption of pyridine monitored with FT-IR evidenced similar strength distribution of Lewis acid sites in all samples containing titanium introduced by direct hydrothermal synthesis (i.e. 3D TS-1, 2D

TS-1 and TS-1-PISi). In contrast, the TS-1-PITi, containing share of titanium introduced by post-synthesis treatment (and previously shown to be the most active catalyst in cycloalkene-to-epoxide transformation [18,19]), possessed increased concentration of strong Lewis acid centres.

FTIR spectroscopy of samples with pre-adsorbed quinoline and d₃-acetonitrile probe molecule confirmed the enhanced relative concentration of external Lewis acid sites in the layered TS-1 materials (28–38%) vs. 3D TS-1 (2%). The results presented in this paper provide fundamental knowledge on the features of acid sites in the recently designed layered and pillared TS-1 zeolites, which will contribute to the development of heterogeneous selective oxidation catalysts.

Acknowledgements

M.S. thanks the Primus Research Program of the Charles University (project number PRIMUS/17/SCI/22 “Soluble zeolites”); J.P., M.S. acknowledge OP VVV “Excellent Research Teams” project no. CZ.02.1.01/0.0/0.0/15_003/0000417 – CUCAM; J.Z. acknowledges the support of the Czech Science Foundation through the project EXPRO (19-27551X). The authors thank also to Prof. Roman Bulánek, University of Pardubice for collecting the TPDA curves.

Appendix A. Supplementary data

Supplementary material related to this article can be found, in the online version, at doi:<https://doi.org/10.1016/j.cattod.2019.10.011>.

References

- [1] M. Taramasso, G. Perego, B. Notari, Preparation of porous crystalline synthetic material comprised of silicon and titanium oxides US 4410501.
- [2] R. Millini, E. Previde Massara, G. Perego, G. Bellussi, J. Catal. 137 (1992) 497–503.
- [3] X. Lu, W.-J. Zhou, H. Wu, A. Liebens, P. Wu, Appl. Catal. A Gen. 515 (2016) 51–59.
- [4] C. Perego, A. Carati, P. Ingallina, M.A. Mantegazza, G. Bellussi, Appl. Catal. A Gen. 221 (2001) 63–72.
- [5] A. Korzeniowska, J. Grzybek, W.J. Roth, A. Kowalczyk, P. Michorczyk, J. Cejka, J. Prech, B. Gil, ChemCatChem 11 (2019) 520–527.
- [6] M. Mazur, V. Kasnerik, J. Prech, F. Brivio, C. Ochoa-Hernandez, A. Mayoral, M. Kubu, J. Cejka, Inorg. Chem. Front. 5 (2018) 2746–2755.
- [7] M.A. Cambor, A. Corma, A. Martinez, J. Perez-Pariente, J. Chem. Soc. Chem.

- Commun. (1992) 589–590.
- [8] P. Wu, T. Tatsumi, T. Komatsu, T. Yashima, *J. Phys. Chem. B* 105 (2001) 2897–2905.
- [9] P. Wu, T. Komatsu, T. Yashima, *J. Phys. Chem.* 100 (1996) 10316–10322.
- [10] Y. Kubota, Y. Koyama, T. Yamada, S. Inagaki, T. Tatsumi, *Chem. Commun. (Cambridge, U. K.)* (2008) 6224–6226.
- [11] J. Pfech, D. Vitvarová, L. Lupínková, M. Kubů, J. Čejka, *Microporous Mesoporous Mater.* 212 (2015) 28–34.
- [12] S.-Y. Kim, H.-J. Ban, W.-S. Ahn, *Catal. Lett.* 113 (2007) 160–164.
- [13] J. Pfech, J. Čejka, *Catal. Today* 277 (2016) 2–8.
- [14] J. Prech, P. Pizarro, D.P. Serrano, J. Čejka, *Chem. Soc. Rev.* 47 (2018) 8263–8306.
- [15] A. Corma, U. Diaz, M.E. Domine, V. Fornes, *Chem. Commun. (Cambridge, U. K.)* (2000) 137–138.
- [16] K. Na, C. Jo, J. Kim, W.S. Ahn, R. Ryoo, *ACS Catal.* 1 (2011) 901–907.
- [17] W.J. Roth, P. Nachtigall, R.E. Morris, J. Čejka, *Chem. Rev.* 114 (2014) 4807–4837.
- [18] J. Pfech, P. Eliášová, D. Aldhayan, M. Kubů, *Catal. Today* 243 (2015) 134–140.
- [19] J. Pfech, *Catal. Rev.* 60 (2018) 71–131.
- [20] J. Pfech, M. Kubů, J. Čejka, *Catal. Today* 227 (2014) 80–86.
- [21] D. Trong On, S.V. Nguyen, V. Hulea, E. Dumitriu, S. Kaliaguine, *Microporous Mesoporous Mater.* 57 (2003) 169–180.
- [22] D. Srinivas, R. Srivastava, P. Ratnasamy, *Catal. Today* 96 (2004) 127–133.
- [23] L. Wu, S. Zhao, L. Lin, X. Fang, Y. Liu, M. He, *J. Catal.* 337 (2016) 248–259.
- [24] P. Ratnasamy, D. Srinivas, H. Knözinger, *J. Adv. Catal. Sci. Technol.* 48 (2004) 1–169.
- [25] Z. Zhuo, L. Wang, X. Zhang, L. Wu, Y. Liu, M. He, *J. Catal.* 329 (2015) 107–118.
- [26] S. Bordiga, C. Lamberti, F. Bonino, A. Travert, F. Thibault-Starzyk, *Chem. Soc. Rev.* 44 (2015) 7262–7341.
- [27] B. Gil, Acidity of zeolites, in: J. Čejka, J. Pérez-Pariante, W.J. Roth (Eds.), *Zeolites: From Model Materials to Industrial Catalysts Transworld Research Network*, 2008, pp. 173–207.
- [28] W.J. Roth, J. Čejka, R. Millini, E. Montanari, B. Gil, M. Kubu, *Chem. Mater.* 27 (2015) 4620–4629.
- [29] B. Gil, W.J. Roth, W. Makowski, B. Marszałek, D. Majda, Z. Olejniczak, P. Michorczyk, *Catal. Today* 243 (2015) 39–45.
- [30] B. Gil, G. Kosova, J. Čejka, *Microporous Mesoporous Mater.* 129 (2010) 256–266.
- [31] D.P. Serrano, R.A. García, M. Linares, B. Gil, *Catal. Today* 179 (2012) 91–101.
- [32] M. Bevilacqua, G. Busca, *Catal. Commun.* 3 (2002) 497–502.
- [33] B. Gil, K. Kalahurska, A. Kowalczyk, *Appl. Catal. A Gen.* 578 (2019) 63–69.
- [34] B. Gil, W. Makowski, B. Marszałek, W.J. Roth, M. Kubu, J. Čejka, *Z. Olejniczak, Dalton Trans.* 43 (2014) 10501–10511.
- [35] B. Gil, B. Marszałek, A. Micek-Ilnicka, Z. Olejniczak, *Top. Catal.* 53 (2010) 1340–1348.
- [36] M. Taramasso, G. Perego, B. Notari, H. Robson (Ed.), *Verified Syntheses of Zeolitic Materials*, Elsevier, Amsterdam, 2001, p. 207.
- [37] S. Brunauer, P.H. Emmett, E. Teller, *J. Am. Chem. Soc.* 60 (1938) 309–319.
- [38] B.C. Lippens, J.H. de Boer, *J. Catal.* 4 (1965) 319–323.
- [39] B. Gil, K. Kalahurska, A. Kowalczyk, *Appl. Catal. A Gen.* 578 (2019) 63–69.
- [40] J.W. Harris, M.J. Cordon, J.R. Di Iorio, J.C. Vega-Vila, F.H. Ribeiro, R. Gounder, *J. Catal.* 335 (2016) 141–154.
- [41] F. Thibault-Starzyk, B. Gil, S. Aiello, T. Chevreau, J.-P. Gilson, *Microporous Mesoporous Mater.* 67 (2004) 107–112.
- [42] A. Corma, V. Fornés, F. Rey, *Zeolites* 13 (1993) 56–59.
- [43] Y. Zhou, S.A. Kadam, M. Shamzhy, J. Čejka, M. Opanasenko, *ACS Catal.* 9 (2019) 5136–5146.
- [44] Q. Yue, J. Zhang, M. Shamzhy, M. Opanasenko, *Microporous Mesoporous Mater.* 280 (2019) 331–336.
- [45] M. Pitínová-Štekrová, P. Eliášová, T. Weissenberger, M. Shamzhy, Z. Musilová, J. Čejka, *Catal. Sci. Tech.* 8 (2018) 4690–4701.
- [46] M. Thommes, K.A. Cychosz, *Adsorption* 20 (2014) 233–250.
- [47] A. Travert, A. Vimont, A. Sahibed-Dine, M. Daturi, J.-C. Lavalley, *Appl. Catal. A Gen.* 307 (2006) 98–107.
- [48] A. Zecchina, G. Spoto, S. Bordiga, M. Padovan, G. Leofanti, G. Petrini, IR spectra of CO adsorbed at Low temperature (77 K) on titaniumsilicalite, H-ZSM5 and silicalite, in: G. Öhlmann, H. Pfeifer, R. Fricke (Eds.), *Stud. Surf. Sci. Catal. Elsevier*, 1991, pp. 671–680.
- [49] F. Bonino, A. Damin, S. Bordiga, C. Lamberti, A. Zecchina, *Langmuir* 19 (2003) 2155–2161.
- [50] T. Armaroli, M. Bevilacqua, M. Trombetta, Ad.G. Alejandre, J. Ramirez, G. Busca, *Appl. Catal. A Gen.* 220 (2001) 181–190.
- [51] T.K. Phung, G. Busca, *Appl. Catal. A Gen.* 504 (2015) 151–157.
- [52] T. Armaroli, M. Trombetta, A.G. Alejandre, J.R. Solís, G. Busca, *Phys. Chem. Chem. Phys.* 2 (2000) 3341–3348.
- [53] C.O. Areal, M.R. Delgado, P. Nachtigall, H.V. Thang, M. Rubes, R. Bulánek, P. Chlubna-Eliasova, *Phys. Chem. Chem. Phys.* 16 (2014) 10129–10141.
- [54] H.V. Thang, J. Vaculik, J. Prech, M. Kubu, J. Čejka, P. Nachtigall, R. Bulánek, L. Grajciar, *Microporous Mesoporous Mater.* 282 (2019) 121–132.
- [55] H.V. Thang, K. Frollich, M. Shamzhy, P. Eliášová, M. Rubeš, J. Čejka, R. Bulánek, P. Nachtigall, *Phys. Chem. Chem. Phys.* 18 (2016) 18063–18073.
- [56] R. Bulánek, M. Kolarova, P. Chlubna, J. Čejka, *Adsorption* 19 (2013) 455–463.
- [57] B. Wichterlová, Z. Tvarůžková, Z. Sobalík, P. Sarv, *Microporous Mesoporous Mater.* 24 (1998) 223–233.

3. **J. Zhang**, O. Veselý, M. Shamzhy, M. Opanasenko, J. Čejka. [High Activity of Ga-Containing Nanosponge MTW Zeolites in Acylation of P-xylene](#). *Catalysis Today*, 2020, 345, 110-115.
4. **J. Zhang**, M. Liu, R. Zhang, B. Wang, Z. Huang. [Insight into the Properties of Stoichiometric, Reduced and Sulfurized CuO Surfaces: Structure Sensitivity for H₂S Adsorption and Dissociation](#). *Molecular Catalysis*, 2017, 438, 130-142.
5. **J. Zhang**, R. Zhang, B. Wang, L. Ling. [Insight into the Adsorption and Dissociation of Water over Different CuO \(111\) Surfaces: The Effect of Surface Structures](#). *Applied Surface Science*, 2016, 364, 758-768.
6. I. Podolean, **J. Zhang**, M. Shamzhy, V. I. Pârvulescu, J. Čejka. [Solvent-Free Ketalization of Polyols over Germanosilicate Zeolites: The Role of the Nature and Strength of Acid Sites](#). *Catalysis Science & Technology*, 2020, 10, 8254-8264.
7. Q. Yue, **J. Zhang**, M. Shamzhy, M. Opanasenko. [Seeded Growth of Isomorphously Substituted Chabazites in Proton-Form](#). *Microporous and Mesoporous Materials*, 2019, 280, 331-336.
8. R. Zhang, **J. Zhang**, B. Jiang, B. Wang, M. Fan. [The Cost-Effective Cu-Based Catalysts for the Efficient Removal of Acetylene from Ethylene: The Effects of Cu Valence State, Surface Structure and Surface Alloying on the Selectivity and Activity](#). *Chemical Engineering Journal*, 2018, 351, 732-746.
9. L. Kang, **J. Zhang**, R. Zhang, L. Ling, B. Wang. [Insight into the Formation Mechanism and Kinetics for the Oxidative Carbonylation of Methanol to Dimethyl Carbonate over CuO Catalyst: Effects of Cu Valence State and Solvent Environment](#). *Molecular Catalysis*, 2018, 449, 38-48.
10. R. Zhang, **J. Zhang**, B. Zhao, L. He, A. Wang, B. Wang. [Insight into the Effects of Cu Component and the Promoter on the Selectivity and Activity for Efficient Removal of Acetylene from Ethylene on Cu-Based Catalyst](#). *The Journal of Physical Chemistry C*, 2017, 121, 27936-27949.
11. M. Shamzhy, J. Přeč, **J. Zhang**, V. Ruaux, H. El-Siblani, S. Mintova. [Quantification of Lewis Acid Sites in 3D and 2D TS-1 Zeolites: FTIR Spectroscopic Study](#). *Catalysis Today*, 2020, 345, 80-87.

Conference

1. **Oral presentation**, Seminar of Students 2018 in J. Heyrovsky Institute, "Overcoming application limitations of germanosilicate zeolites: post-synthesis

- tailoring the active sites”, June 12-13, 2018, Prague, Czech Republic.
2. **Oral presentation**, Workshop-Advances in Low-dimensional Materials, “Tailoring the active sites by post-synthesis of germanosilicate zeolites” , Sep. 18-21, 2018, Liblice, Czech Republic.
 3. **Poster**, 50th Symposium on Catalysis, “On the formation of Al-substituted stage-structured UTL-derived zeolites”, Nov. 5-6, 2018, Prague, Czech Republic.
 4. **Poster**, 8th Czech-Italian-Spanish Conference on Molecular Sieves and Catalysis, “Improving application potential of germanosilicate zeolites: post-synthesis tailoring the active sites coupled with germanium recycling”, June 11-14, 2019, Amantea, Italy.

Honors & Awards

- 2018 Outstanding Thesis Award
- 2016 National Scholarship
- 2016 Presidential Scholarship
- 2015 The First Prize Scholarship
- 2013 National Endeavor Fellowship
- 2012 Government Scholarship
- 2011 National Scholarship